Aristotle University of Thessaloniki
Hellenic Open University

Multilepton final states at the Standard Model, as background processes in the search for New Physics, with the ATLAS experiment, with the first LHC data

Dimitrios Iliadis

A thesis submitted for the degree of
Doctor of Philoshophy, Ph.D.

Thessaloniki, Greece
December 2014

This research has been co-financed by the European Union (European Social Fund - ESF) and Greek national funds through the Operational Program "Education and Lifelong Learning" of the National Strategic Reference Framework (NSRF) - Research Funding Program: Heracleitus II. Investing in knowledge society through the European Social Fund.

Η παρούσα έρευνα έχει συγχρηματοδοτηθεί από την Ευρωπαική Ένωση (Ευρωπαικό Κοινωνικό Ταμείο - ΕΚΤ) και από εθνικούς πόρους μέσω του Επιχειρησιακού Προγράμματος "Εκπαίδευση και Δια Βίου Μάθηση" του Εθνικού Στρατηγικού Πλαισίου Αναφοράς (ΕΣΠΑ) - Ερευνητικό Χρηματοδοτούμενο Έργο: Ηράκλειτος ΙΙ. Επένδυση στην κοινωνία της γνώσης μέσω του Ευρωπα'ικού Κοινωνικού Ταμείου.

PhD. committee:

S. Tzamarias (supervisor), Professor, Department of Physics, HOU

Chariclia Petridou (supervisor), Professor, Department of Physics, AUTh

C. Sfetsos, Professor, Department of Physics, UoA

S. Hassani, Researcher A', IRFU, CEA Saclay

A. Leisos, Lecturer, Department of Physics, HOU

D. Sampsonidis, Assistant Professor, Department of Physics, AUTh

K. Kordas, Assistant Professor, Department of Physics, AUTh

Signature from head of Ph.D. committee:

To my family

Abstract

This doctoral thesis presents two studies performed within the context of the ATLAS experiment.

The first one describes the detector-related work of the author of this Thesis. Initially I was involved in the Data Quality Monitoring Framework (DQMF) and specifically in the off-line DQMF monitoring for the Muon Spectrometer (MS) of the ATLAS detector. In the context of this work, I implemented several algorithms that run during data reconstruction at Tier-0, in order to assure their quality and flag them for the off-line shifter. Also, I was involved in a detector performance study in which fully simulated Monte Carlo events were used to investigate the feasibility of the usage of a single lepton trigger, in order to select di-muon events coming from J/ψ and Υ decays. These events are used in order to measure the reconstruction efficiency of Combined and MuTag muons using the Tag and Probe method. The J/ψ and Υ candles are used in order to probe the low-p_{T} region and act complementary to the standard candle, i.e the Z-boson decays. It is shown that the J/ψ candle can be used in order to extract the relevant efficiency, while the Υ candle is not suitable for this task. The results using this method are presented, both from the study with MC as well as from efficiency measured in data.

In the second study, the full 2012 8 TeV data set was used in order to measure the fiducial and total cross-section and to provide the differential distribution with respect to the Z-boson p_{T} in an analysis on the production of the $W^{\pm}Z$ bosons. Fully leptonic decays of the W and Z bosons are considered and even though they represent a small fraction of all the decay modes, they provide a clean experimental signature with background that can be well controlled. Using the full 2012 integrated luminosity that corresponds to 20.28 fb^{-1}, the total cross-section is found to be $\sigma_{WZ}^{tot} = 23.89^{+0.64}_{-0.63}(stat.)^{+0.43}_{-0.36}(syst.)^{+0.75}_{-0.72}(lumi.)\pm 0.33(\mathrm{th.})$ [pb], to be compared with the theoretical prediction of 22.7 $\pm$ 2.7 [pb]. For the derivation of the differential cross-section, the Bayesian Iterative unfolding method was used in order to remove the detector effects; the notions and the details of the method are discussed as well.

Contents

List of Figures

List of Tables

Chapter 1

Theoretical background and motivation

In this chapter a short description of the Standard Model (SM), the collection of theories that describe the fundamental particles and their interactions, is given. A more detailed description of the SM can be found in [1–5].

1.1 A brief look at the Standard Model

The Standard Model (SM) describes the building blocks of matter and their interactions. It was developed from the 1930s up to 1973 and it became very successful in either predicting the existence of new particles or in the expectations of several values of interest (couplings, cross-sections, e.t.c.). Numerous examples verified the validity of the SM in the years that followed, spanning from the discovery of the neutral currents (1973), the gluon (1979), the W and Z bosons (1983), as well as the discovery of the third family of fermions in the years 1975 - 2000 and up to the recent discovery of the Higgs boson in LHC (2013). Apart from the discoveries of particles, several quantitative tests have been performed on the ElectroWeak theory in the past decades at LEP, SLC, Tevatron and currently at the LHC.

1.1.1 Fermions

Fermions are particles that obey the Fermi-Dirac statistics; they are half-integer spin particles that can be further divided into *leptons*[1] and *quarks*[2], where the leptons do not participate in the strong interactions, while quarks carry fractional charge. All fermions can be classified into three families (or generations) with all their characteristics identical except for their mass, which is increasing with the family number. Figure 1.1 summarises the particles along with some of their properties.

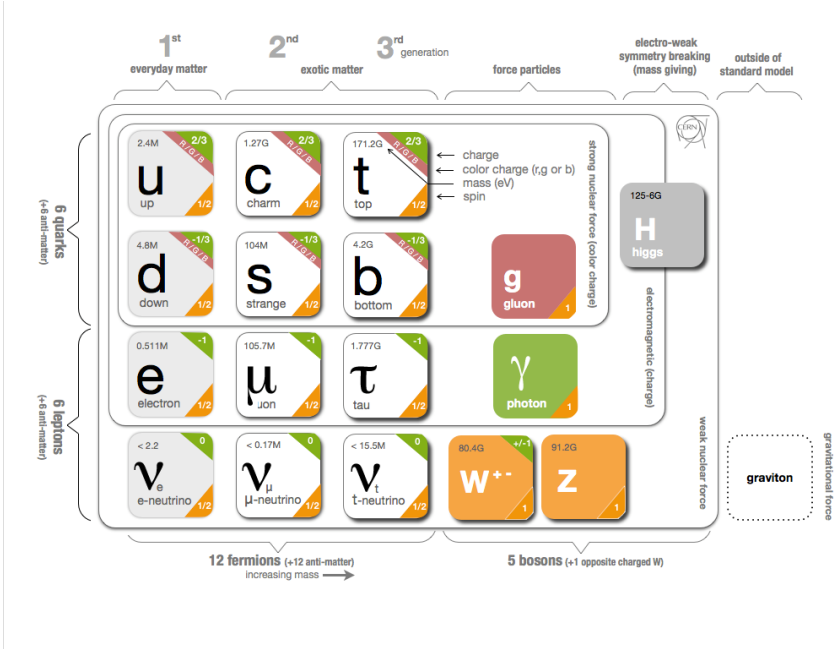

Figure 1.1: The Standard Model (SM) of Particle Physics. All of the SM particles have been experimentally observed, including the Higgs boson.

The Quantum Field Theory (QFT) interpretation of the fields as operators (and not as states) surmounted the difficulties behind Dirac's idea of states with negative energy, allowing us to accept without further objection that, due to relativity, for each particle in nature there exists an anti-particle. For each fermion, i.e. the electron, exists a particle with the exact same properties but the charge; the positron in this case. Some particles may be their own anti-particles, i.e the photon. Table 1.1 lists the masses and charges of

[1]From the Greek work λεπτός which means thin, small.

[2]From the book *Finnegans Wake* by James Joyce: "Three quarks for Muster Mark".

the particles in each of the three generations.

Generation	Lepton	mass (GeV)	Q	Quark	mass (GeV)	Q
1st	e^-	$5{\cdot}10^{-4}$	-1	u	$5{\cdot}10^{-3}$	+2/3
	ν_e	$5< 10^{-9}$	0	d	$3{\cdot}10^{-3}$	-1/3
2nd	μ^-	0.106	-1	c	1.3	+2/3
	ν_μ	$5< 10^{-9}$	0	s	0.1	-1/3
3rd	τ^-	1.78	-1	t	174	+2/3
	ν_τ	$5< 10^{-9}$	0	b	4.5	-1/3

Table 1.1: The constituents of matter along with their fundamental properties. Ordinary matter consists only of particles from the 1^{st} generation. Lepton masses are bare masses. Quark masses are not known exactly but in very wide limits.

1.1.2 Bosons

The second class of particles within the SM includes the mediators of the interactions, namely the bosons. These are particles of integer spin, obeying the Bose-Einstein statistics. Table 1.2 lists the known interactions and their corresponding mediators along with some of their intrinsic properties.

Interaction	Coupling	Boson	mass (GeV)	Q	Spin
Strong	$a_s \sim 1$	gluon(s) g	0	0	1
E/M	$a \sim 10^{-2}$	photon γ	0	0	1
Weak	$a_w \sim 10^{-7}$	W^+ boson	80.4	+1	1
		W^- boson	80.4	-1	1
		Z boson	91.2	0	1
Gravitational	$a_g \sim 10^{-39}$	graviton G	0	0	2

Table 1.2: The interactions mediators and their fundamental properties. The graviton is the assumed mediator of the gravitational interaction and has not yet been observed. The relative coupling strengths are evaluated assuming a distance of 1 fm.

1.2 The Standard Model formalism

In the SM context, the fermions (matter fields) are defined using the chirality operator $f_{L,R} = \frac{1}{2}(1 \pm \gamma^5)f$, where γ^5 is given by the Dirac γ-matrices: $\gamma^\mu = \gamma^0\gamma^1\gamma^2\gamma^3$. The negative sign corresponds to left-handed components of the Dirac field, which are SU(2) weak iso-doublets, while the positive to right-handed components that are singlets:

$$L_1 = \begin{pmatrix} \nu_e \\ e^- \end{pmatrix}_L, e_R, \nu_R, Q_1 = \begin{pmatrix} u \\ d \end{pmatrix}_L, u_R, d_R \tag{1.1}$$

In Equation 1.1 only the first generation fermions have been listed in a model with neutrinos that have small (but non-zero) mass.

The gauge bosons associated with the fundamental interactions are the spin-1 particles:

$$G^A_\mu, A = 1, ..., 8 \tag{1.2}$$

$$W^I_\mu, I = 1, 2, 3, B_\mu \tag{1.3}$$

where in Equations 1.2 and 1.3 the gluons of the strong interaction and the bosons of the EW interaction are listed. Interactions between the fermions and the gauge fields emerge from the invariance of the Lagrangian under gauge tranformations. The group acts on the fermions via the covariant derivative D_μ, expressed in Equation 1.4:

$$D_\mu \psi_L = (\theta_\mu I + g A_\mu)\psi_L \tag{1.4}$$

where I is the identity matrix and A_μ a matrix built from the gauge bosons and the generators of the gauge group. The field strength tensor is defined using the covariant derivative:

$$F_{\mu\nu} = -\frac{i}{g}[D_\mu, D_\nu] \tag{1.5}$$

The only spin-0 field in the theory is the Higgs field, Φ, that couples left- and right-handed fermions together. The Lagrangian can be then expressed in terms of these fields:

$$\begin{aligned} \mathscr{L} = -\frac{1}{2} tr[F_{\mu\nu}F^{\mu\nu}] + \hat{\Psi}_L i\gamma^\mu D_\mu \Psi_L + tr[(D_\mu \Phi)^\dagger D_\mu \Phi] + \\ \mu^2 \Phi^\dagger \Phi - \frac{1}{2}\lambda(\Phi^\dagger \Phi)^2 + (\frac{1}{2}\Psi_L^T C h \Phi \Psi_L + hc) \end{aligned} \tag{1.6}$$

with C being the charge conjugation matrix and h the matrix of Yukawa couplings. All masses are generated from the Higgs mechanism which gives a vacuum expectation to the Higgs field of:

$$\left\langle \Phi \right\rangle = 174 \text{ GeV} \tag{1.7}$$

The SM is a renormalisable, quantum gauge field theory that describes the particles that matter consists of and their interactions, namely the electromagnetic, weak and strong[3],

[3]Gravitational interactions are way too weak compared to the others and can be neglected.

via a combination of the local gauge symmetry groups $SU(3)_C \times SU(2)_L \times U(1)_Y$, where the indices denote the conserved property: color (C), isospin (I)[4] and hypercharge (Y). It is a theory of fields with spins 0, 1/2 and 1; *fermions* being the matter spin-1/2 fields and *bosons* being the mediator spin-1 fields, while the Higgs field is the only spin-0 field in the theory. The SM comprises of Quantum Chromodynamics (QCD) which is the theory of the strong interactions, based on the $SU(3)_C$ gauge symmetry and the Electroweak theory that incorporates the electromagnetic and weak interactions, based on the $SU(2)_L \times U(1)_Y$ gauge symmetry.

1.3 pp experiments Physics

The LHC is the largest hadron accelerator which collides protons[5]. In such a pp collision, a constituent from each proton interacts with a constituent of the other proton. These constituents may be quarks (valence or sea) or gluons; collectively, they are known as *partons*. As the proton energy rises, the part of the momentum that can be carried by gluons and sea quarks rises as well. In the QCD context, there is field manifesting itself as quarks or gluons according to the momentum transfer of the interaction, Q^2. Since pertubative QCD cannot describe the proton structure accurately, proton structure functions, known as Probability Density Functions (PDF), are used. PDFs are functions of the momentum transfer Q^2 and its fraction a parton of flavour i carries, $f_i = f_i(x_i, Q^2)$. PDFs are derived by fitting the experimental data. Summing this picture up, in a pp collision, the actual interaction is between two partons and it is known as the *hard scattering*, leading to 2 (or more) hard outgoing particles. The term "hard" indicates the large fraction x_i of the momentum transfer Q^2 that a parton of flavour i carries.

A very important property of QCD is the *factorisation* theorem that "factors-out" the hard, short-distance component that can be calculated using pertubative QCD from the soft, long-distance one that needs to be evaluated via PDFs. Therefore, the hard scattering cross-section calculation for a pp collision can be then expressed as:

$$\sigma = \sum_{i,j} \int dx_1 dx_2 f_i(x_1, \mu_F) f_j(x_2, \mu_F) \times \hat{\sigma_{i,j}}(p_1, p_2, a_s(\mu_R^2), Q^2/\mu_R, Q^2/\mu_F) \tag{1.8}$$

[4]Even though the index in this case was L, denoting that only left-handed fields are present.

[5]The LHC also has a complementary Physics program that uses lead-ions.

where the subscripts i, j denote the parton flavour, x is the fraction of the proton momentum that each parton carries and $f_i(x_1, \mu_F), f_j(x_2, \mu_F)$ the PDFs of the interacting partons which incorporate the fragmentation effects. The cross-section of the hard, short-distance component, $\hat{\sigma}_{i,j}$ can be calculated as a series of the strong coupling constant, a_s[6]

$$\hat{\sigma} = (a_s)^2 \sum_{\nu=0}^{n} C_\nu \cdot (a_s)^\nu \tag{1.9}$$

where the C_ν coefficients are functions of the renormalisation and factorisation scales (μ_R, μ_F) and of the kinematics.

Incoming partons emit QCD radiation, known as *Initial State Radiation* (ISR), while the outgoing partons, following the same mechanism emit the so-called *Final State Radiation* (FSR). Both ISR and FSR are emitted in the form of gluons. Incoming and outgoing charged particles also emit QED radiation, i.e photons. The spectators may produce secondary interactions; these additional interactions from the residual partons of the original protons are known as multiple interactions. Particles from ISR, FSR and the debris of the hard scattering along with multiple interactions are known as the *Underlying Event* (UE). Figure 1.2 shows a sketch of the notions described above.

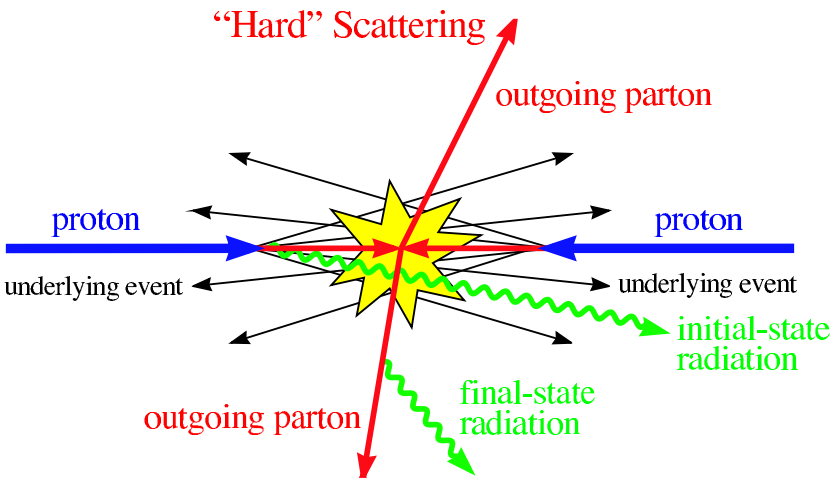

Figure 1.2: Schematic representation of a $2 \to 2$ hard scattering event. Figure taken from [4].

[6]The fact that the gluons are massless introduces QCD UV divergencies that lead to infinities in the cross-sections calculations. In order to avoid such unphysical results, a renormalisation procedure is introduced and the scale at which this procedure is done is called the *renormalisation scale*, μ_R.

1.4 $W^{\pm}Z$ analysis motivation

At the LHC the dominant $W^{\pm}Z$ production mechanism is from quark-antiquark initial states. Figure 1.3 shows the leading-order Feynman diagrams for $W^{\pm}Z$ production from $q\bar{q}$ initial states.

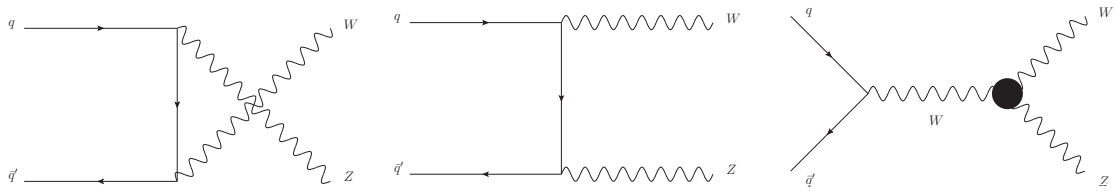

Figure 1.3: The SM tree-level Feynman diagrams for $W^{\pm}Z$ production through the $q\bar{q}'$ initial state in hadron colliders. The s-channel diagram contains the WWZ TGC vertex.

Next-to-leading-order (NLO) contributions include the quark-gluon (antiquark-gluon) processes which result in the presence of an additional quark in the final state, along with the Feynman diagrams with virtual corrections. Finally, NNLO corrections result in the presence of at least two jets in the final state.

The measurement of the $W^{\pm}Z$ production cross-section can be done in a variety of final states: from the fully leptonic to the semi-leptonic and to the pure hadronic final state. The fact that this analysis utilizes the fully leptonic final state, that represents a small fraction of the inclusive cross-section, is based on the clean signature of the leptons along with the low background.

The di-boson $W^{\pm}Z$ production at the LHC is of great interest since it is an excellent probe of the ElectroWeak sector. The cross-sections are precisely predicted by the SM and their dependence on the centre-of-mass-energy in known; therefore, any deviation from these predictions may be an indication of New Physics, both affecting the cross-section itself as well as the kinematic distributions.

Bibliography

[1] F. Halzen and A. D. Martin, *QUARKS AND LEPTONS: AN INTRODUCTORY COURSE IN MODERN PARTICLE PHYSICS*. 1984.

[2] D. Griffiths, *Introduction to Elementary Particles*. Wiley VCH (1987).

[3] R. K. Ellis, W. J. Stirling, and B. R. Webber, *QCD and collider physics*. Camb. Monogr. Part. Phys. Nucl. Phys. Cosmol. 8 (1996).

[4] J. M. Campbell, J. Huston, and W. Stirling, *Hard Interactions of Quarks and Gluons: A Primer for LHC Physics*, Rept.Prog.Phys. **70** (2007) 89, arXiv:hep-ph/0611148 [hep-ph].

[5] W. Buchmuller and C. Ludeling, *Field Theory and Standard Model*, arXiv:hep-ph/0609174 [hep-ph].

Chapter 2

The Large Hadron Collider

Scattering experiments are for more than a century the best (and only) means to explore the structure of matter. Rutherford's analysis on the Geiger-Marsden α-particles experiment in 1909, led to the breakthrough discovery of the nucleus; ever since numerous devices and techniques have been developed in order to achieve higher energies, necessary for studies at subatomic level. The need for higher energies can be related to:

1. de Broglie's realisation that particles of momentum p are associated with a wavelength λ, via:

$$\lambda = h/p \ , \tag{2.1}$$

   where h is Planck's constant, $h = 6.636 \cdot 10^{-34}$ J·s.

2. The fact that resolution improves as wavelength λ falls, therefore as energy (momentum) rises.

Starting from low-energies particles (at the order of MeV) coming from a natural radioactive source and from table-top accelerators, like the first cyclotron invented by Lawrence in 1925, Figure 2.1, we are today at the TeV scale and to huge, multi-billion euros accelerators such as the Large Hadron Collider (LHC) [1] situated at the European Centre for Nuclear Research (CERN).

However, this picture of a collider as a microscope to observe matter is rather naive; the most crucial parameter in High Energy Physics experiments is the available energy at the centre of mass system (E_{cms}); energy is Nature's currency and it can be converted to mass. An obvious consequence of this realisation is that as the available energy rises, processes and

Figure 2.1: Lawrence's cyclotron [Courtesy of University of California, Berkeley] (left), aerial view of LHC [Courtesy of Lawrence Livermore National Laboratory] (right). The dotted line depicts the Franco-Swiss borders while the full white circles represent the interaction points where the four major LHC experiments are installed.

theoretical models that involve heavier particles can be studied and verified (or discarded). Such processes, at the time the LHC became operational included the Higgs mechanism (with the recently observed Higgs boson), as well as searches for SuperSymmetric particles (until the time of this thesis no SuperSymmetric particle has been observed).

The other crucial parameter that is used in order to quantify the performance of a collider is the number of events it can produce, for a process of given cross-section, in a certain time period. This parameter is the luminosity and it is evident that for rare processes with small production cross-sections a high luminosity is an essential factor.

In the following, a brief description of the operational parameters of LHC is given.

2.1 Operational parameters

LHC is the largest hadron collider in the world with a circumference of 26.7 km capable to accelerate and collide protons that circulate in two counter-rotating beams comprised of 2808 bunches each and with approximately 10^{11} protons per beam. Apart from protons, LHC has a complementary Physics program that uses lead ($^{208}_{82}Pb^{+}$) ion collisions. The design operational energy is 7 TeV per proton (2.76 TeV per $^{208}_{82}Pb^{+}$ nucleon), while the peak instantaneous luminosity is $10^{34}[cm^{-2}s^{-1}]$. LHC is installed in CERN's previous accelerator (LEP) tunnel, in a depth varying from 45 to 150 m below ground[1]. LHC operational parameters are listed in Table 2.1.

[1]In order to avoid the cost of property expropriation, as well as for radiation shielding reasons.

Circumference	26.67 km
Proton beam energy	7 TeV
Number of bunches per beam	2808
Number of particles per bunch	$1.15 \cdot 10^{11}$
Circulating beam current	0.584 A
RMS of bunch length	75.5 mm
Bunch radius $\sigma_x = \sigma_y$	16 μm
Peak luminosity	10^{34} cm^{-2} s^{-1}
Collision time interval	24.95 ns
Number of dipoles	1232
Number of quadrapoles	392
Field of dipoles	8.33 T
Temperature of dipoles	1.9 K

Table 2.1: LHC basic operational parameters.

The maximum energy a hadron can gain is limited by the radius of the (already existing LEP) tunnel; Equation 2.2 relates the radius of curvature R of an accelerating charged particle to it's momentum p and the magnetic field used in order to bend it's path:

$$p[GeV/c] \approx 0.3 \cdot B[T] \cdot R[m] \tag{2.2}$$

The LHC machine is able to provide energies higher than 7 TeV per proton; however, from equation 2.2 it is evident that the maximum momentum a particle can gain is limited by the bending power of the magnetic field, B.

In order to bend particles with energy of 7 TeV, a magnetic field of 8.33 T is required, which is achieved by means of superconductivity. For this purpose, alloys of Nb and Ti are used operating at a temperature of 1.9 K, achieved by a powerful cryogenic system that circulates 120 tons of super-fluid liquid Helium inside the LHC dipole magnets, responsible for the bending of the proton beams. Since the LHC accelerates protons in two counter-rotating beams orbiting in the same ring, the magnet system is designed to incorporate the two opposite fields in the same structure. This is possible via a twin-aperture dipole magnet, that comprises of two sets of coils generating opposing magnetic fields, for the acceleration of same charge particles that move in opposite directions. Both sets of coils are housed in the same structure and use the same cryostat. Figure 2.2 shows the dipole magnets structure, while in Figure 2.3 the dynamic lines of the magnetic field produced by a quarter of a dipole aperture are drawn.

Figure 2.2: Inner structure of a dipole magnet. The two holes in the center are the beam pipes. LHC uses 1232 of these 15-meter long dipole magnets, responsible for the bending of the proton beams.

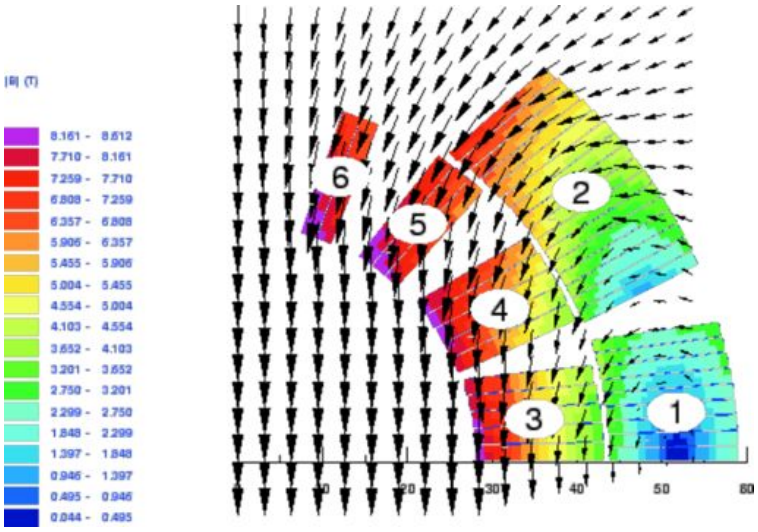

Figure 2.3: A quarter of a dipole aperture showing the 6 superconducting blocks and the magnetic field produced.

Apart from the (1232) 15-meter long dipole magnets used for the bending of the protons, LHC uses a large variety of other magnets, from the protons extraction from hydrogen atoms, up to the point they collide. Essential for the beams stability and precise alignment are quadrapole (392), sextupole (688) and octupole (168) magnets which squeeze and tighten the beams making them narrower by 12.5 times, from 0.2 mm down to 16 μm across and from a few mms to 4 μm wide.

2.2 The proton life cycle

It all starts with a hydrogen bottle. Protons are stripped off their electron and are accelerated to 90 keV by a radio frequency quadrapole (RFQ2). A series of accelerators (linear along with synchrotrons) work in chain until protons reach their final energy of 7 TeV. At first they are fed to a linear accelerator, namely LINO2, which boosts them to 50 MeV. Protons are then injected to the circular booster, called Proton Synchrotron Booster (PSB), where they reach 1.4 GeV. The PS also squeezes the bunches down, so that their cross-section is smaller. At the next step they are accelerated by the Proton Synchrotron (PS) up to 25 GeV. Then the Super Proton Synchrotron (SSS) takes over to further accelerate them up to 450 GeV before they are fed to LHC who takes over for the final step of the acceleration.

When protons ramp up to their nominal energy and stable beams are declared, they intersect at four predefined points where the major LHC experiments are istalled. These are (in alphabetical order):

- **ALICE** [2] (**A** **L**arge **I**on **C**ollider **E**xperiment): A 10,000-tonne detector dedicated to the study of the quark-gluon plasma.
- **ATLAS** [3] (**A** **T**orroidal **LHC** **A**pparatu**S**): A general purpose experiment, designed for a wide range of Physics searches as well as precision measurements. A more detailed description of the ATLAS detector is given in chapter 3.
- **CMS** [4] (**C**ompact **M**uon **S**olenoid): Along with ATLAS, CMS can detect a wide variety of phenomena, providing complementary measurements to ATLAS.
- **LHCb** [5], dedicated to b-physics studies, focusing on CP violation and searches for rare decays of B-mesons.

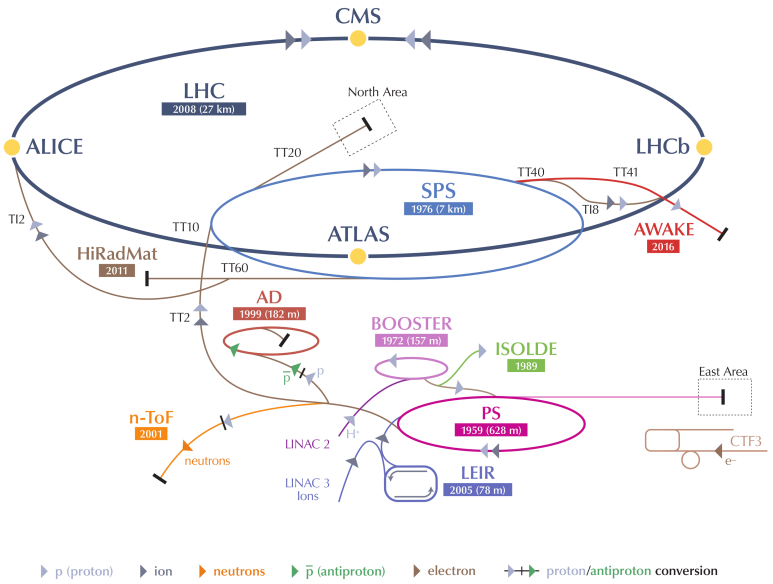

Figure 2.4: The LHC accelerator complex. LINAC2, PSB, PS, and SPS are used in a chain before feeding the protons to LHC. Filled yellow circles depicts the points where the four major LHC experiments are installed.

Three more experiments that operate within the LHC context are LHCf [6] (an experiment dedicated to the study of simulated cosmic rays in laboratory conditions, comprised of two detectors sitting along the LHC beam-line, at 140 m either-side the ATLAS collision point), TOTEM [7] (Total Cross Section, Elastic Scattering and Diffraction Dissociation at the LHC) and MoEDAL [8] (Monopole & Exotics Detector at the LHC, dedicated to monopole and exotic searches such as the Dyon or Stable Massive Particles).

The acceleration scheme, along with the points where the four major LHC experiments are situated, is pictorially represented in Figure 2.4.

2.3 Luminosity

There is a relation between the event rate $\delta R/\delta t$, the number of interactions or events per second and the cross-section σ_{int}, the likelihood of these interactions in pp collisions:

$$\delta R/\delta t = \mathscr{L} \cdot \sigma_{int} \ , \tag{2.3}$$

where $\mathscr{L}$ is the proportionality factor, namely luminosity and it is measured in $\mathrm{cm}^{-2}\mathrm{s}^{-1}$.

For a given E_{cms}, σ_{int} is known; the rate then is directly proportional to $\mathscr{L}$. Luminosity estimations [9] can be performed using pp inelastic collisions. Luminosity can be expressed as:

$$\mathscr{L} = \frac{N_1 N_2 n_1 n_2}{4\pi\sigma_x\sigma y} f_{rev} \tag{2.4}$$

where:

- N_i: number of protons in each bunch (i=1,2)
- n_i: number of bunches in each beam (i=1,2)
- f_{rev}: revolving frequency of the bunches
- σ_j: Gaussian transverse beam profiles in the horizontal (bend) and vertical directions (j=x,y)

The σ_x, σ_y profiles can be known through a process called *van der Meer* scans [10] (or simply luminosity scans). In this process the beams are moved against each other both in the x- and y- coordinates in known steps so that they partially overlap; interaction rates are then measured as a function of the separation in each coordinate. By fitting the resulting Gaussian distributions, which have the maximum interaction rates at zero separation, the σ_x, σ_y values are extracted.

A variety of luminosity measurements detectors is used in the ATLAS experiment; Table 2.2 lists the technologies used and the systems distances from the Interaction Point (IP).

Detector	IP distance	Type
ZDC	±140 m	Calorimeter
BCM	±184 cm	Diamond
MBTS	±365 cm	Scintillators
LUCID	±17 m	Cherenkov (gas)

Table 2.2: ATLAS luminosity determination detector technologies and their distance from the IP.

The number of protons in the bunches decreases as a function of the number of collisions (and thus of the time), as seen in Figure 2.6. After a period of a few hours (about 10) the beams are controllable dumped and the LHC is prepared for the next fill.

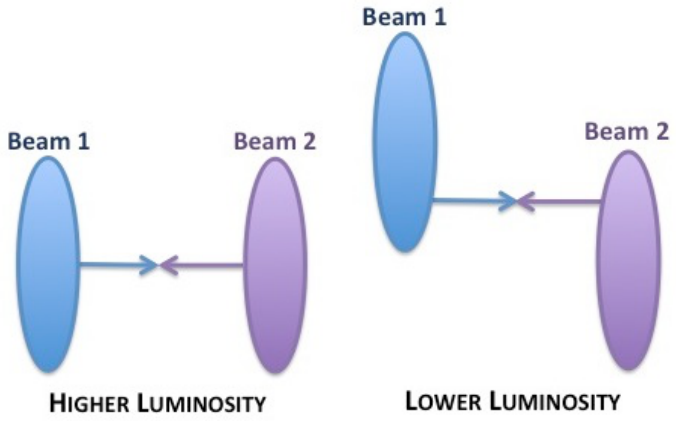

Figure 2.5: High luminosity conditions with large cross-section for pp interactions (left). Low luminosity conditions can be achieved by displacing the beams with respect to each other (right) [Courtesy of quantumdiaries.org].

Another important aspect is the luminosity levelling. Not all experiments are designed to operate at the same luminosity conditions; ATLAS and CMS are able to cope with the rate of collisions that corresponds to an instantaneous luminosity of 10^{34} [$cm^{-2}s^{-1}$]. However, LHCb and ALICE are not; for LHCb the design luminosity conditions vary from $2{\cdot}10^{32}$-$3{\cdot}10^{32}$ [$cm^{-2}s^{-1}$], while for ALICE the corresponding conditions are $5{\cdot}10^{29}$-$5{\cdot}10^{30}$ [$cm^{-2}s^{-1}$]. LHC operators are therefore forced to adjust the colliding conditions among the four experiments and this can be done by either

- having a different number of proton bunches colliding at each of the interaction points. However, this colliding scheme was suitable only at the beginning of the operation of LHC, where luminosity has not reached high levels.
- means of "Luminosity levelling", i.e by moving the proton beams relative to each other so that the cross-section is reduced; this is pictorially represented in Figure 2.5.

2.4 The future of LHC

As of February 2013 the LHC has stopped its operations, after 3 years of excellent performance, having delivered a total of 5.46 fb^{-1} of E_{cms} 7 TeV and 22.8 fb^{-1} of E_{cms} 8 TeV data, from which 4.57 and 20.3 respectively are available for Physics analyses within the ATLAS experiment, Figure 2.7. The LHC has scheduled a long (currently ongoing)

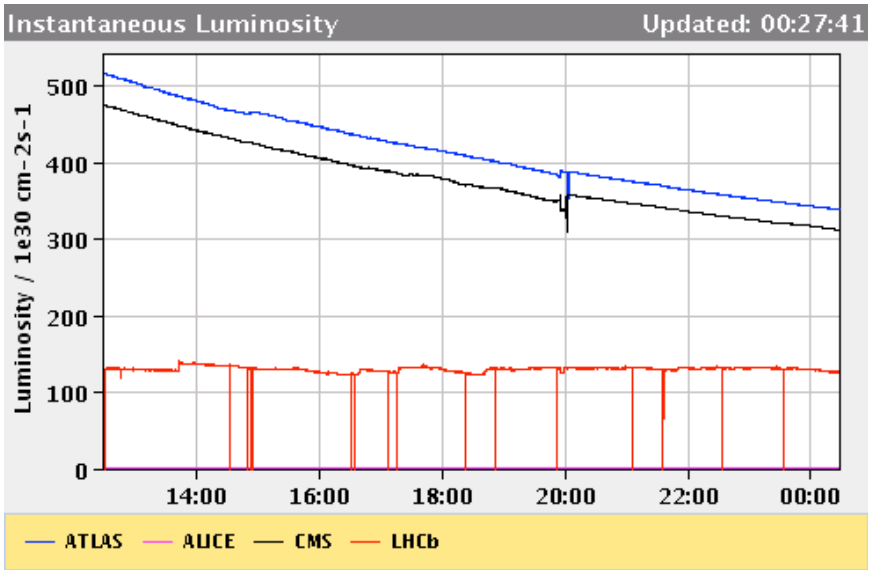

Figure 2.6: Instantaneous luminosity as a function of time. The legend shows the instantaneous luminosity as recorded by each of the four major LHC experiments [Courtesy of quantumdiaries.org].

shutdown period[2] in order to prepare for the energy and luminosity upgrades at $\sqrt{s}$=13∼14 TeV and 10^{34}[cm^{-2}s^{-1}] respectively of the next run period, namely Run II. Then a long data-taking period until the end of 2017 is foreseen, expected to yield ∼75-100 fb^{-1}. 2018 is scheduled to be the second upgrade interval[3] where the luminosity is expected to double, reaching $2{\cdot}10^{34}$ and the energy to be fixed at $\sqrt{s}$=14 TeV, Figure 2.8. 2019-2022 will be the Run III data-taking period that is expected to deliver ∼ 350 fb^{-1} followed by the last upgrading period[4] which will further upgrade the luminosity to $5 \cdot 10^{34}$ [cm^{-2}s^{-1}]. The final period of the LHC operation is estimated to begin in 2023 and it is scheduled to run until approximately 2030, providing a total foreseen data yield of ∼3000 fb^{-1}.

[2]LS1, estimated to last until the end of 2014.

[3]LS2, estimated to last until mid 2018.

[4]LS3, estimated to last until mid 2019.

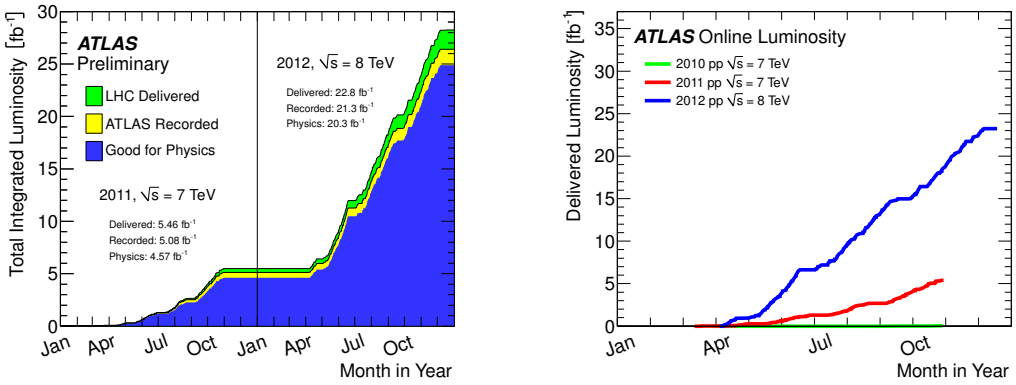

Figure 2.7: Total integrated luminosity vs time for 2011 and 2012 data taking periods. The ATLAS detector performed with an average efficiency of 93.2% in 2011 and 2012 (left). Total delivered luminosity for all data taking periods since the LHC begun operations (right).

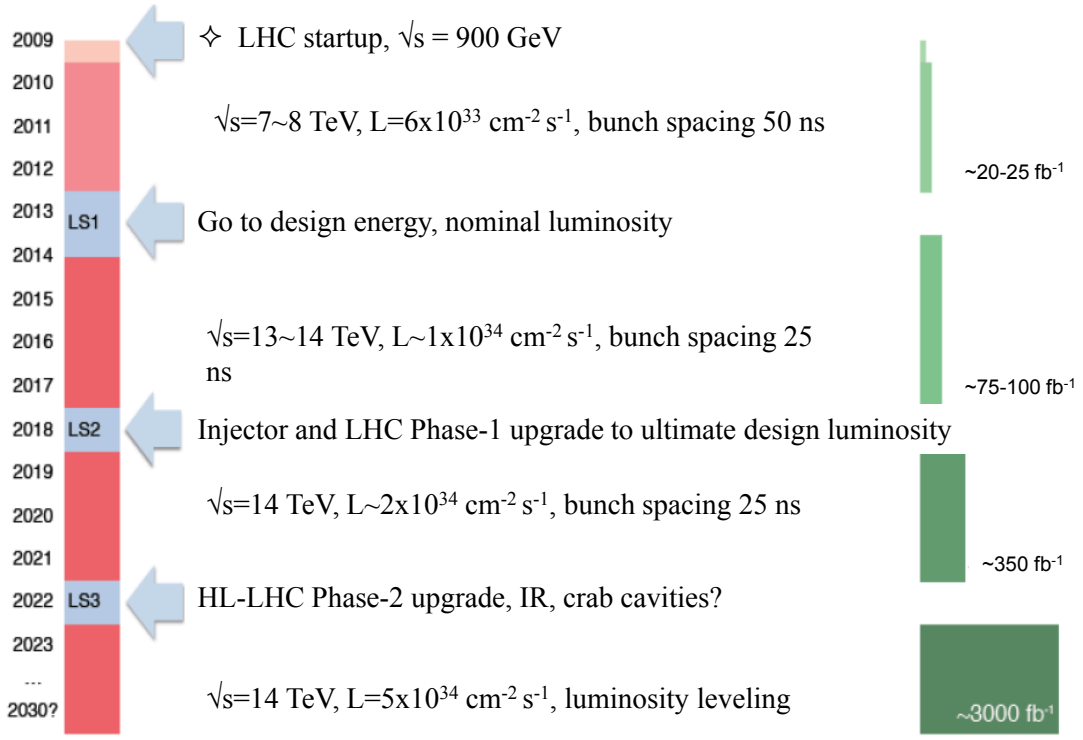

Figure 2.8: Time-line of the LHC and ATLAS detector operations and upgrades for the time period 2009-2030 [11].

Bibliography

[1] O. S. Bruning, P. Collier, P. Lebrun, S. Myers, R. Ostojic, et al., *LHC Design Report. 1. The LHC Main Ring,*.

[2] ALICE Collaboration, K. Aamodt et al., *The ALICE experiment at the CERN LHC*, JINST **3** (2008) S08002.

[3] ATLAS Collaboration, G. Aad et al., *The ATLAS Experiment at the CERN Large Hadron Collider*, JINST **3** (2008) S08003.

[4] CMS Collaboration, S. Chatrchyan et al., *The CMS experiment at the CERN LHC*, JINST **3** (2008) S08004.

[5] LHCb Collaboration, J. Alves, A. Augusto et al., *The LHCb Detector at the LHC*, JINST **3** (2008) S08005.

[6] LHCf Collaboration, O. Adriani et al., *The LHCf detector at the CERN Large Hadron Collider*, JINST **3** (2008) S08006.

[7] TOTEM Collaboration, G. Anelli et al., *The TOTEM experiment at the CERN Large Hadron Collider*, JINST **3** (2008) S08007.

[8] J. L. Pinfold, *The MoEDAL Experiment at the LHC*, EPJ Web Conf. **71** (2014) 00111.

[9] ATLAS Collaboration, G. Aad et al., *Improved luminosity determination in pp collisions at $\sqrt{s}$ = 7 TeV using the ATLAS detector at the LHC*, Eur.Phys.J. **C73** (2013) 2518, arXiv:1302.4393 [hep-ex].

[10] S. van der Meer. ISR-PO/68-31, KEK68-64.

[11] https://indico.cern.ch/event/219327/.

Chapter 3

The ATLAS detector

The LHC Physics potential motivated the design and construction of the ATLAS detector [1–3] as a multi-purpose experiment, not dedicated to a single goal, but suitable for a large variety of Physics tasks, such as the probing of the EW sector of the SM, the quest for the Higgs boson and BSM searches. ATLAS is the largest volume detector, with a cylindrical geometry of 25 m diameter and 46 m length, weighting over 7000 t and with almost 4π solid angle coverage. Table 3.1 lists the basic parameters of the ATLAS detector. The ATLAS experiment time span ranges from the late 1980s when it was first conceived[1], until 2030 when the LHC is estimated to stop operations. Today, more than 3000 scientists from 165 institutions around the world are involved in the ATLAS experiment. Figure 3.1 shows a sketch of the ATLAS detector.

Length	46 m
Diameter	25 m
Weight	7000 t
Coverage	4π
Channels	100 M
Cables	3000 km
Depth	93 m
Construction cost	550 M CHF
Data (per year)	3.2 PB

Table 3.1: ATLAS basic parameters.

[1]Important milestones: 1992-Letter of Intend, 1993-Technical Design Report, 1997-Construction begins, 2003-Installation on the pit.

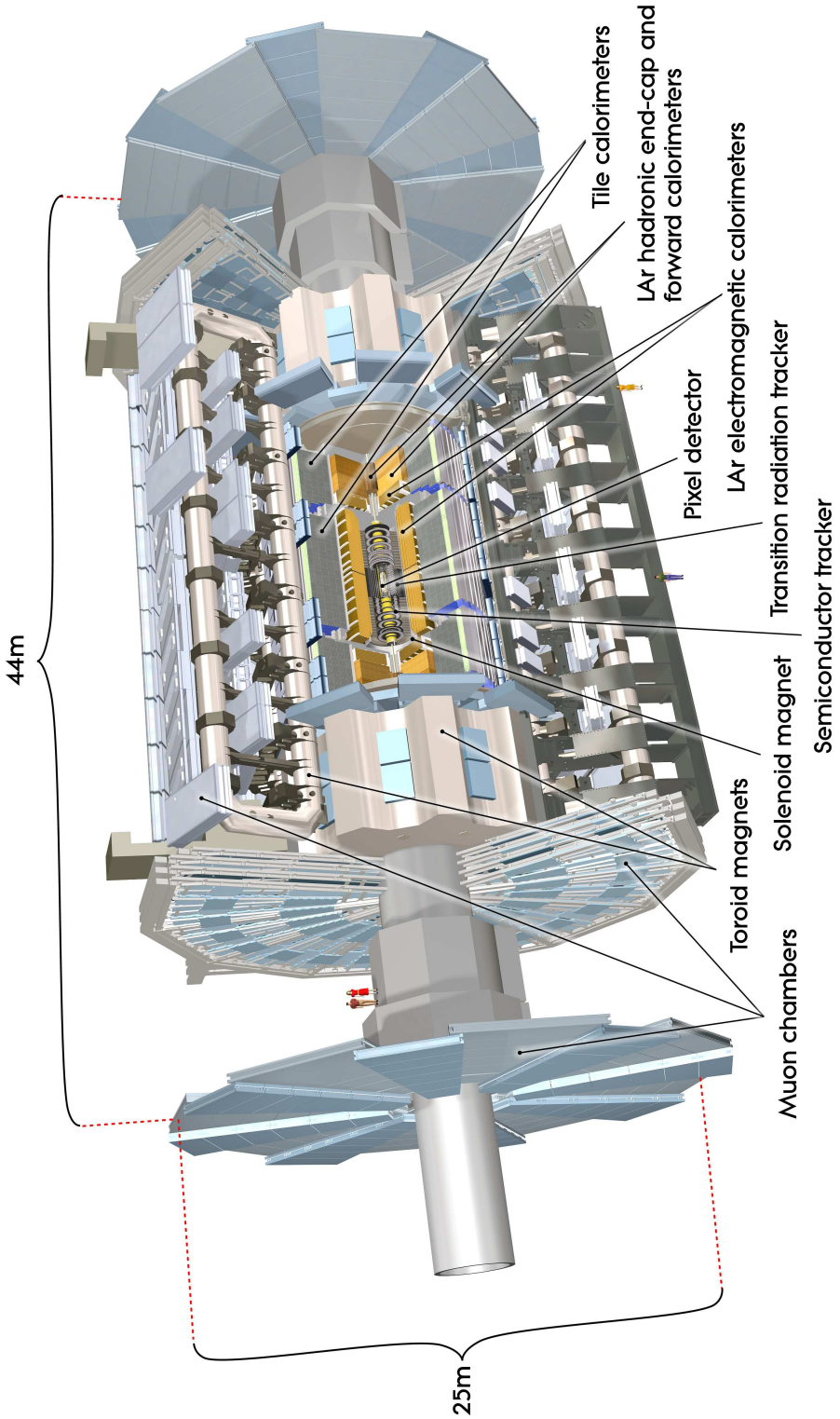

Figure 3.1: A cut-view 3-D sketch of the ATLAS detector.

3.1 Coordinates system

Throughout the ATLAS experiment a right-handed coordinates system is used which originates at the interaction point (IP) where the pp collisions take place. The beam direction defines the z-axis; the x-axis is perpendicular to the z-axis with it's positive direction pointing at the center of the LHC ring, while the y axis is perpendicular in turn to the plane defined by the x- and z-axis, pointing upwards. An illustration of the coordinates system is given in Figure 3.2. In polar coordinates system, θ ($\in [0, \pi]$) and ϕ ($\in [-\pi, \pi]$) define the polar and azimuth angles from and around the z-axis respectively. The x-y plane, perpendicular to the beam line is defined as the transverse plane.

In most of the cases, observables like momentum P are given in the transverse plane (energy is not a vector; however, the corresponding energy to the p_{T} is defined as the E_{T}). It is therefore useful to define the transverse components of these quantities as:

$$p_{\mathrm{T}} = P \cdot \sin\theta, \; E_{\mathrm{T}} = E \cdot \sin\theta \; . \tag{3.1}$$

Two more important quantities are the rapidity and pseudo-rapidity, defined by:

$$y = \frac{1}{2} log \frac{E + p_{\mathrm{z}}}{E - p_{\mathrm{z}}}, \; \eta = -ln(tan\frac{\theta}{2}) \; , \tag{3.2}$$

where y is a Lorentz-invariant quantity which, at the limit of very small masses and relativistic energies, can be transformed to a function of θ. Pseudo-rapidity η and the azimuth angle ϕ define a plane, in which the metric is Euclidean and consequently can be expressed as:

$$\Delta R = \sqrt{\Delta\eta^2 + \Delta\phi^2}, \tag{3.3}$$

where $\Delta\eta = |\eta_1 - \eta_2|$ and $\Delta\phi = |\phi_1 - \phi_2| - \kappa \cdot 2\pi$, with κ =+1 if $|\phi_1 - \phi_2| > \pi$ and κ =0 otherwise.

3.2 Detector subsystems

The ATLAS detector comprises four major subsystems, the Magnet System (MagSys), the Inner Detector (ID), the Calorimeter System (CS), and the Muon Spectrometer (MS). A more detailed description for each one of the aforementioned subsystems is given in the following sections, while in table 3.2 a description of the resolution and the geometrical coverage in η for the ID, the CS and the MS systems is given.

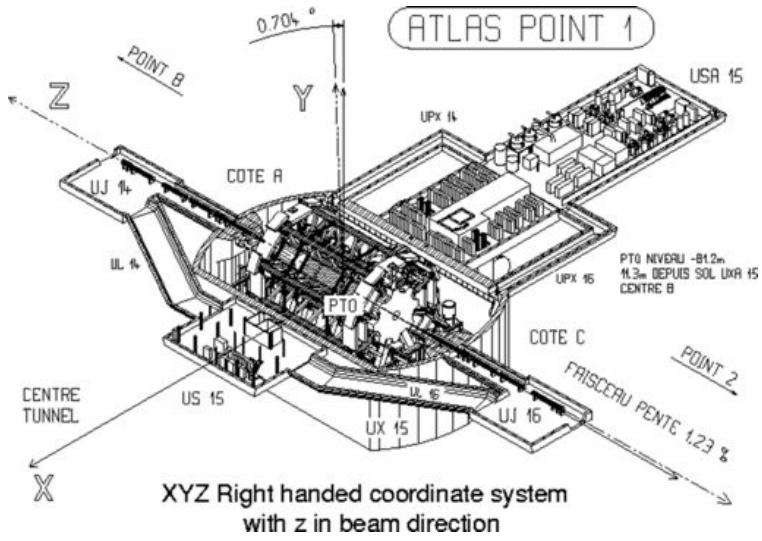

Figure 3.2: The ATLAS detector coordinates system. The transverse to the beam plane is defined by the x- and y-axis.

Subsystem	Resolution	η coverage
Inner Detector	$\sigma_{p_T}/p_T = 0.05\% \oplus 1\%$	± 2.5
E/M Calorimeter	$\sigma_E/E = 10\%/\sqrt{E} \oplus 0.7\%$	± 3.2
Hadronic Calorimeter		
Barrel/End Cap	$\sigma_E/E = 50\%/\sqrt{E} \oplus 3\%$	± 3.2
Forward	$\sigma_E/E = 100\%/\sqrt{E} \oplus 10\%$	$3.1 < \lvert\eta\rvert < \pm 4.9$
Muon Spectrometer	$\sigma_{p_T}/p_T = 10\%$ at p_T =1 TeV	± 2.7

Table 3.2: ATLAS subsystems resolution and geometrical (η) coverage.

3.2.1 Magnet System

The ATLAS MagSys comprises of a superconducting central solenoid and three superconducting toroid magnets (one in the barrel and two in the end-cap regions), for the bending of charged particles trajectories and the measurement of their momentum in the ID and MS subsystems. It expands axially to 26 m, radially to 22 m, operates at 4.5 K and the total energy stored in it rises up to 1.6 GJ. Figure 3.3 shows the solenoid and a sketch of the three toroids deployed in the ATLAS detector, while figure Fig 3.4 shows the barrel air-core toroid magnet.

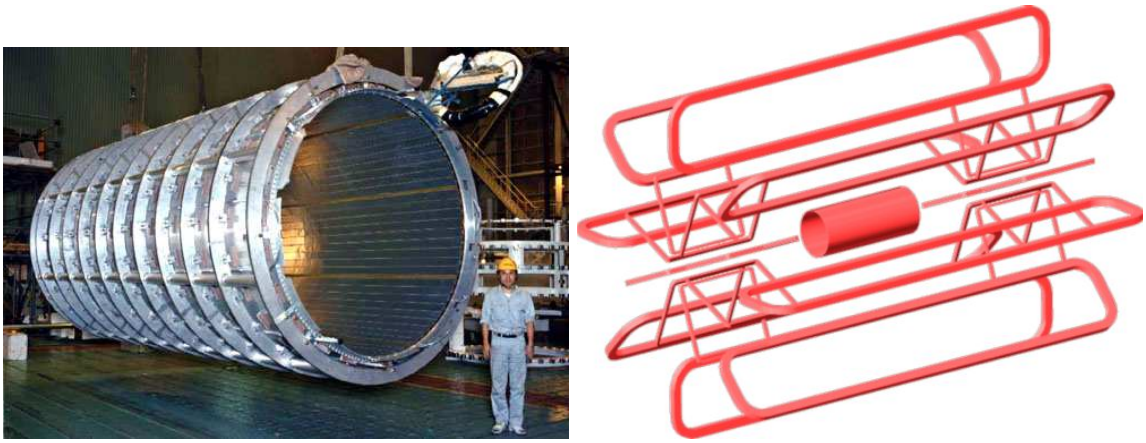

Figure 3.3: The central solenoid before installation (left). A sketch of the magnet systems deployed for the ATLAS experiment (right).

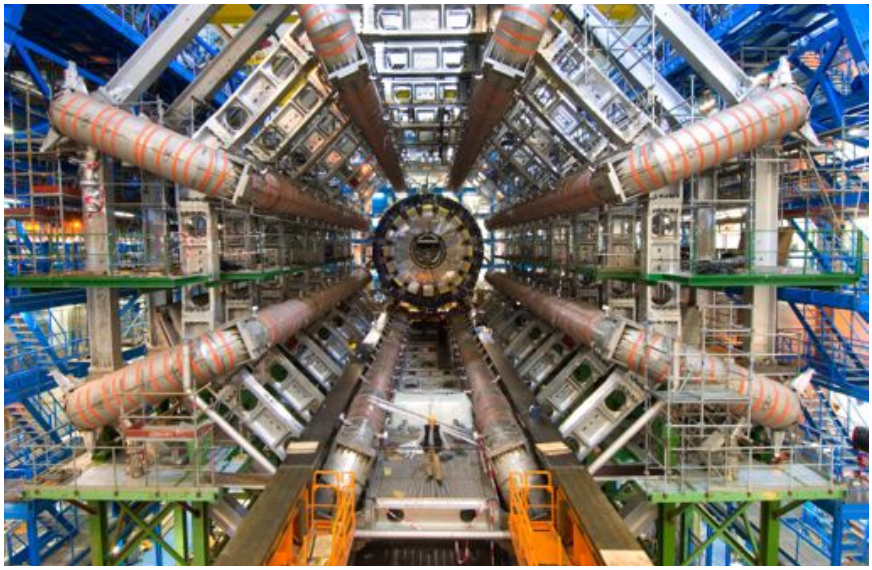

Figure 3.4: The barrel air-core toroid. The eight coils provide the magnetic field in the barrel region of the MS.

Central Solenoid

The 5.8 m long central solenoid is a single layer coil wounded on the inside of a thick cylinder, spanning radially from 1.23 m to 1.28 m and it is able to provide a magnetic field of 2 T at the center and 0.5 T at the edges, when operating at the nominal current of 7.73 kA. In the design of the solenoid emphasis was given in minimizing the material in front of the CS, resulting in a contribution of approximately 0.66 radiation lengths[2]. The magnetic field lines are parallel to the beam axis, so that the bending of the trajectories occurs in the ϕ-direction, while the flux of the field is returned via the steel of the HC.

Air-core toroid

The air-core toroid barrel part extends radially from 9.4 m up to 20.1 m while it has a length of 25.3 m. It consists of 8 coils surrounding the beam axis and it is situated around the CS. The end-cap toroids are inserted at the barrel at each end of the central solenoid and they are rotated by 22.5° with respect to the barrel toroid coil in order to optimise the bending power at the transition region between the two coil systems. The field produced by the barrel toroid is 0.5 T while at the end-caps it rises up to 1 T. All three toroids share the same technology of winding pure Al-stabilized Nb/Ti/Cu conductor and their nominal current is 20.5 kA. The field lines are in the ϕ-direction so that the bending of the trajectories is on the η-direction. Figure 3.5 shows one of the end-cap magnets and Figure 3.6 the magnetic field produced by the three toroids for the bending of the muons trajectories in the MS.

3.2.2 Inner detector

The ID is the innermost part of the ATLAS detector and it has three main goals: Particle identification, momenta measurements and primary (as well as secondary) vertex[3] measurements for charged tracks above a p_{T} threshold[4] and within $|\eta|$ <2.5. It has a cylinder

[2]For this purpose the solenoid windings and the LAr calorimeter share the same cryogenic system.

[3]A vertex is defined as the common point from which reconstructed tracks originate; The primary vertex of the pp collision will contain most of the reconstructed tracks. As multiple pp collisions may occur in a given bunch crossing, it is possible that many primary vertices may be reconstructed per event. These will be constrained by the beam spot, which is the region defined by the geometrical properties of the proton beams.

[4]Nominal value: 0.5 GeV but as low as 0.1 GeV in some initial measurements with minimum-bias events.

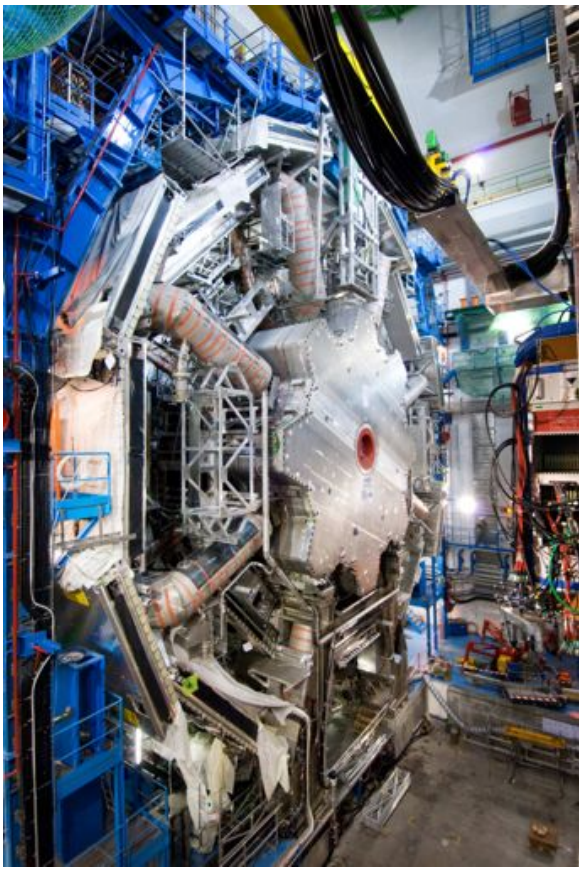

Figure 3.5: End-cap toroid installed at the ATLAS cavern.

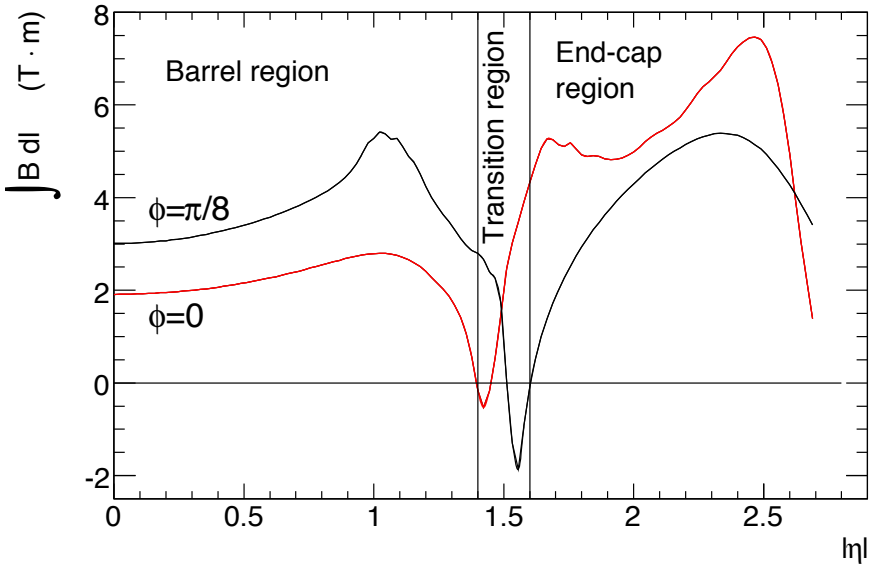

Figure 3.6: Predicted field integral as a function of $|\eta|$ from the innermost to the outermost MDT layer in one toroid octant, for infinite-momentum muons. The curves correspond to the azimuth angles ϕ=0 (red) and ϕ=$\pi/8$ (black) (right).

form with 7 m length and radius 1.15 m and it is immersed in a solenoid magnetic field of 2 T. Three sub-detectors comprise the ID, namely the Pixel detector, the Semi-Conductor Tracker (SCT) and the Transition Radiation Tracker (TRT), depicted in Figure 3.7.

Pixel detector

The Pixel detector is the first component of the ID, closest to the IP. It is comprised of 50×400 μm^2 rectangles (pixels) and it utilises silicon as active material. The pixels are arranged in three concentric cylindrical layers in the barrel region, at radial distances from the IP of 50.5 mm, 88.5 mm and 122.5 mm, along with three disks on each of the end-caps, located at distances of 49.5 cm, 58.0 cm and 65.0 cm, perpendicular to the beam axis (Figure 3.8). There are 1744 pixel silicon modules with an active area for each one of them of 16.4 × 60.8 mm^2. Every module contains 47232 pixels that provide an accuracy of 50 μm in the R-ϕ plane and 400 μm in the z-direction. The Pixel detector has a coverage of $|\eta| < 2.5$ and it provides precision measurements due to its high granularity, while it has more than 80% of the electronics of the ATLAS experiment (80.4 million channels).

During the LS1 upgrade period, the Pixel detector will be enhanced with an extra layer, next to the IP, the Insertable B-Layer (IBL) [4]. The IBL is expected to further-

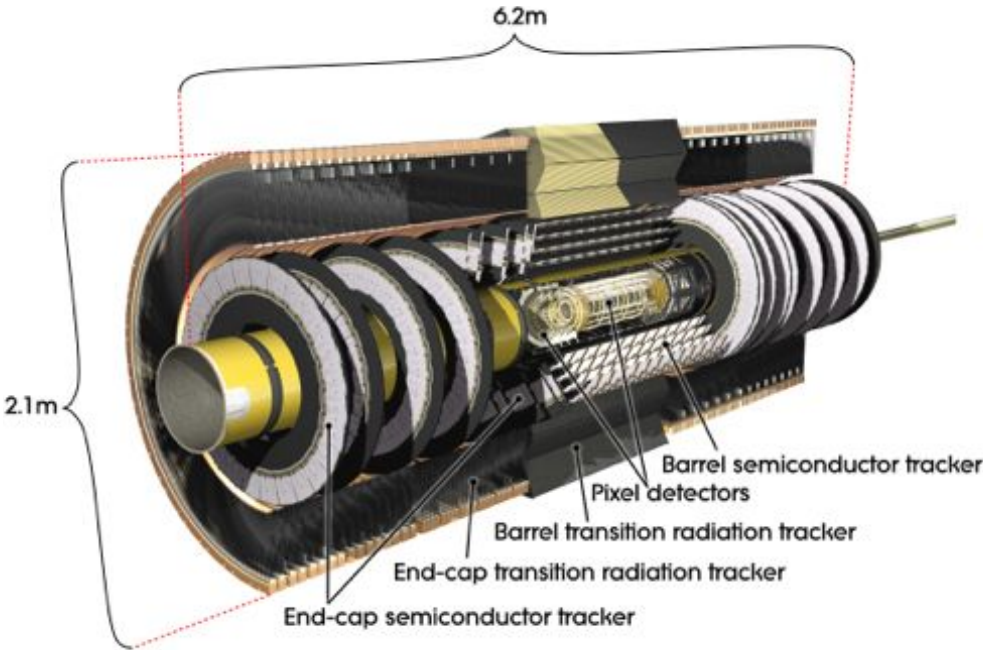

Figure 3.7: A cut-away view of the ATLAS Inner Detector, organized on concentric, cylindrical subsystems. The beam pipe is surrounded by the Pixel Detector, the middle part is the Semi-Conductor Tracker and the outer part is the Transistion Radiation Tracker.

more improve the resolution for tagging and vertexing in the high luminosity and radiation conditions of the next phase of LHC.

Semi-Conductor Tracker

The SCT is the next component of the ID and it also uses silicon as active material. It is arranged in four cylindrical layers in radial distances of 30, 37, 45 and 52 cm respectively in the barrel region and 9 disks on each end-cap, spanning from 85.4 to 272.0 cm in the z-axis and with an outer radius of 56 cm (Figure 3.8). The 4088 micro-strip wafers which comprise the SCT are glued together back-to-back and in a small solid angle of 40 $mrad$, thus allowing the determination of two coordinates in the R-ϕ plane. The design resolution of the SCT is 22 μm in the R-ϕ plane and 580 μm in the z-direction and it has 6.4 million readout electronic channels. The SCT operates complementary to the Pixel detector regarding the vertexing reconstruction and it also needs to function at a low temperature, around -7 $°C$, in order to avoid radiation damage as well as to reduce noise from leakage currents[5].

[5]Leakage currents emerge in the silicon bulk from thermal excitation

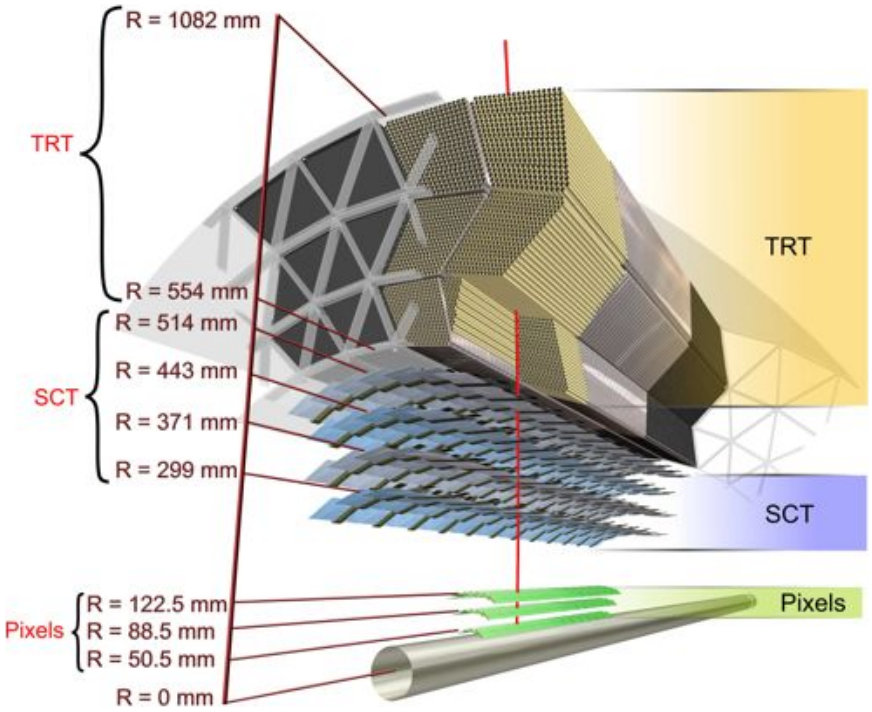

Figure 3.8: A sketch of the Inner Detector with the positions of the three sub-detectors comprising it. A track traversing all detectors is shown (red line).

Transition Radiation Tracker

The TRT is the outermost sub-detector of the ID, spanning in $|\eta|$ <2.0 and unlike the Pixel and the SCT, uses (instead of silicon) straws of 4 mm diameter and 144 mm length (37 mm in the end-caps), filled with a gaseous mixture of 70% Xe, 20% CO_2 and 10% CF_4 and containing a 31 μm diameter, gold-plated tungsten anode wire. The TRT is located radially from 56 to 107 cm (Figure 3.8), has an intrinsic resolution of 130 μm and there are approximately 351000 read-out electronic channels in it. In the barrel region the straws are placed parallel to the beam pipe, while in the end-cap regions they are arranged radially on wheels. Transition radiation, the radiation emitted by charged particles when they traverse the boundary between two substances of different dielectric properties, is the basis of TRT operation. Depending on the particle energy:

$$E = \gamma mc^2 \tag{3.4}$$

and using polypropylene fibers surrounding the straws, the TRT can discriminate between electrons and pions due to the different Lorentz factor they have, operating complementary

to the Electromagnetic Calorimeter (EC) in electron identification, especially in the low-energies regime.

3.2.3 Calorimeters

The CS rests between the ID and the MS and it its main purpose is to measure the energy of particles. This is achieved by interjecting material with which the particles interact and by absorbing their energy. High-density metal is used for this purpose while dedicated sub-detecting systems return information on the resulting particle shower shape, measuring thus the energy of the original incident particle. More precise, the CS system is used in the ATLAS experiment for:

- energy measurements of leptons and jets,
- determination of the missing transverse energy (E_T^{miss}),
- identification of particles from their shower shape and their longitudinal energy leakage and
- estimation of the spatial isolation of particles, which is extremely important for background suppression in Physics searches to channels with isolated leptons.

Muon measurements also benefit from the CS: Not only the CS limits the number of particles reaching the MS, but it also complements these measurements by providing corrections for the (small, in general) energy losses muons have in the CS system. This loss of energy for the muons in the CS sets the threshold for the lowest energy a muon can have in order to reach the MS. The CS is divided in three subsystems, the EM, the Hadronic Calorimeter (HC) and the Forward Calorimeter (FCal) covering all together the range up to $|\eta|$ <4.9. Figure 3.9 shows a schematics three-dimensional view of the CS.

ElectroMagnetic Calorimeter

The EC uses Liquid Argon (LAr) as active material and lead absorber plates over its full range and it is comprised of a barrel and two end-cap parts in the pseudorapidity regions of $|\eta|$ <1.475 and 1.375< $|\eta|$ <3.2 respectively. Accordion-shaped elements provide with symmetric coverage and lack of crack regions in ϕ, while the thickness of the lead plates was optimized as a function of η in terms of energy resolution. LAr is radiation tolerant

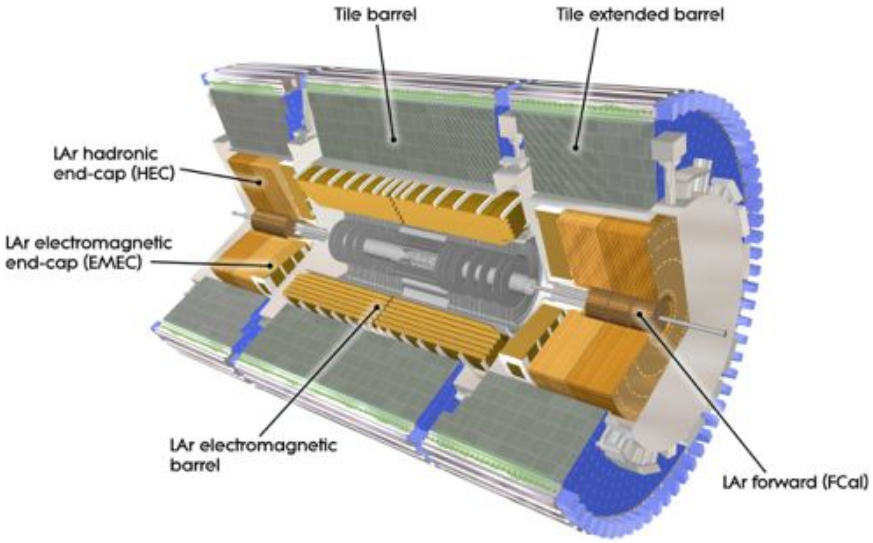

Figure 3.9: A cut-away view of the ATLAS CS.

and has linear response, while lead (due to its high atomic number) can provide sufficient signals from photons and electrons shower development.

In the common region of the EC and the ID, the EC is divided in three compartments, each of which is segmented in cells of different sizes. In the first compartment, closest to the IP, the cell granularity is $\Delta\eta \times \Delta\phi = 0.003 \times 0.1$, allowing precision measurements. The middle compartment has the highest thickness and a granularity of $\Delta\eta \times \Delta\phi = 0.025 \times 0.0245$, while the back compartment has a granularity of $\Delta\eta \times \Delta\phi = 0.05 \times 0.025$ with a varying thickness, depending on η. Finally, to account for energy losses due to the material in front of the CS, a thin layer of LAr, namely the PreSampler (PS) is used. The EC has a total of 190000 electronic channels and Figure 3.10 shows an illustration of an EC module.

Hadronic Calorimeter

Just like most of the ATLAS subsystems, the HC is divided into a barrel and two end-cap parts, covering the region of $|\eta|$ <4.9. It is responsible for jet [6] identification and reconstruction as well as for the determination of the E_T^{miss}, providing hermiticity in the high-η region. One of the most important aspects in the design of the thickness of the

[6] Jets occur in the process of hadronisation of partons, i.e quarks and gluons and can be regarded as a set of (mainly) hadrons and leptons originating from the same point.

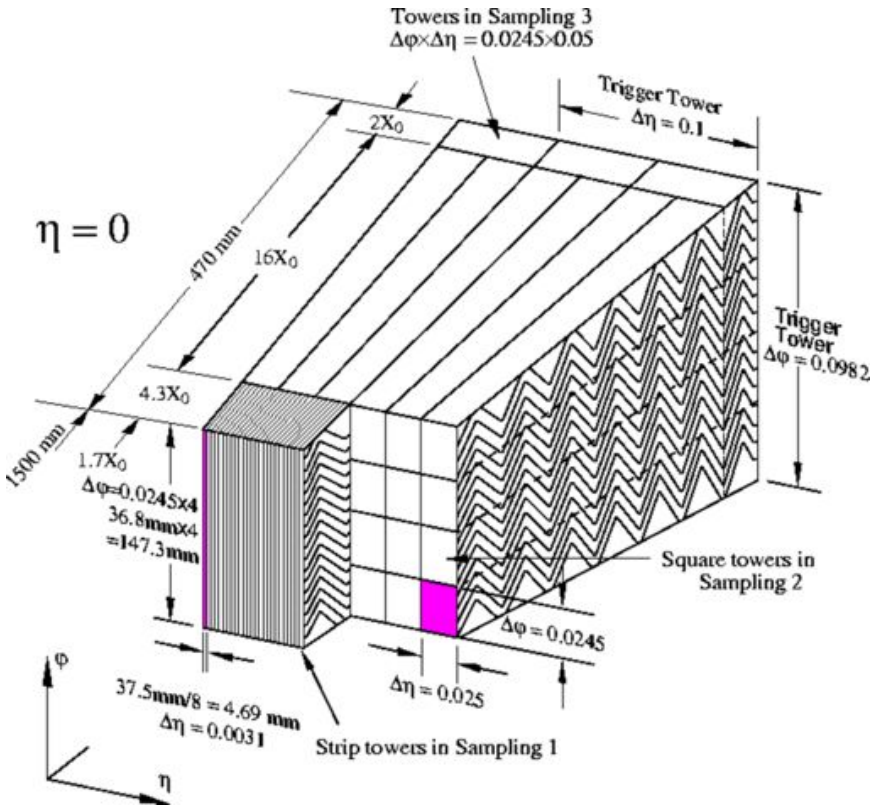

Figure 3.10: An EC module sketch, showing the three compartments and their granularity, along with the radiation lengths the material of each compartment corresponds to.

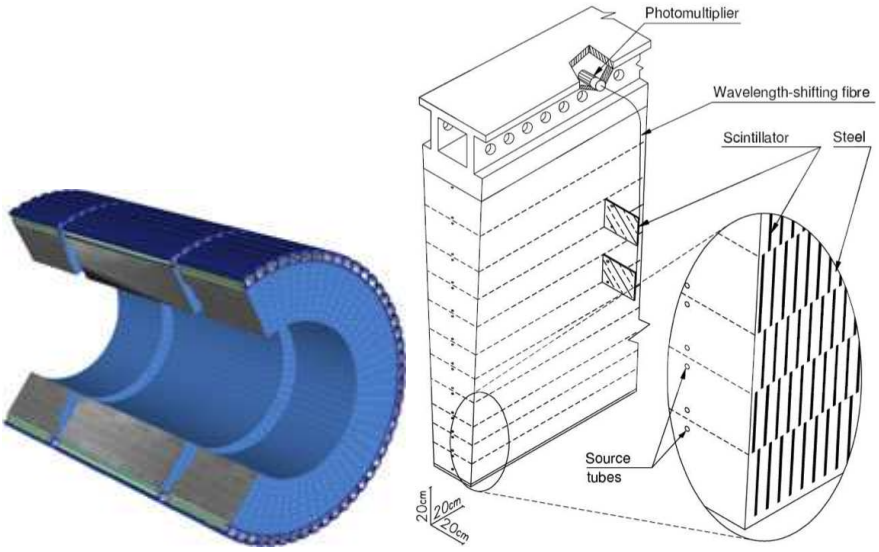

Figure 3.11: Layout of the TileCal (barrel and extended, left), a sketch of a module of the TileCal (right).

HC was based on the demand to contain hadronic showers and reduce the rate of punch-through hadrons[7] to the MS. It utilises tiles of plastic scintillator as active material with iron absorbers in the barrel part (Tile Hadronic Calorimeter, TileCal) while in the end-cap regions (HEC) the absorbing material is copper while the active material is LAr, due to the high radiation levels. Like the EC, it is segmented in three compartments of varying granularity. Figure 3.11 shows the TileCal along with a sketch of the modules comprising it.

Forward Calorimeter

The FCal cannot provide precision measurements of charged particles due to the fact that it is out the ID coverage. Still, it is a very useful component since it provides hermiticity in calorimetry for the determination of E_T^{miss}. It is segmented in three sections, utilises LAr as the active material due to the extreme radiation conditions in the area it rests and covers the range $3.1 < |\eta| < 4.9$. The absorber is copper in the first compartment and tungsten in the other two and the resulting thickness corresponds to approximately 10 radiation lengths.

[7]Punch-through hadrons can mimic muons in the MS contributing thus to misidentification and fake muon rates.

3.2.4 Muon Spectrometer

The MS is the outermost part of the ATLAS detector and its purpose is to measure muon momentum in the range of $|\eta|$ <2.7 as well as to trigger on them in the range of $|\eta|$ <2.4. It was designed for a performance in momentum resolution of approximately 10% for 1 TeV tracks, while at the GeV scale momentum measurements are done with a relative resolution of approximately 30%. Precision tracking measurements are done in the barrel region using Muon Drift Tube chambers (MDT) while for the end-cap regions a combination of MDTs along with Cathode Strip Chambers (CSC) is used, arranged in wheels in front and behind the end-cap toroid magnets. For the trigger Resistive Plate Chambers (RPC) are used in the barrel region and wheels of Thin Gap Chambers (TGC) in the end-cap regions respectively. Table 3.3 lists the most important characteristics of the four chamber technologies the MS utilises, while Figure 3.12 shows a 3-D view of the MS.

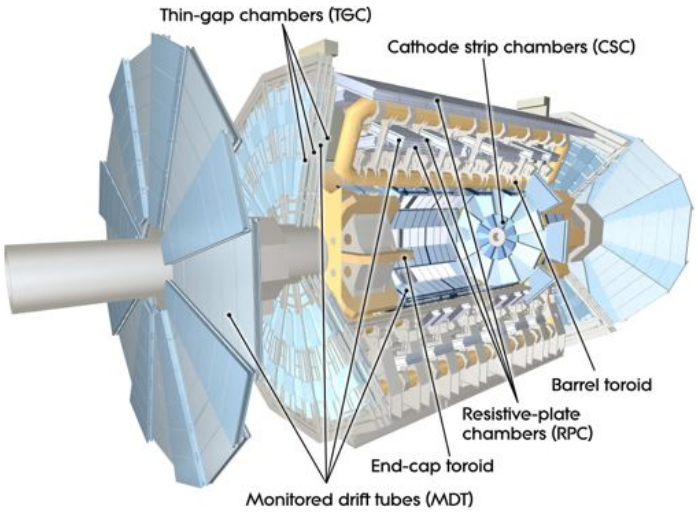

Figure 3.12: A cut-away three-dimensional view of the MS.

Muon Drift Tubes

The basic element of an MDT chamber is an 30 mm diameter aluminum tube, filled with a gas mixture of Ar (93%) and CO_2 (7%) at 3 bar pressure. The tube wall is the cathode while the anode is a tungsten-rhenium wire at the centre of the tube, with an electric field of 3080 V. A chamber consists of two multi-layers with three layers of

MS chambers parameters		
MDT	-Coverage	$\|\eta\|$ <2.7
	-Chambers	1150
	-Channels	354 k
	-Role	Tracking
CSC	-Coverage	2.0< $\|\eta\|$ <2.7
	-Chambers	32
	-Channels	31 k
	-Role	Tracking
RPC	-Coverage	$\|\eta\|$ <1.05
	-Chambers	606
	-Channels	373 k
	-Role	Triggering, 2nd coordinate
TGC	-Coverage	1.05< $\|\eta\|$ <2.4
	-Chambers	3518
	-Channels	318 k
	-Role	Triggering, 2nd coordinate

Table 3.3: The main parameters of the four technologies chambers used for tracking and triggering in the MS.

drift tubes each[8], separated by aluminum bars and frames. The structure of a MDT is shown in Figure 3.13 and the relative position and potential mechanical deformation due to gravitational sag are controlled by a dedicated monitoring alignment system, namely RASNIK [5]. Figure 3.14 shows the arrangement of the chambers in the perpendicular to the beam axis and the bending plane respectively.

The passage of charged particles through the tube causes ionisation of the gas mixture and, under the electric field, free electrons move towards the wire while ions move towards the tube walls. The electronics of the chamber translate the drift time to an electric signal that is counted. A known function, relating the drift time of a free electron to the distance it travelled, permits the translation of the electronic signal to a tracking precision measurement, via the space-drift time (r-t) relation. MDTs have an average resolution of 80 μm per tube and 35 μm per chamber.

[8]Depending on the distance from the IP, each multi-layer can consist of up to four layers.

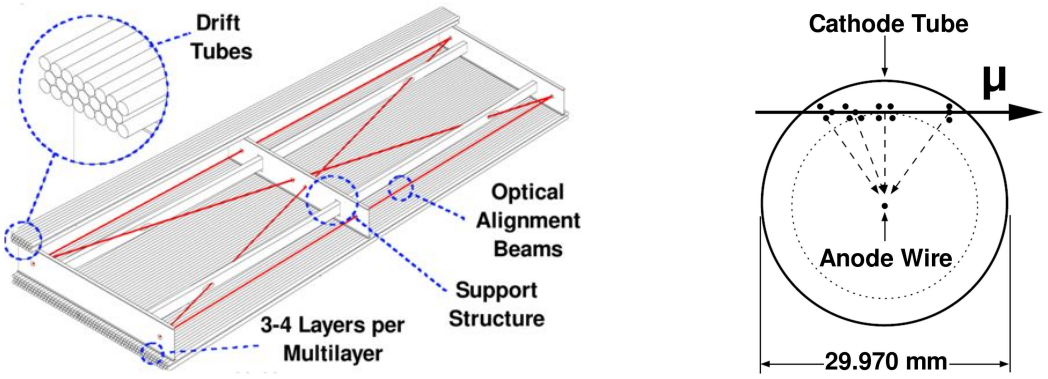

Figure 3.13: Sketch of the mechanical structure of a MDT chamber (left). Cross section of an aluminum tube (right).

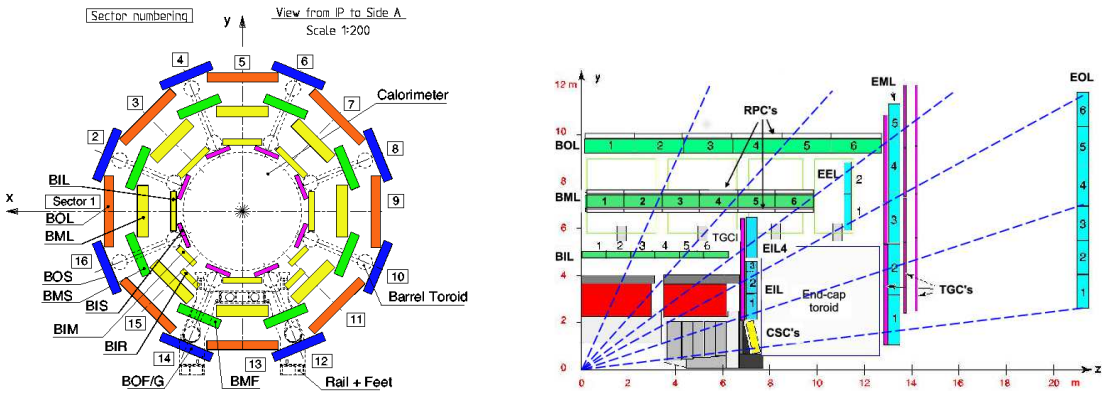

Figure 3.14: Cross-section of the barrel MS perpendicular to the beam axis, showing three concentric layers of eight large and eight small chambers. The dashed lines show the eight coils of the air-core barrel toroid magnet system (left). Cross-section of the MS in the bending plane. Infinite-momentum muons would propagate along straight trajectories which are illustrated by the dashed lines and typically traverse three muon stations.

Cathode Strip Chambers

CSCs replace MDTs at the $|\eta|$ >2.0 region to compensate for the very high rates (up to 1000 Hz/cm^2). They are multi-wire proportional chambers with their wires oriented in the radial direction, filled with a gas mixture comprising of Ar (80%) and CO_2 (20%). CSCs are placed in two disks of eight chambers each (eight small and eight large), providing independent measurements in η and ϕ along each track. The resolution in the bending plane is about 60 μm and in the transverse plane 5 mm. Figure 3.15 shows the structure of a CSC. The cathode planes are segmented into strips in orthogonal directions; the plane with the strips perpendicular to the wires provides the precision coordinate while the plane parallel

to the wires provides the transverse coordinate.

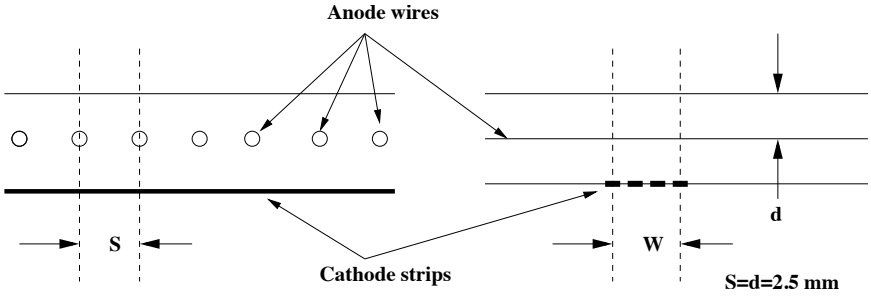

Figure 3.15: Mechanical structure of a CSC chamber. The wire pitch is equal to the anode-cathode spacing.

Resistive Plate Chambers

RPCs are used along with MDTs in the barrel region and provide triggering and two coordinate measurement. Arranged in three cylindrical layers from the IP, they consist of two resistive electrode-plates of phenolic-melaminic plastic laminate, separated by insulating spacers that form a gap filled with a gaseous mixture of $C_2H_2F_4$. Their electric field is at the order of 4.9 kV/mm and their time and space resolution is 2 ns and 1 cm respectively. Figure 3.16 shows the schematic view of a RPC.

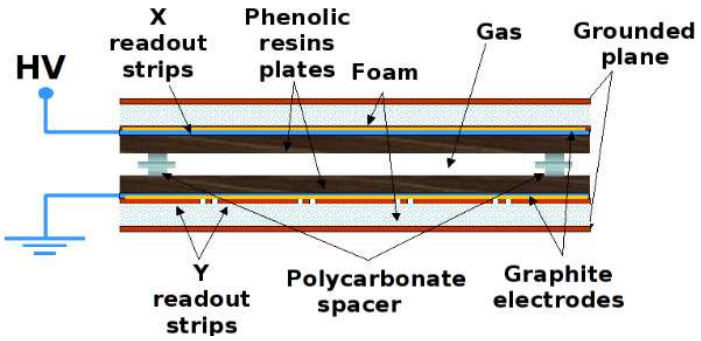

Figure 3.16: Schematics of a RPC chamber.

Thin Gap Chambers

TGCs are multi-wire proportional chambers consisting of two cathode plates at a 2.8 mm distance that are filled with a gas mixture $n-C_5H_{12}$ and CO_2. They provide a very good time resolution for the vast majority of the tracks, allowing for their signals to arrive

(with a 99% probability) within 25 ns, which makes them a reliable solution for triggering in the pseudorapidity region of 1.05< $|\eta|$ <1.92. Their resolution in R varies from 2-6 mm and in ϕ from 3-7 mm. Figure 3.17 shows the schematics of a TGC.

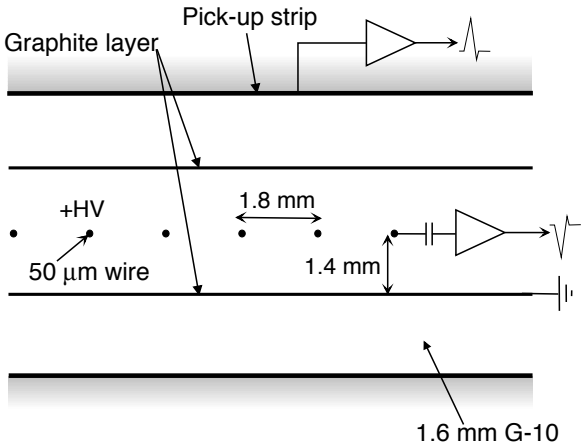

Figure 3.17: Mechanical structure of a TGC chamber. The distance between the wires is larger than the distance between the wire and the cathode.

3.3 Trigger and Data Acquisition

The Trigger and Data Acquisition (TDAQ) system of the ATLAS experiment comprises of those systems responsible for selecting events of interest, as well as the ones that handle the output of the approximately 100 M electronic channels. The LHC bunch spacing is 25 ns; therefore the anticipated rate of interactions is approximately 1 GHz (if we consider 25 interactions per bunch crossing on average for a luminosity of $10^{34}[cm^{-2}s^{-1}]$) and since each event registers no less than 1.3 MB it is evident that not all of these collisions can be recorded for further analysis. The trigger system of the ATLAS experiment is responsible for keeping the rate at tolerable levels (at most 200 Hz), selecting only events of interest based on criteria like high-p_{T} leptons and jets, as well as large E_T^{miss}. In Figure 3.18 an overview of the ATLAS trigger is presented.

The trigger system comprises of Level-1 (L1), Level-2 (L2) and the Event Filter (EF), where L2 and EF are collectively known as High-Level Trigger (HLT). L2 and EF refine the decisions made at the previous level and, if necessary, apply additional criteria. L1 is hardware based, comprising of dedicated electronics and it uses reduced information from the MS and the CS in order to feed the Central Trigger Processor (CTP) which holds

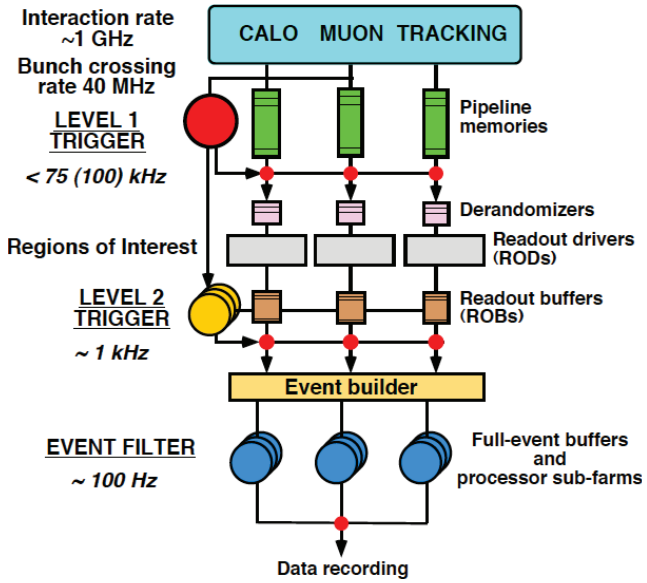

Figure 3.18: An overview of the ATLAS trigger system. Event rate is reduced from the order of GHz to 100-200 Hz after the Event Filter.

the "trigger menu", i.e. all the desired combinations of items to trigger upon. The L1 trigger maps the MS and CS sub-detectors into Regions-of-Interest (RoI's) which are the η and ϕ coordinates of the region of the subsystem with activity of interest. The rate after L1 decisions is reduced to 75 kHz in 2.5 μs in each event. L2 in turn is seeded by L1 information, starting from the RoI and using the full detector data furthermore reduces the rate to at most 3.5 kHz in an average time of 40 μs. Finally, events passing the L2 decisions go through the Event Builder (EB) that uses all the data from the Read-Out Buffers (ROB's) and submits them to the EF that runs sophisticated offline algorithms in an average time of 4 s. Figure 3.19 shows a flow chart of the L1 trigger.

The Data Acquisition system (DAQ) is made from all the subsystems responsible for data collection, formatting and processing before their final storage at the CERN computing centre, along with the ones providing the configuration, control and monitoring of all the hardware and software components which together provide the data-taking functionality. The Detector Control System (DCS) permits the coherent and safe operation of the ATLAS detector hardware and serves as a homogeneous interface to all sub-detectors and technical infrastructure. Within its role are the continuous monitoring, control and archiving of all operational parameters and signals, allowing for a series of automatic or manual corrective actions to be taken regarding high- and low-voltage systems for detec-

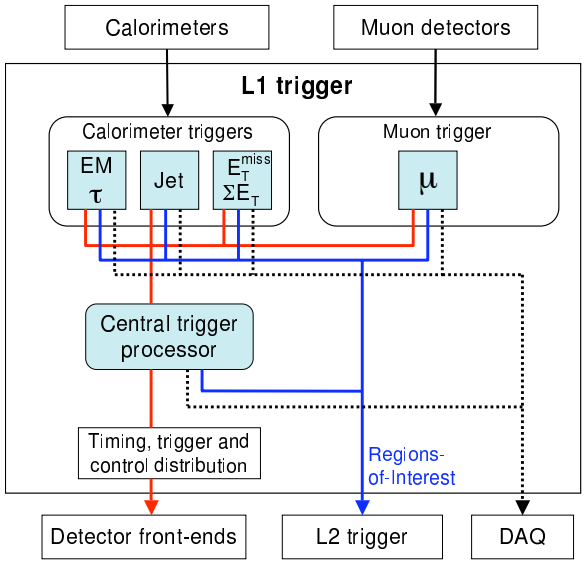

Figure 3.19: L1 trigger flow chart. All trigger decisions start with RoI's defined by L1 and are made by the CTP. Paths to the detector front-ends, L2 and DAQ are shown in red, blue and black respectively.

tors and electronics, gas and cooling systems, magnetic field, temperatures and humidity. The DCS also enables bi-directional communication with DAQ, allowing synchronisation of the detector state with the data-taking procedure and thus ensuring good data quality for Physics analyses.

Bibliography

[1] CERN, *ATLAS: Detector and physics performance technical design report, Volume 1*,.

[2] CERN, *ATLAS: Detector and physics performance technical design report, Volume 2*,.

[3] ATLAS Collaboration, G. Aad et al., *The ATLAS Experiment at the CERN Large Hadron Collider*, JINST **3** (2008) S08003.

[4] ATLAS Collaboration, *ATLAS Insertable B-Layer Technical Design Report*,. https://cds.cern.ch/record/1291633.

[5] ATLAS Collaboration, *ATLAS Muon Spectrometer Technical Design Report*,. https://cds.cern.ch/record/331068.

Chapter 4

Software

4.1 Athena framework

The Athena framework [1, 2] is an enhanced version of the Gaudi framework [3] which was originally developed for the LHCb experiment but now is a common ATLAS-LHCb project. Both Athena and Gaudi are concrete realisations of a component-based architecture, designed for a wide range of experimental physics applications. The fact that it is component-based allows flexibility in developing, both shared as well as task-specific components. The main design principles of the Athena framework include, among others:

- The use of abstract interfaces, allowing easy manipulation of groups of components that share a common interface.
- Extensive use of dynamic libraries and loading implementing the Gaudi component architecture.
- The recognition that different types of data have different lifetimes within the software. For instance data that are directly associated to a pp collision event would live at the scope of the event, while ATLAS geometry data or statistical data like histograms would be stable among many events, thus being long-lived.
- Clear separation in the framework between data and algorithms and also between data in memory (transient) and on disk (permanent).
- Multiple developer types, translating to exposure to a few, simple interfaces for the end user, providing isolation from the expert's part of the code.

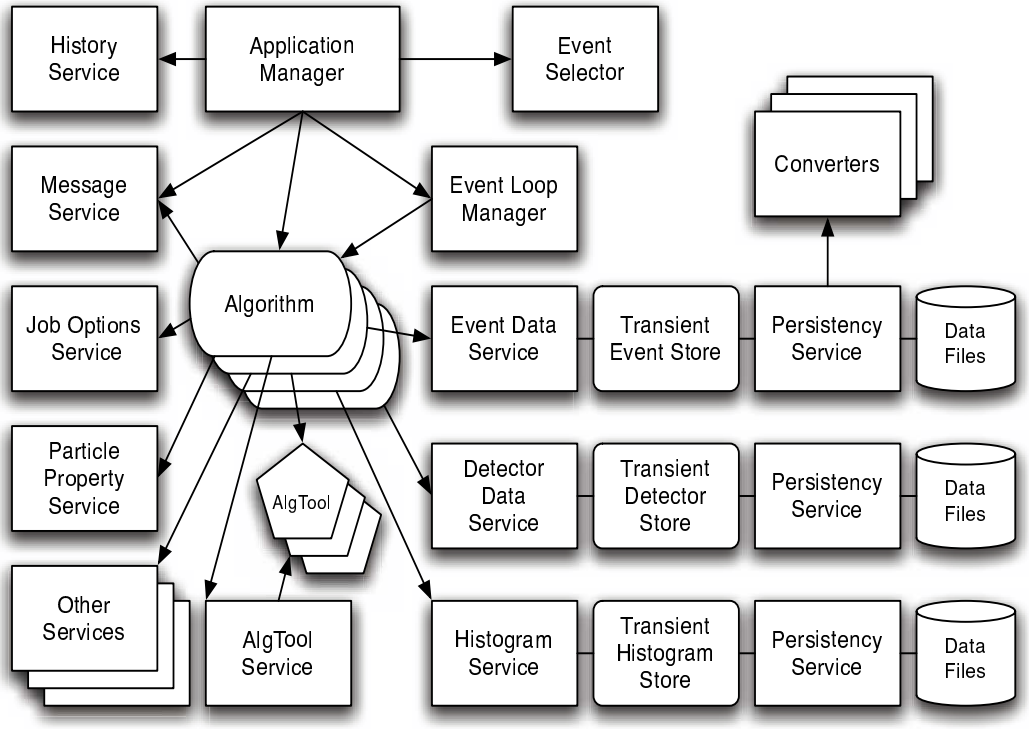

Figure 4.1: Athena framework component model.

Figure 4.1 shows the major components of the Athena framework, which are:

- **Application Manager**. The common component to all applications that manages and coordinates the activity of all other components within the application.

- **Algorithms**. Algorithms share a common interface and perform a defined (but configurable) operation on input data, usually producing some output data.

- **Sequencers**. A sequencer is a sequence of Algorithms allowing a tree structure of processing elements.

- **Tools**. Similar to Algorithms, can be executed many times within the same event. They do not share a common interface and each instance of a Tool is owned by an Algorithm, a Service or by default by the Algorithm Tool Service (AlgToolSvc).

- **Services**. They provide high-level functionality needed by Algorithms, such as message printing, data access, persistency operations, e.t.c.

- **Selectors**. These components perform selections, i.e the Event Selector that provides functionality to the Application Manager for selecting the input events to be processed.

- **Converters**. Responsible for conversion of data from one representation to another and also from transient to persistent form.

- **Properties**. All the adjustable elements of a component defined by basic (integer, float, e.t.c.) or user-defined variable types.

Within the purposes of the Athena framework are a large number of duties; from high-level triggering to event generation and reconstruction, Athena is the heart of the ATLAS software. Apart from its role in raw-data formatting, Athena is used for producing Monte Carlo (MC) events, that have the exact same format with the data and are crucial in all Physics as well as performance analyses and studies. The simulated events are produced within the following steps:

Event generation

In the event generation step pp collisions are simulated for a process of interest, for instance $pp \rightarrow WZ \rightarrow \mu ee$. This is done using dedicated software, namely generators like Pythia [4], Sherpa [5] and Madgraph [6] (among others). These take as input Parton Distribution Functions (PDF), re-normalisation and factorisation scales and configurable initial- and final-state kinematics in order to produce the final-state particles from the hard scattering as well as the remnants of the pp collision. Generators also take care of the parton-showering and hadronisation processes and all the information of the generated particles is kept in the HepMC format [7], within the *mc_truth* container.

Simulation

During this step all particles produced by the generator are fed to Geant [8, 9], the dedicated software for detector simulation. Geant simulates the passage of particles through the ATLAS detector and their interactions with the active material under its magnetic field. This process creates the so-called "hits", the information blocks containing the energy loss and the position of the particles which is added to the *mc_truth* record. Figure 4.2 shows the flow of the ATLAS simulation software.

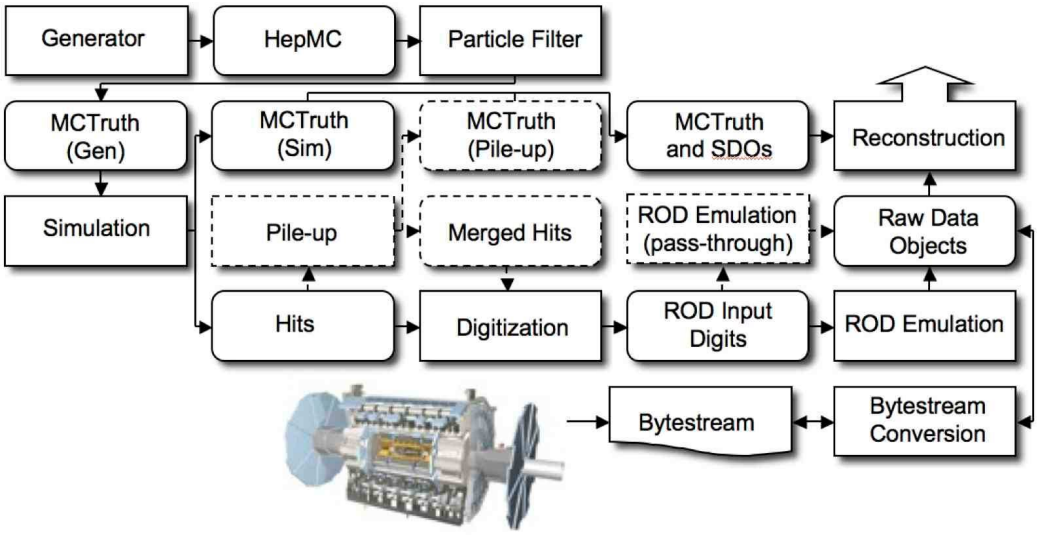

Figure 4.2: The flow of the ATLAS simulation software, from event generators (top left) through reconstruction (top right). Algorithms are placed in square-covered boxes and persistent data objects are placed in round boxes.

Digitisation

In the digitisation step the hits produced from Simulation are used in order to emulate the detector electronics response. During this process the intrinsic resolution of each sub-detector is taken into account and the output of this step, namely Simulated Data Objects (SDOs) or "digits" are introduced to the Read-Out Drivers (RODs) in order to produce the Raw Data Object (RDO) files. RDO files from MC generated events are identical to data events and the final step that follows is common to both.

Reconstruction

Reconstruction is the final step of the Athena framework in the full chain. In this step high-level objects, suitable for Physics analyses, like vertices, leptons, jets and calorimeter energy deposits are built from low-level objects (digits). This is done by a series of reconstruction algorithms that utilize energy measurements, fitting techniques and pattern recognition. The final output is a collection of containers with all the physics objects at the detector level, suitable for validation and performance, namely the Event Summary Data (ESD) format.

4.2 Event model

In the ATLAS Event Data Model (EDM) the representation of detector elements and/or objects (particles, jets) is completely object-oriented, adopting the POOL/ROOT [10–12] format. There are many event representations within the ATLAS analysis model; The output of the HLT algorithms is the RDO format where reconstruction runs upon it; ESD is the output of the reconstruction step and from that point on, a series of formats is available, depending on the analysis. The Analysis Object Data (AOD) is a reduced event representation, derived from ESD and it contains the full information for high-level Physics objects and reduced information for low-level detector objects. The Derived Physics Data (DPD) format is a format suitable for a specific Physics or performance group, since it contains only the subset of interest of the full information stored in the ESD or AOD formats. DPDs can be produced from ESDs (dESD) or AODs (dAOD) or, as an alternative, directly from an Athena analysis job, resulting in the D3PD format, suitable for ROOT analysis since it contains flat n-tuples and/or histograms. During D3PD production stricter event selection criteria may be applied (skimming), variables of no interest may be removed (thinning) and the information per object may be reduced (slimming). Table 4.1 summarises the main data formats used in the ATLAS experiment.

4.3 Grid

The volume of data produced per year in the ATLAS experiment is at the order of several PB, widowing their storage and manipulation a challenging task. A traditional approach would be to centralize the required sources at one location near the experiments. However, CERN pioneered in developing a distributed analysis technology for the LHC experiments, namely the Worldwide LHC Computing Grid (WLCG), or more simple the Grid, which provides several key benefits, the major ones being:

- The significant costs of maintaining and upgrading the necessary resources for such a computing challenge are more easily handled in a distributed environment, where individual institutes and participating national organisations can fund local computing resources, while still contributing to the global goal.
- In a distributed system there are no single points of failure. Multiple copies of data and automatic reassigning of computational tasks to available resources ensures load

Format	**Size** (at HLT rate of 200 Hz)	**Description**
RDO	1.6 MB/event	The output of the EF. Events arrive in "byte-stream" format, as delivered from the detector, to be used for reconstruction.
ESD	0.5 MB/event	The full collection of high-level objects, suitable for Physics analyses. All low-level detector information and high-level Physics objects containers are present.
AOD	0.1 MB/event	This format contains the high-level Physics objects containers and part of the detector-related objects. Strictly object-oriented, stored in POOL/ROOT format
D3PD	10 KB/event	The lightest format of all, suitable for performance groups or specific Physics analyses.

Table 4.1: Main data formats within the ATLAS experiment. The POOL/ROOT output format is the common format chosen for all data types.

balancing. Spanning all time zones also facilitates round-the-clock monitoring and support.

The Grid addresses the aforementioned challenges with a tiered computing model [13,14], with Tier-0 being the CERN facilities, where the first processing of data is performed and a replica is kept. Tier-0, through the backbone infrastructure of dedicated $GBit$ lines, shares the data with major research and computing centres throughout the world, the Tier-1 facilities. Their responsibilities include storage of data replicas, reprocessing of data, production of desired data formats and redistribution to Tier-2 facilities worldwide, for Physics analyses. Tier-2 centres also serve as MC production and storage facilities, along with their end-user analysis role. Figure 4.3 shows the tiered structure of WLCG.

The second key component of the Grid, apart from the backbone infrastructure of dedicated $GBit$ lines, is the middleware, the part of the software that rests between the

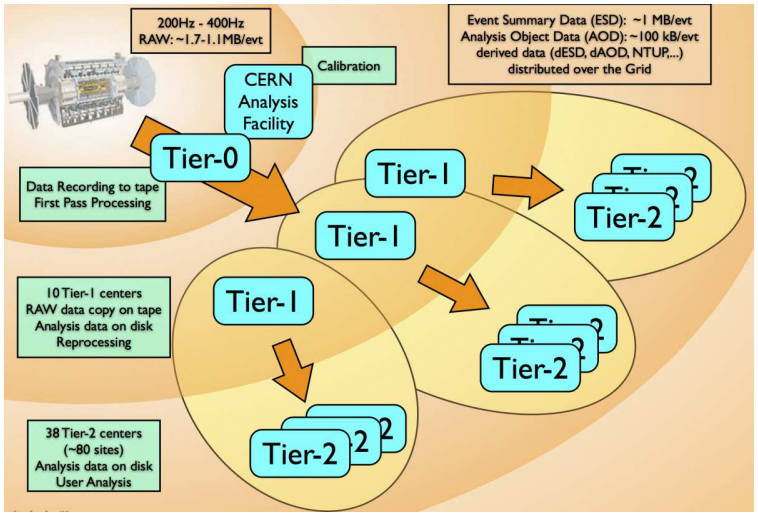

Figure 4.3: The tiered structure of the ATLAS Grid. Tier-0 is CERN where the first processing of RAW data takes place. Distribution to Tier-1 centres for further processing and production of various formats is done via dedicated lines.

operational systems and the end-user applications. Middleware comprises of the specialized software projects, used for a series of tasks such as managing data distribution and access, job submission and user authentication and authorisation and it includes *Globus*, *Virtual Data Toolkit* and *gLite* among others. Within the context of the ATLAS experiment, a set of wrappers has been developed, utilizing the capabilities of the middleware and providing an abstract layer to the end-user, for all Grid-related activities. These include:

- **AMI**. ATLAS Metadata Interface contains all the essential info and commands for various dataset(s) operations..
- **DQ2**. Don Quixote 2: a tool for producing output datasets, registering them on the Grid and downloading for local jobs.
- **PanDA**. PanDA allows for a series of tasks related to distributed analysis operations, from submission to monitoring tools.

Bibliography

[1] ATLAS Collaboration, G. Duckeck et al., *ATLAS computing: Technical design report*,.

[2] *The Athena Software*,. http://atlas-computing.web.cern.ch/atlas-computing/packages/athenaCore/athenaCore.php.

[3] G. Barrand, I. Belyaev, P. Binko, M. Cattaneo, R. Chytracek, et al., *GAUDI - A software architecture and framework for building HEP data processing applications*, Comput.Phys.Commun. **140** (2001) 45–55.

[4] T. Sjostrand, S. Mrenna, and P. Z. Skands, *PYTHIA 6.4 Physics and Manual*, JHEP **0605** (2006) 026, arXiv:hep-ph/0603175 [hep-ph].

[5] T. Gleisberg, S. Hoeche, F. Krauss, M. Schonherr, S. Schumann, et al., *Event generation with SHERPA 1.1*, JHEP **0902** (2009) 007, arXiv:0811.4622 [hep-ph].

[6] J. Alwall, P. Demin, S. de Visscher, R. Frederix, M. Herquet, et al., *MadGraph/MadEvent v4: The New Web Generation*, JHEP **0709** (2007) 028, arXiv:0706.2334 [hep-ph].

[7] M. Dobbs and J. B. Hansen, *The HepMC C++ Monte Carlo event record for High Energy Physics*, Comput.Phys.Commun. **134** (2001) 41–46.

[8] J. e. a. Allison, *Geant4 developments and applications*, Nuclear Science **53** (2006) 270–278.

[9] *Geant4, a toolkit for the simulation of the passage of particles through matter*,. http://geant4.web.cern.ch/geant4/.

[10] *POOL: Pool Of persistent Objects for LHC*,. http://pool.cern.ch/.

[11] R. Brun and F. Rademakers, *ROOT - An Object Oriented Data Analysis Framework*, Nucl. Inst. and Meth. in Phys. **A 389** (1997) 81–86.

[12] *ROOT - A Data Analysis Framework*,. http://root.cern.ch/drupal/.

[13] C. Eck, J. Knobloch, L. Robertson, I. Bird, K. Bos, N. Brook, D. Düllmann, I. Fisk, D. Foster, B. Gibbard, C. Grandi, F. Grey, J. Harvey, A. Heiss, F. Hemmer, S. Jarp, R. Jones, D. Kelsey, M. Lamanna, H. Marten, P. Mato-Vila, F. Ould-Saada, B. Panzer-Steindel, L. Perini, Y. Schutz, U. Schwickerath, J. Shiers, and T. Wenaus, *LHC computing Grid: Technical Design Report. Version 1.06 (20 Jun 2005).* Technical Design Report LCG. CERN, Geneva, 2005.

[14] *ATLAS Collaboration, P. Nilsson, Distributed Data Analysis in ATLAS, ATL-SOFT-PROC-2009-007 (2009)*,.

Chapter 5

Reconstruction

Physics analyses, in HEP experiments, are realised using final state objects such as leptons, jets and vertices along with information regarding the missing transverse energy of the event. In particular, stable objects like electrons and muons[1] are relevant in this analysis where the final state is comprised by three leptons accompanied by significant E_T^{miss}. In this chapter a description of how these objects are identified and registered for analysis purposes, through the process called reconstruction, will be given; mainly for leptons and briefly for jets, since the latter are also used in the calculation of E_T^{miss}.

5.1 Electrons

An electron in the ATLAS experiment is defined by a shower in the EC, which is (usually) associated to a track in the ID. Depending on the kinematic properties (p_{T} and η), there are three algorithms for electron reconstruction, with their details available in [1–3].

1. In the first (standard) algorithm areas in the EC are investigated and a candidate is matched to an ID track. An energy deposit in the EC is the starting point for the reconstruction, where an algorithm (namely *sliding window*) sums up neighbouring calorimeter cells within a region of $\Delta\eta$ x $\Delta\phi = 0.075$ x 0.125 and defines the cluster position so that the energy inside the η x ϕ window is a local maximum, constructing

[1] A muon can be considered as being stable, within the context of the ATLAS detector, since it can travel through the whole detector before it decays. Under the assumption that muons travel approximately with $v \simeq c$ and given their lifetime $t_\mu = 2.2 \cdot 10^{-6}$ s we get for their flight length $s = v \cdot t \simeq 658$ m, which is well above any ATLAS detector dimension.

this way a seed cluster. ID tracks satisfying track-quality criteria (such as silicon hits) are then extrapolated to the middle layer of the EC (using either their momentum or the cluster energy scale) and if they are within $\Delta\phi = 0.1$ from the cluster[2], an electron candidate is found. In the case where no ID track can be successfully matched, the seed cluster is classified as photon.

2. The second algorithm follows the opposite approach, where the starting point is an ID track that is extrapolated to the EC, where a cluster is formed using as seed the track impact point. This algorithm is used for low-p_{T} electrons.

3. Finally the third algorithm reconstructs electrons in the forward region where no ID information is available and therefore no track matching between an ID track and the EC cluster is performed.

Since a jet can mimic an electron, identification criteria are required in order to ensure low electron fake rates. These are based on cuts on the shower shapes in the CS, information on the reconstructed tracks and from combined reconstruction. Depending on the signal efficiency and jet rejection requirements of the Physics samples under study, the following cut-based operating (working) points, optimised in p_{T} and η have been defined for electron identification:

- **loose++:** Simple shower-shape cuts, like longitudinal leakage and shower shape in the middle layer of the EC, are used in order to match the reconstructed track with the calorimeter cluster. They are based on the fact that the energy deposit by electrons in the EC is different than the one by jets, while it is also expected the width of the showers to be narrower in η for electrons than for jets;

- **medium++:** Shower-shape cuts including also information from the first calorimeter layer, along with track-quality cuts;

- **tight++:** Track-matching criteria applied are tightened as well as the cut applied on the energy-to-momentum ratio. Further isolation criteria are imposed.

- **multilepton:** Optimised selection operating point, for low energy electrons in the $H \rightarrow ZZ^{(*)} \rightarrow 4l$ analysis, with a similar efficiency to the *loose++* but a better

[2]Actually the matching is done using the metric of the space: $\Delta R = \sqrt{\Delta\eta^2 + \Delta\phi^2}$ with $\Delta\eta = 0.05$ and $\Delta\phi = 0.1$. It is evident that the $\Delta\phi$ separation is crucial, given these values.

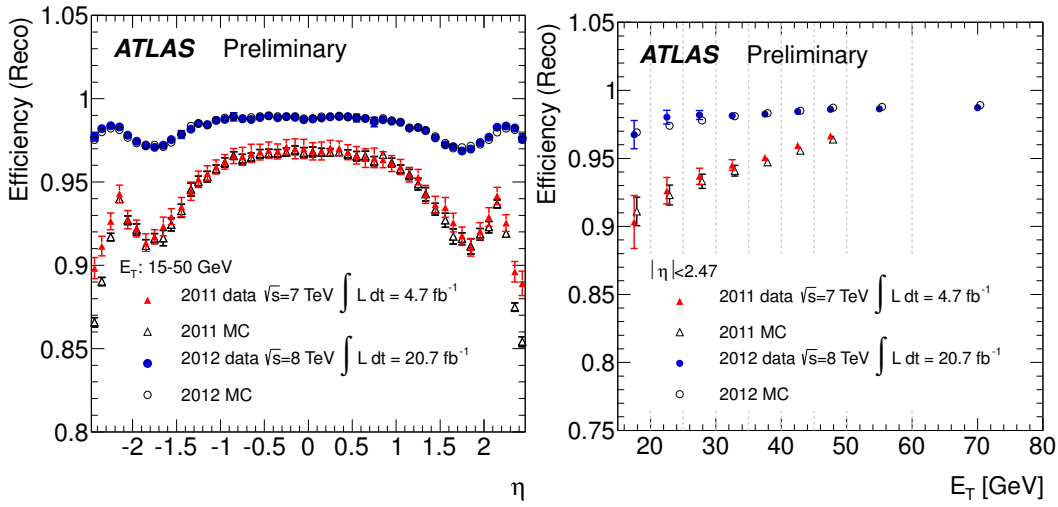

Figure 5.1: Measured electron reconstruction efficiency as a function of η for 15GeV< E_T <50GeV (left) and E_T integrated over the full pseudorapidity range (right).

background rejection factor, containing on top of the *loose++* selection cuts variables measuring bremsstrahlung effects.

Apart from the above set of cuts, a different approach has been implemented as well in the 2012 data menu, the so-called *likelihood* identification menu. It is a multi-variant technique that allows for the combined evaluation of several properties when making a selection decision, making use of signal and background probability density functions (PDFs) of the discriminating variables. Based on these PDFs, an overall probability is calculated, with the PDFs being obtained from data and the selections defined as *looseLH*, *mediumLH* and *tightLH* selected to match the efficiency as in *Multilepton*, *medium++* and *tight++* respectively.

Reconstruction efficiency

The reconstruction efficiency for electrons are derived using events from $Z \rightarrow ee$ decays collected in data and using the tag-and-probe method. Figure 5.1 shows the relevant efficiency as a function of η and E_{T}.

Identification efficiency

Electron identification efficiency are calculated using the tag-and-probe method with events from $Z \rightarrow ee$, $W \rightarrow e\nu$, and $J/\psi \rightarrow ee$ decays collected in data [3]. Figure 5.2

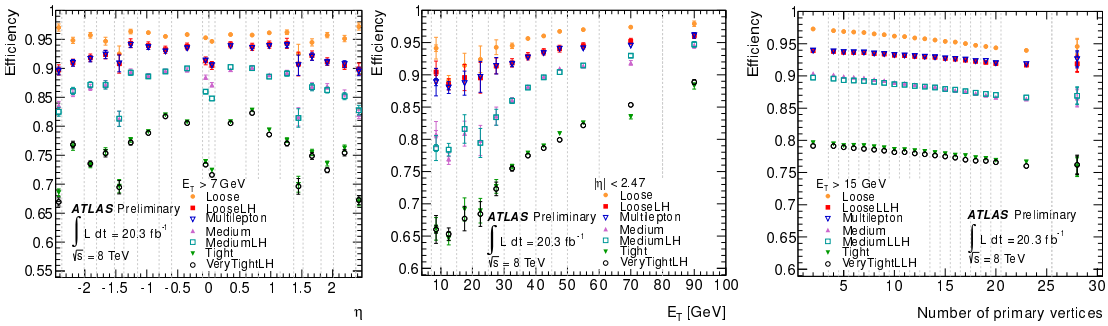

Figure 5.2: Electron identification efficiency calculated using $Z \to ee$, $W \to e\nu$, and $J/\psi \to ee$ decays from data events as a function of η (left), E_{T} (middle) and number of reconstructed vertices (right). The uncertainties displayed include both statistical and systematic, while a comparison with MC expectation is shown (black).

shows the efficiency calculated with the full 2012 dataset, as a function of η, E_{T} and the number of reconstructed primary vertices.

Energy scale

In order to calibrate the energy scale of electrons in the EC and establish it's linearity in response, test-beam measurements are used along with events from $Z \to ee$, $W \to e\nu$, and $J/\psi \to ee$ decays collected in data [3]. In the context of this procedure, the dominant uncertainty in the electron energy scale determination emerges.

5.2 Muons

ATLAS implemented a muon spectrometer capable of precise muons momenta measurements in the p_{T} range from as low as 3 GeV, up to the TeV scale. Muons loose very little of their energies when traversing the inner detector and the calorimeter systems, even though they travel as far as 100 radiation lengths of material. Their identification is done by the MS up to the range of $|\eta|$ <2.7. For their reconstruction, two independent algorithms are employed, `MOORE` [4] and `Muonboy` [5] that both use the same approach. Starting from the drift-radius measurements, a track segment within a chamber is given by a straight line fit[3], by performing all the combinatorics emerging from the number of hits and selecting the best χ^2/NDF candidate. Segments from all the stations are then

[3]The straight line fit is a valid approach taking into account the p_{T} of a muon and the length of a chamber.

combined, under the consideration of the magnetic field, to form the full muon track in the MS. For the p_{T} measurement, a *super-point* is defined between the multi-layers of each chamber participating in the reconstruction of a track. By combining the three super-points the sagitta of the track can be defined from which the p_{T} measurement is done. Figure 5.3 shows a sketch of a segment formation along with the combination of segments into a single track.

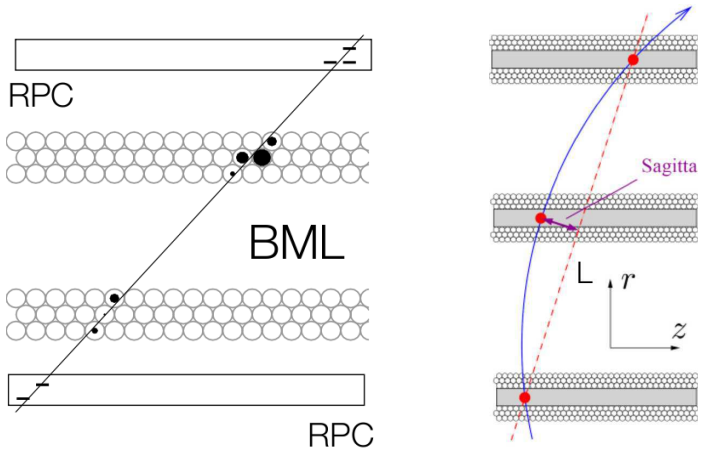

Figure 5.3: Muon segment formation, from drift-radius measurements in the two multi-layers of an MDT chamber (left). Full muon track reconstruction using chambers in all three MS stations. The p_{T} is measured from the sagitta of the three super-points (red points) of the resulting track (right).

Even though muons pass through the CS without significant loss of energy (except for the rare so-called *catastrophic* losses, where a muon deposits a large fraction of it's energy [6]), their behaviour is consistent with that of a minimum ionizing particle. Furthermore, since muons are charged particles, the full capabilities of the ID can be exploited, along with information from the CS in the process of the reconstruction. Therefore, four muon families can be defined, according to the information used:

1. **Combined (CB):** In the common acceptance of the ID and the MS ($|\eta|$ <2.5) muon tracks reconstructed by the MS can be combined with tracks in the ID, using either a global refit (`MOORE`) or a statistical combination (`Muonboy`) method. This results in improved momentum resolution and lower fake rates than in any other reconstructed muon family.

2. **Stand-alone (SA):** Stand-alone muons are reconstructed solely in the MS, without

using any information from the ID. Muon tracks are extrapolated to their vertex of origin, taking into account information from the CS to correct for energy losses. Stand-alone muons extend muon identification outside the ID span, up to $|\eta|$ =2.7.

3. **Segment-tagged (ST):** Segment-tagged muons are formed by combining ID tracks to partially reconstructed muons[4] by the MS (usually the inner station), taking into account information from the CS. Their parameters are those calculated by the ID and the segments used to form muons of this family have not been used in the track reconstruction of CB muons.

4. **Calorimetric-tagged (CT):** This family of reconstructed muons is useful for muons near the vicinity of $|\eta| \simeq 0$, where there is no MS coverage. CT muons are reconstructed using ID tracks along with CS info (shower shapes compatible with minimum ionizing particles) and the track parameters of the ID track, like in the ST case, are used. However, CS muons suffer from high fake rates.

In this analysis, CB along with ST muons are used. Figure 5.4 shows a sketch of the detector subsystems relevant in the reconstruction process for each of the four muon families.

Reconstruction efficiency

Similarly to electron efficiency, muon reconstruction efficiency are calculated as well using the tag-and-probe method with events from $Z \to \mu\mu$ and $J/\psi \to \mu\mu$ decays collected in data [7]. The latter are used in order to extract the efficiency in the low-p_{T} region, up to $\simeq$10 GeV. Figure 5.5 shows the efficiency calculated with the full 2012 dataset, as a function of η and p_{T}.

Momentum scale and resolution

The MC knowledge of the detector conditions is described with a set of constants that can differ from the actual (real) conditions. These differences can play an important role in factors affecting the muon momentum resolution, including detector misalignment, the intrinsic resolution of the muon chambers as well as multiple scattering effects. To

[4] Partial reconstruction stands for muons that did not traverse all three muon stations, either falling out of the MS acceptance, or having low-p_{T}, or falling in the transition or services reserved regions ($|\eta| \simeq$0, 1.2).

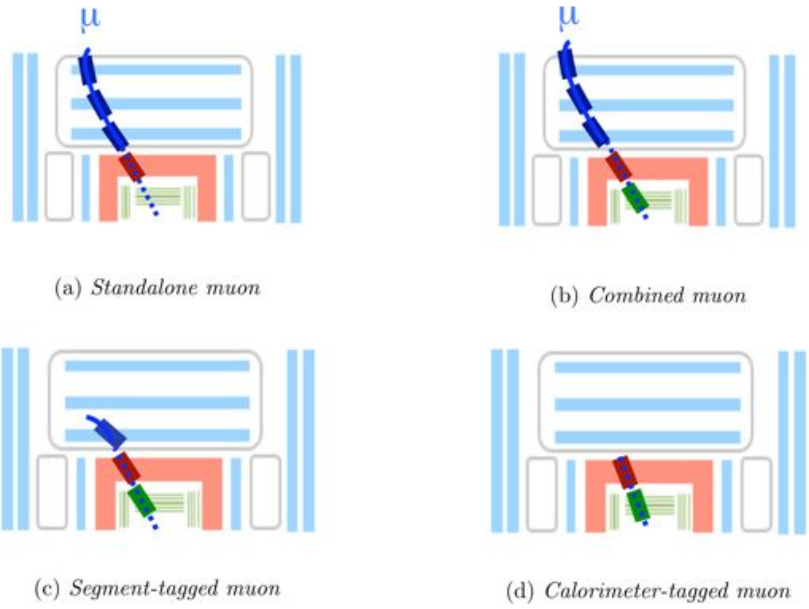

(a) *Standalone muon* (b) *Combined muon*

(c) *Segment-tagged muon* (d) *Calorimeter-tagged muon*

Figure 5.4: Reconstructed muon categories, top left SA, top right CB, bottom left ST, bottom right CT.

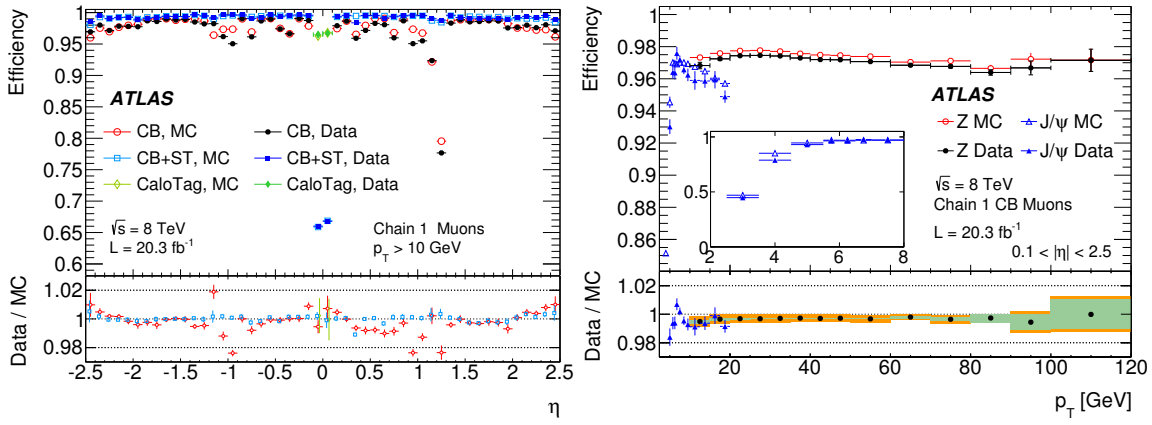

Figure 5.5: Muon efficiency calculated using $Z \to \mu\mu$ and $J/\psi \to \mu\mu$ decays from data events as a function of η (left), p_{T} (right).

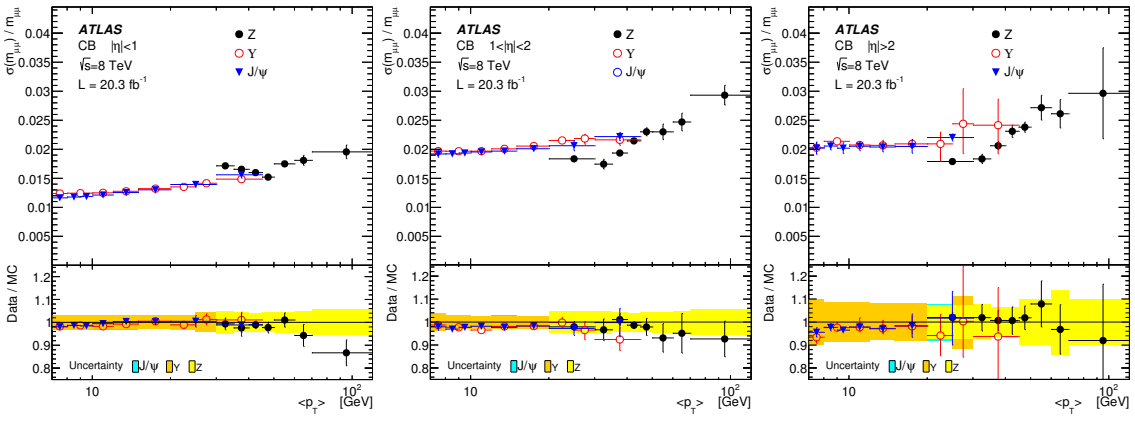

Figure 5.6: Dimuon invariant mass resolution for CB muons measured from J/ψ, Υ and Z events as a function of the average p_{T} in three η ranges, $|\eta| < 1$ (left), $1 < |\eta| < 2$ (middle) and $|\eta| > 2$ (right). The lower panel shows the ratio between data and the corrected MC. The bands represent the uncertainty on the MC correction.

account for this fact, muon p_{T} distribution is corrected (smeared) so that it matches the one obtained in data, using muons from $Z \to \mu\mu$, $J/\psi \to \mu\mu$ and $\Upsilon \to \mu\mu$ decays. The scale correction to the simulated ID track reconstruction is always below 0.1%, while for the correction to the MS scale it is at the level of 0.1%, except for the large MS sectors in the barrel region whereas a correction of 0.3% is needed, and for specific MS regions with $1.25 < |\eta| < 1.5$ where a correction of about 0.4% is necessary. Figure 5.6 shows the dimuon mass resolution, as it was obtained for CB muons.

5.3 Jets

Jets are present in many final states within the context of the LHC Physics program. In the ATLAS experiment, reconstruction of jets is done by two algorithms: a seeded fixed-cone and a successive iterative, both used in two distinct configurations that utilise different cone sizes of either $R = 0.4$, 0.7 for the seeding cone and 0.4, 0.6 for the anti-k$_\perp$ respectively, resulting in narrower or wider jets [8].

Jet finding is performed using two different signals from the calorimeters, towers and topological clusters. Towers are composed by collecting cells into bins of a $\Delta\eta$ x $\Delta\phi$ = 0.1 x 0.1 grid and yielding their total signal. In case of towers with negative signals, a recombination process is used that emulates cell noise cancellation. Topological cell clusters perform a three-dimensional reconstruction of the energy deposition in the calorimeter,

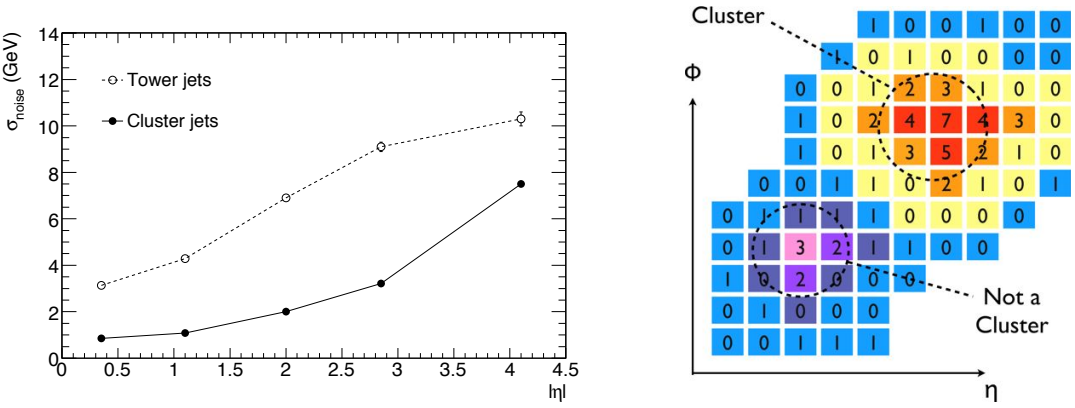

Figure 5.7: Average electronic noise contribution to cone jets with $\Delta R = 0.7$ in QCD di-jet events, reconstructed from towers (open circles) and topological cell clusters (full circles) as a function of η (left). Formation of topological cell clusters, where cells with $|E_{cell}| > 4\sigma_{noise}$ seed the cluster. Neighbouring cells with $|E_{cell}| > 2\sigma_{noise}$ are added iterative while in the final step neighbouring cells over a very low threshold are added (right).

taking as seeds cells with a significant absolute signal above the major seed threshold, i.e. $|E_{cell}| > 4\sigma_{cell}$ of the total noise (electronics plus pile-up). All neighbouring cells, using a secondary seed threshold equal to $|E_{cell}| > 2\sigma_{cell}$ are added and finally all surrounding cells that are above a very low threshold (typically set to 0 σ) are included as well, if no more secondary seeds are among the direct neighbours. In this process actual noise suppression is included, resulting in substantially less noise. Figure 5.7 shows the noise distribution as a function of η for towers and cluster jets, along with an example of how topological cell clusters are build.

5.4 Missing transverse energy

The ATLAS detector has almost 4π solid angle coverage and fair hermiticity, provided by the calorimeter systems. However, in some cases of either:

- very forward particles that fall outside the detector acceptance,
- mis-reconstructed particles,
- the presence of neutrinos,

there is an amount of missing energy in the transverse plane. This amount, denoted by E_T^{miss} (or MET), is expected to be significant for all processes including the production of

a W boson, for decays of the type $Z \to \nu\nu$ or in the case of New Physics events.

In order to calculate the E_T^{miss} of a pp event, the four-momenta of all the reconstructed physics objects, like electrons, muons, taus and jets are taken into account, by combining information from the calorimeter systems and the muon spectrometer. Especially in the calorimeters, after combining the information regarding the physics objects aforementioned, the remaining non associated cells to a physics object are summed as well contributing to the so-called *CellOut* MET term.

The calculation of MET has two major terms: a calorimeter one, calculated by adding all the energy depositions calibrated to the corresponding object and an MS term, which is calculated from all the muons falling inside the acceptance of the MS, corrected for energy losses in the calorimeter system. In the case of the $W^{\pm}Z$ analysis for the calculation of MET calibrated topological clusters are used in order to construct the calorimeter term and the flavour of E_T^{miss} used is called `MET RefFinal`.

Bibliography

[1] ATLAS Collaboration, G. Aad et al., *The ATLAS Experiment at the CERN Large Hadron Collider*, JINST **3** (2008) S08003.

[2] ATLAS Collaboration, G. Aad et al., *Expected Performance of the ATLAS Experiment - Detector, Trigger and Physics*, arXiv:0901.0512 [hep-ex].

[3] ATLAS Collaboration, *Electron efficiency measurements with the ATLAS detector using the 2012 LHC proton-proton collision data*,.

[4] D. Adams, K. A. Assamagan, M. Biglietti, G. Carlino, G. Cataldi, F. Conventi, A. Farilla, Y. Fisyak, S. Goldfarb, E. Gorini, T. Lagouri, K. Mair, L. Merola, A. Nairz, A. Poppleton, M. Primavera, S. Rosati, J. T. Shank, S. Spagnolo, L. Spogli, G. D. Stavropoulos, M. Verducci, and T. Wenaus, *Track reconstruction in the ATLAS Muon Spectrometer with MOORE 007*, Tech. Rep. ATL-SOFT-2003-007, CERN, Geneva, May, 2003. revised version number 1 submitted on 2003-10-13 13:51:39.

[5] R. Nicolaidou, L. Chevalier, S. Hassani, J. Laporte, E. Le Menedeu, and A. Ouraou, *Muon identification procedure for the ATLAS detector at the LHC using Muonboy reconstruction package and tests of its performance using cosmic rays and single beam data*, J.Phys.Conf.Ser. **219** (2010) 032052.

[6] C. Bachas, *Studies of the ATLAS Muon Spectrometer with Test Beam and Simulated Physics Data*,.

[7] ATLAS Collaboration, *Measurement of the muon reconstruction performance of the ATLAS detector using 2011 and 2012 LHC proton-proton collision data*,.

[8] G. Cacciari, S. Salam, and G. Soyez, *The anti-kt jet cluster algorithm*, JHEP04 **063** (2008).

Chapter 6

Data Quality Monitoring

The Data Quality Monitoring (DQM) is the core of the ATLAS dedicated software that ensures the quality of data. DQM is part of the Data Quality Monitoring Framework (DQMF) [1], which is the distributed system that provides DQM functionality in the online environment. The DQM constantly monitors the detector status during data-taking periods (on-line DQM) as well as the quality of the off-line reconstructed data (off-line DQM).

In the on-line environment, information about the on-going run are presented with a latency of O(s) and in an automated way to the shifter, ensuring that potential problems during data-taking periods are identified and solved on the spot. This is feasible thanks to the *on-line stream*, which is fed directly from the Data Acquisition (DAq) system during the run. During reconstruction, the off-line DQM performs more complex checks on the integrity of the reconstructed data, in order to provide extra information about the detector conditions during the run. The latency of the off-line DQM is of O(day) and with it the quality of the data is re-evaluated. The off-line DQM utilises the *express stream* which contains as low as 10% of the reconstructed data of a run.

My contribution in the DQM project was within the context of the off-line DQM for the Muon Spectrometer.

6.1 Muon off-line DQM

Off-line DQM runs along the full reconstruction of the express stream performing more complex checks on the data in order to flag the quality of the run. Four dedicated software packages, running within the context of the ATLAS software Athena, have been de-

veloped in order to serve the Muon DQM, namely the following: `MuonRawDataMonitoring`, `MuonSegmMonitoring`, `MuonTrackMonitoring` and `MuonPhysicsMonitoring`. The output of these packages is a ROOT file containing monitoring histograms that are to be checked by the off-line muon shifter. Each histogram contains the algorithm (the actual check) and its result, which is flagged following a color code where red indicates a problem, yellow a potential problem and green shows no problem. These monitoring flags are propagated upwards in order to characterise the status of a subsystem, i.e the RPCs. Following the flow of the reconstruction chain, the muon off-line DQM can be seen as operating in the following steps:

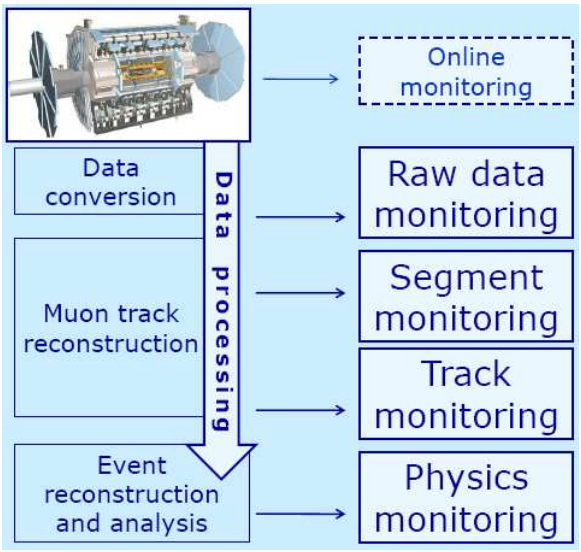

Figure 6.1: Schematic diagram of the flow of the muon off-line DQM, with respect to the data processing [2].

- **Raw data monitoring:** Hit-level quantities are monitored in order to verify the integrity of the read-out system. It is performed when the raw byte stream is converted to hit information ("low-level"). These quantities include chamber occupancies, hit multiplicities and noise levels, charge and time spectra, as well as correlations between chambers. Figure 6.2 shows some of the aforementioned quantities.

- **Segment and track monitoring:** In the "mid-level" monitoring, reconstructed quantities are used in order to check the performance of the two muon reconstruction algorithms, namely `MOORE` and `MuonBoy`. Specifically, segments (which are reconstructed within the scope of a single chamber) are of particular interest since they

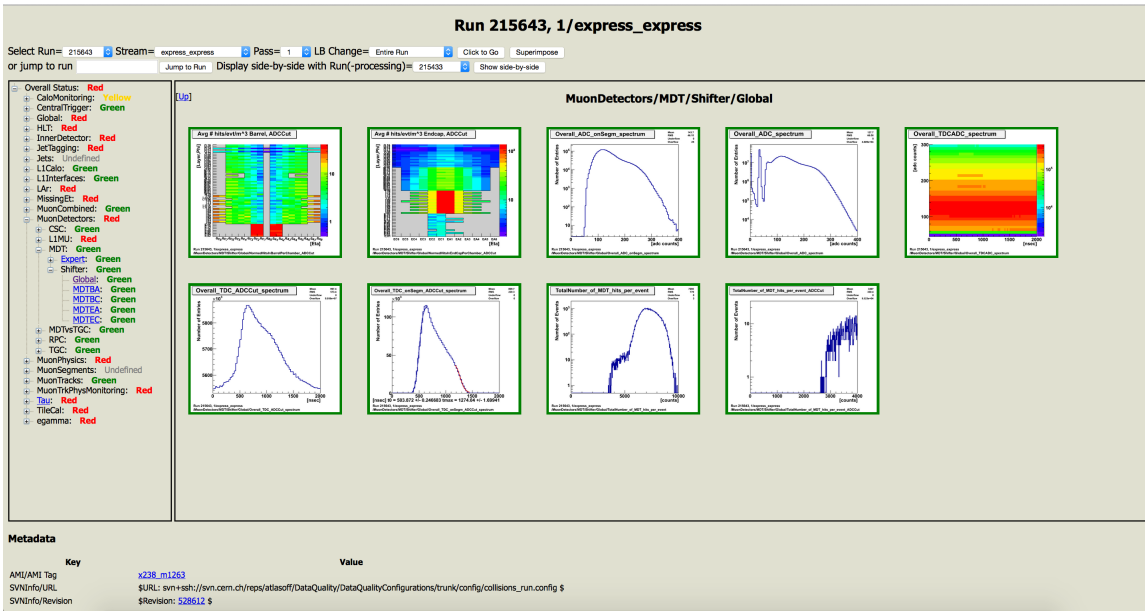

Figure 6.2: Muon DQMF web display of the Raw Data Monitoring package. Several quantities of interest are presented.

can provide information about the reconstruction efficiency of a chamber as well as the verification of the calibration constants. In the track monitoring, where segments from more than one chamber are used, the quality of the fit is checked along with track multiplicity, track p_{T} as well as spacial distributions. Figure 6.3 shows the η-ϕ map of the reconstructed segment stations along with fit quality distributions.

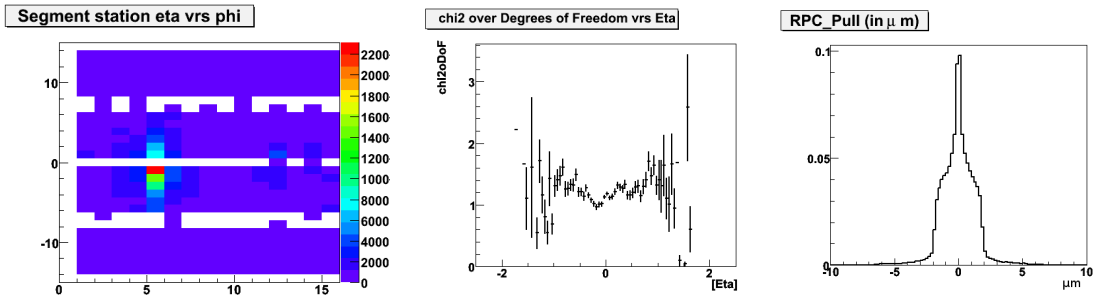

Figure 6.3: The η - ϕ map of the reconstructed segment stations (left). χ^2/NDF of the track vs η station (middle). RPC hit on-track pull distribution (right). Images taken from [2].

- **Physics monitoring:** The last step of the Muon DQM is the Physics monitoring. At this "high-level" stage, the di-muon decays of known resonances, like J/ψ and

the Z boson, are used in order to probe the performance of the muon system and in particular the alignment of the chambers, the magnetic field mapping and material effects. The parameter of interest used in order to acquire the aforementioned information is mainly the invariant mass distribution of the di-muon pair. Figures 6.4 and 6.5 show such distributions coming from J/ψ and Z decays in 8 TeV data collected with the ATLAS detector in 2012.

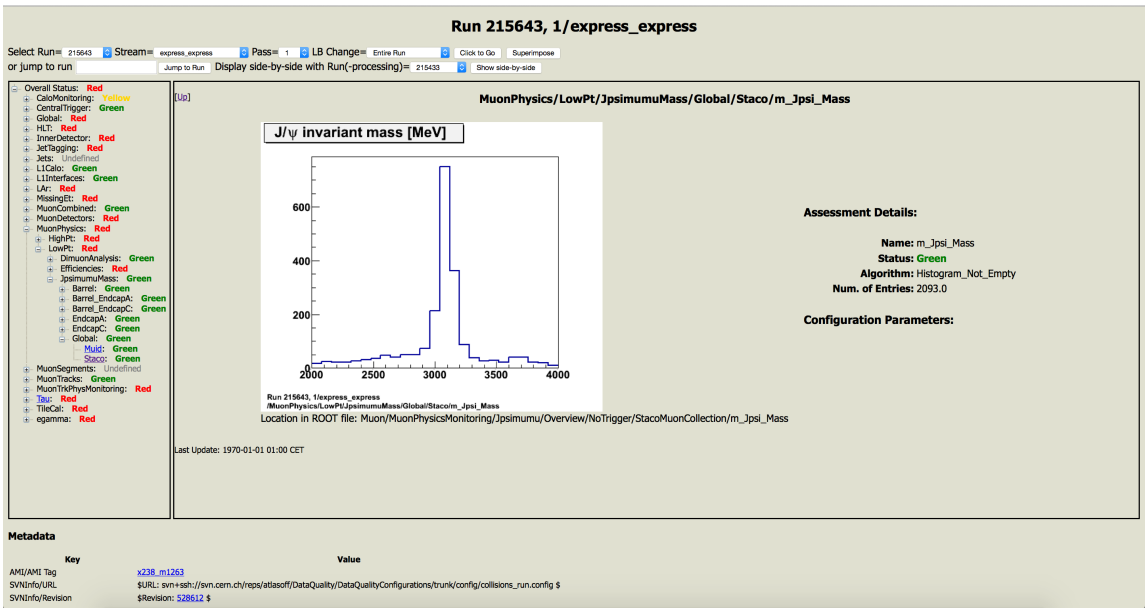

Figure 6.4: Muon DQMF web display of the Physics monitoring package. The invariant mass distribution of J/ψ di-muon decays is shown.

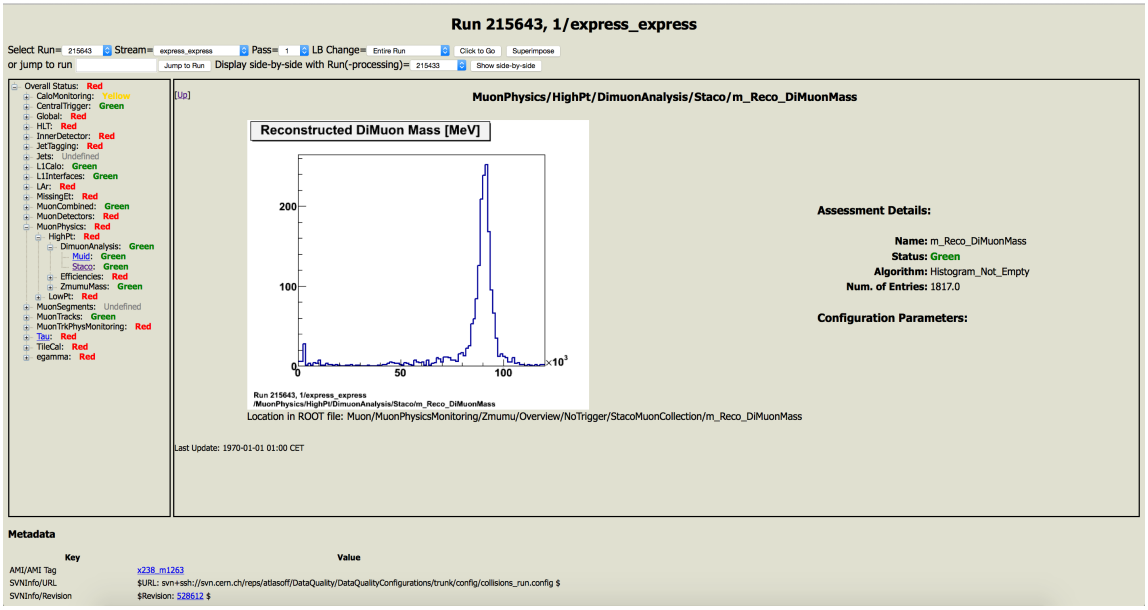

Figure 6.5: Muon DQMF web display of the Physics monitoring package. The invariant mass distribution of all di-muon decays is shown. The J/ψ and Z peaks are well reconstructed.

Bibliography

[1] M. Hauschild, H. Hadavand, R. Kehoe, A. Corso-Radu, and S. Kolos, *Data Quality Monitoring Framework for the ATLAS experiment at LHC*, IEEE Trans.Nucl.Sci. **55** (2008) 417–420.

[2] ATLAS Muon Offline DQA Collaboration Collaboration, I. A. Christidi, *The offline data quality monitoring system of the ATLAS muon spectrometer*, J.Phys.Conf.Ser. **219** (2010) 042035.

Chapter 7

Performance

An *in situ* determination of the performance of the ATLAS detector provides a complementary approach to MC simulation. A generic method, widely used in HEP experiments, to calculate efficiency in detecting and measuring Physical objects is the so-called tag-and-probe method. It was developed and first used in the Tevatron experiments [1] and has been adopted by ATLAS and CMS. Initially in ATLAS it was used for measuring the efficiency of high-p_{T} leptons from Z decays in data and it was extended to the low-p_{T} region[1] using decays from J/ψ and Υ to muons, in order to compute the efficiency of low-p_{T} muons. The low-p_{T} region is important in multi-muon final-states of several SM processes (like $Z\bar{b}$, $W^{\pm}Z$, ZZ^{*}, e.t.c) but also in SUSY searches in Physics searches related to the Higgs mechanism.

This chapter is organised in three sections: The first section describes the method itself and presents the feasibility study performed in MC, right before the first LHC data-taking period, to primarily study the low-p_{T} region of muons using J/ψ decays, but also to extend this study to the Z overlap region, using the Υ resonance muon decays [2]. The second part presents the results of the method using 40 pb^{-1} of 2010 ATLAS data [3], while in the last part, the application of the method in the $W^{\pm}Z$ analysis for the calculation of muon isolation[2] scale factors[3] is presented.

[1] This task granted authorship within the context of the ATLAS experiment to the author of this thesis.

[2] The calorimetric-based isolation of a lepton ℓ, is defined as the ratio: $\sum_{\delta R<0.2} E_t^i/E_t^{\ell}$, where the sum indicates the total transverse energy of all the particles inside a cone of opening 0.2. Another type of isolation is the so-called track-based isolation of a particle, calculated in the ID and defined by: $\sum_{\delta R<0.2} p_t^i/p_t^{\ell}$.

[3] The scale factors are multiplication correction factors that are applied to MC in order to match the

7.1 The tag-and-probe method

The tag-and-probe method exploits the complementarity of two ATLAS detector subsystems, the ID and the MS, regarding muon momenta measurements. The ID complements the performance of the MS at momenta below 100 GeV. Using dimuon decays of well-known resonances, such as J/ψ, Υ and the Z boson, one of the muons is reconstructed in both subsystems and the other one is reconstructed only in one of them, in order to probe the efficiency of the other.

The two muons, namely the "tag" and the "probe", are required to pass two different sets of identification and selection criteria. The tag muon is defined as the muon of the pair that is reconstructed in both subsystems and it it required to pass stringent criteria. These criteria are relaxed[4] in the case of the other muon of the pair, namely the probe, which is only reconstructed in one of the two subsystems under study. Efficiency can be then computed by calculating the ratio of the tag and probe muon pairs in a narrow mass window around the mass region of the resonance that fulfill the specific property under study, over all tag and probe muon pairs around the same mass window. This is valid under the no-background hypothesis. In the case of background presence, this has to be estimated and subtracted from both sets before the efficiency calculation. The criteria on the tag can be the same for a large variety of efficiency measurements; on the other hand, the criteria on the probe have to be varied according to the specific measurement (identification, reconstruction, trigger, scale factor calculation, e.t.c) and the factorisation scheme that was chosen to express the efficiency under study. Figure 7.1 presents a schematic drawing of the method.

7.2 Single lepton trigger feasibility study

The aim of this study is to demonstrate the feasibility of the tag and probe method to measure lepton efficiency (in particular muon identification and reconstruction efficiency in the MS), using fully simulated MC events with J/ψ and Υ dimuon decays selected with a single-muon trigger, in order to probe the low-p_{T} region (<20 GeV). The events are normalised to an integrated luminosity of 10 pb^{-1}, since the aim is to measure the

simulated trigger, reconstruction, identification and isolation efficiency closer to the ones measured in data.

[4]The selection criteria in the case of the probe muon are relaxed in order to avoid introducing biases.

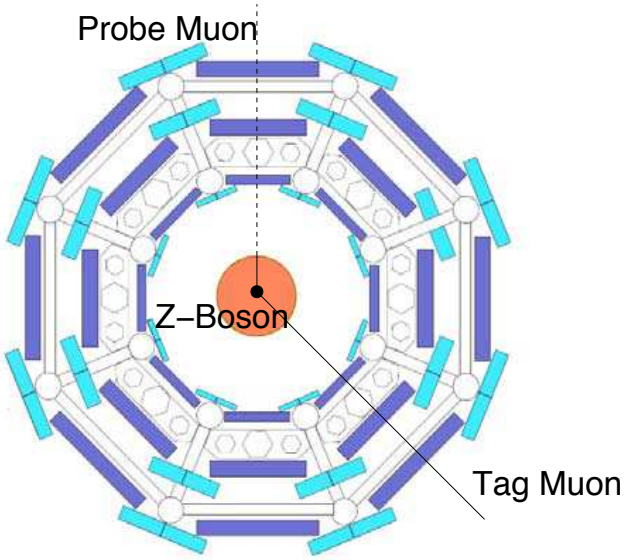

Figure 7.1: Schematic illustration of the tag and probe method [4]. The solid line represents the tag muon that is reconstructed in both detector subsystems (ID and MS). The dashed line indicates the probe muon which is reconstructed in only one of the subsystems (ID). The invariant mass of the tag and probe di-muon system should be within a narrow window of the mass of a known resonance (in the figure the di-muon pair comes from the decay of a Z boson).

aforementioned efficiency with the very first LHC data.

7.2.1 MC samples

`PYTHIA-6.4` [5], including the standard ATLAS tuning [6] was used in order to produce all MC samples used for this study. The simulated samples contain only the hard process and no pile-up events have been included. The signal datasets include the prompt production of the J/ψ and Υ resonances and their consequent decays to muon pairs:

$$\begin{aligned} pp \rightarrow J/\psi \rightarrow \mu^+\mu^- \\ pp \rightarrow \Upsilon \rightarrow \mu^+\mu^- \end{aligned} \tag{7.1}$$

Table 7.1 lists the MC samples used in this study, along with their cross-sections and the integrated luminosity they correspond to. The signal samples are the promptly produced J/ψ and the Υ(1S). The cross-sections for the Υ states take into account the chain feeding from the higher to the lower states (i.e Υ(3S) $\rightarrow$ Υ(2S) $\rightarrow$ Υ(1S)). The main background in the J/ψ case are di-muon pairs from indirectly produced J/ψ. In

both the J/ψ and the Υ cases, the background comprises mainly of the di-muon pairs coming from $b\bar{b}$, $c\bar{c}$ decays and much less from the Drell-Yan process. The $b\bar{b} \to \mu 4\mu 4X$, $c\bar{c} \to \mu 2.5\mu 2.5X$[5] samples, due to their small cross-sections, contribute slightly to the total background, with the bulk of it being mainly di-muon pairs coming from the $b\bar{b} \to \mu 4X$ and $c\bar{c} \to \mu 4X$ processes. Finally, a very small contribution in the total background comes from di-muon pairs originating from the Drell-Yan process. It should be noted that due to the low statistics in all $b\bar{b}$, $c\bar{c}$ samples, along with the small cross-sections of the aforementioned quark-antiquark decays to di-muon pairs, a realistic estimate of the background contribution (to both J/ψ and Υ) was not possible.

Process	$\sigma(nb)$	$\int \mathscr{L} dt(pb^{-1})$
$pp \to J/\psi(\mu 4\mu 4)X$	30.0	5.0
$b\bar{b} \to J/\psi(\mu 4\mu 4)X$	13.5	3.7
$pp \to \Upsilon(1S)(\mu 2.5\mu 2.5)X$	90.0	2.2
$pp \to \Upsilon(2S)(\mu 2.5\mu 2.5)X$	26.0	7.3
$pp \to \Upsilon(3S)(\mu 2.5\mu 2.5)X$	20.0	9.9
$b\bar{b} \to \mu 4\mu 4X$	88.7	0.73
$c\bar{c} \to \mu 2.5\mu 2.5X$	261.0	3.8
$DY \to \mu 2.5\mu 2.5$	3.0	83.1
$b\bar{b} \to \mu 4X$	13170.0	$7.6{\cdot}10^{-3}$
$c\bar{c} \to \mu 4X$	7900.0	$8.9{\cdot}10^{-3}$

Table 7.1: Simulated data sets used for "direct" quarkonia, "indirect" J/ψ and the relevant background processes. The respective cross-sections and the available luminosity of the samples is listed.

7.2.2 Event selection

The event selection starts with the search for at least one muon of high quality, i.e passing a set of stringent cuts. This muon is labeled as the tag. Then all ID tracks are imposed on a series of looser requirements in the quest for the second muon of the decay. The ID track passing these cuts is the probe. The resonance used will define the requirements on the tag-probe pair, since they have different properties (kinematics, masses, mass resolutions).

[5]The lack of a $c\bar{c} \to \mu 4\mu 4X$ sample at the time of the study enforced the usage of the existing $c\bar{c} \to \mu 2.5\mu 2.5X$ sample.

Tag selection

Tag muons are selected by the following selection criteria:

1. The tag muon should be Combined (CB);
2. The kinematics should be p_{T}> 6 GeV, $|\eta|$ <2.5;
3. The associated ID track should have at least one hit on the B-Layer of the Pixel detector;
4. A matching is required between the reconstructed muon and the Level-1 muon trigger with p_{T}>6GeV(L1MU6 trigger chain);
5. In addition to the previous requirement, the reconstructed muon should match the triggered muon confirmed at Level-2 (L2mu6 trigger chain);

Figure 7.2 shows the cut-flows of the tag muons, while in Tables 7.2 and 7.3 a summary of the relative cut efficiency is given. The difference in the p_{T} cut is expected due to the different muon p_{T} required at generator level.

Sample	$pp \to J/\psi X$	$b\bar{b} \to J/\psi X$	$pp \to \Upsilon(1S)X$	$pp \to \Upsilon(2S)X$	$pp \to \Upsilon(3S)X$
Tags	%	%	%	%	%
p_{T}	37.25	47.58	21.38	29.35	26.52
η	98.88	98.94	98.96	98.88	98.88
L1/Reco	81.61	82.42	79.64	80.01	80.23
L2/L1	88.42	82.03	88.75	88.52	88.93

Table 7.2: Relative efficiency (with respect to the previous step) of kinematic and trigger cuts for all the signal samples in the tag selection step. The percentages quoted are calculated as the ratios of each step over the previous one.

7.2.3 Tag and probe pairs selection criteria

In each event, each muon that is selected as tag is combined with all other ID tracks (probes) to form di-muon pairs. This way all the possible J/ψ (or Υ candidates) are formed. The studies concerning the J/ψ and Υ resonances are performed separately. Details on the J/ψ selection will be given and only the qualitative differences in the case of the Υ will be mentioned in the following.

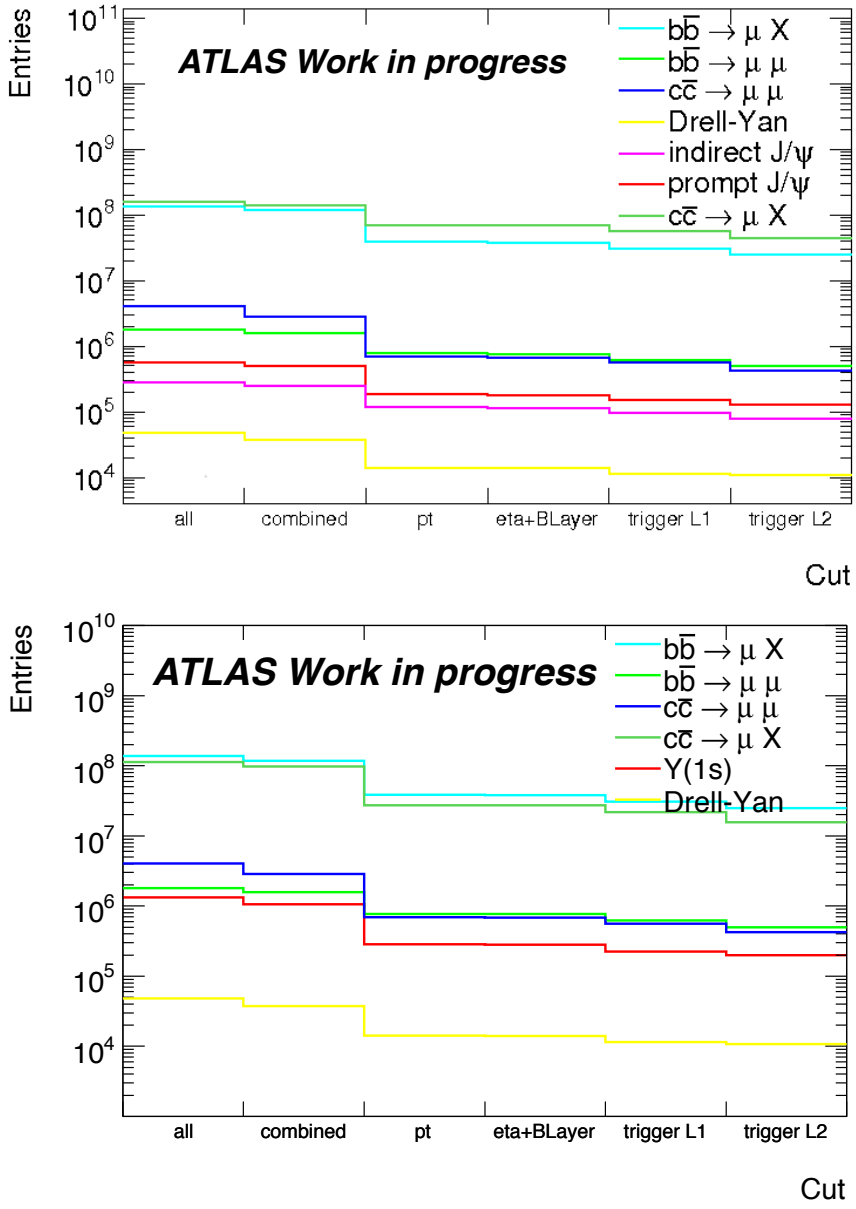

Figure 7.2: Cut-flow selection for signal in J/ψ (top) and Υ events (bottom) for the tag selection.

Sample	$b\bar{b} \to \mu 4X$	$c\bar{c} \to \mu 4X$	$DY \to \mu 2.5 \mu 2.5$	$b\bar{b} \to \mu 4 \mu 4X$	$c\bar{c} \to \mu 4 \mu 4X$
Tags	%	%	%	%	%
p_{T}	32.55	28.33	29.49	28.09	24.02
η	98.91	98.90	98.84	98.91	98.81
L1/Reco	80.34	79.88	82.48	80.34	81.57
L2/L1	81.49	72.20	92.89	81.49	75.96

Table 7.3: Relative efficiency (with respect to the previous step) of kinematic and trigger cuts for all the background samples in the tag selection step. The percentages quoted are calculated as the ratios of each step over the previous one.

J/ψ selection criteria

The following list describes the selection criteria for the tag-probe di-muon pairs originating from the J/ψ resonance:

1. A good quality vertex; the quality of the vertex is defined by it's χ^2 and it is requested that it satisfies χ^2/NDF <6. This cut has a rejection factor of about 4 and 3 against the $b\bar{b} \to \mu X$ and $c\bar{c} \to \mu X$ backgrounds respectively and it also rejects a factor of about 2 the combinatorics background for the signal;

2. 0.1< ΔR_{tp} <0.7: The distance in the $\eta - \phi$ plane of di-muon pairs coming from J/ψ decays should be within the aforementioned range. This selection criterion provides a background rejection factor of about 5 for the two dominant background sources: $b\bar{b} \to \mu X$ and $c\bar{c} \to \mu X$ while it as well reduces the combinatorics background of both prompt and indirect J/ψ by a factor of 1.5;

3. A cut on the pseudo-proper [6] time λ is applied. This cut reduces drastically the indirect J/ψ's but it does not affect the prompt J/ψ yield, while it has a huge impact on the main background sources, rejecting the $b\bar{b} \to \mu X$ process by a factor of 5 and the $c\bar{c} \to \mu X$ one by a factor of 2;

4. $d_0/\sigma_{d_0} < 3.0$: This cut is applied only on the tag muon and since it follows the cut on the pseudo-proper time it has a very limited impact. These two cuts are strongly correlated;

5. The probe ID track should not be an electron;

[6] The pseudo-proper time λ is defined by: $\lambda = L_{xy} \cdot \frac{m_{J/\psi}}{p_T^{J/\psi}}$, where L_{xy} is the transverse decay length.

6. Only tag-probe pairs whose invariant mass is within a narrow window of ±150MeV within the J/ψ mass are kept;

7. In the final step, those di-muon pairs that have a probe track which is also a "muon" are compared against all tag-probe pairs in order to extract the efficiency;

In Tables 7.4,7.5 the effect of each cut for the signal and the background processes in the J/ψ study is presented.

Sample	$pp \to J/\psi X$	$b\bar{b} \to J\psi X$	$b\bar{b} \to \mu 4X$	$c\bar{c} \to \mu 4X$
T-P pairs	%	%	%	%
p_{T}-η	9.93	10.83	9.08	9.50
Charge	49.75	49.04	42.60	44.45
Vertexing	45.63	41.53	24.67	30.43
ΔR	64.12	58.66	17.53	18.12
Pseudo λ	90.27	15.83	17.69	38.19
d_0/σ_{d_0}	99.35	92.95	87.88	92.23
Electron veto	99.95	99.81	97.99	98.73
Invariant mass	96.47	80.80	6.45	3.54
isCB probe muon	87.12	87.51	18.18	68.18

Table 7.4: The effect of each cut relative to the previous one for the tag and probe selection criteria on the J/ψ signal and on the various background sources. The percentages quoted are calculated as the ratios of each step over the previous one.

Sample	$DY \to \mu 2.5 \mu 2.5$	$b\bar{b} \to \mu 4\mu 4X$	$c\bar{c} \to \mu 4\mu 4X$
T-P pairs	%	%	%
p_{T}-η	10.68	11.22	10.29
Charge	47.24	48.54	46.66
Vertexing	46.92	35.42	34.10
ΔR	6.72	30.94	21.12
Pseudo λ	82.81	19.03	32.09
d_0/σ_{d_0}	98.20	84.46	89.89
Electron veto	99.83	99.16	99.26
Invariant mass	5.66	19.68	19.35
isCB probe muon	83.28	84.49	79.29

Table 7.5: The effect of each cut relative to the previous one for the tag and probe selection criteria on the various background sources. The percentages quoted are calculated as the ratios of each step over the previous one.

Table 7.6 gives the expected yields for the signal and background processes at 10 pb^{-1} before and after the last cut of the tag-probe pair selection, while Figure 7.3

shows the invariant mass distribution of the tag and probe candidates (for both signal and backgrounds) before and after the last requirement for the probe to be a muon.

Process	Before	After
$pp \to J/\psi X$	116000	101000
$b\bar{b} \to J\psi X$	9130	7990
$b\bar{b} \to \mu 4X$	23700±6500	3480±1315
$c\bar{c} \to \mu 4X$	9300±6740	5840±3370
$DY \to \mu 2.5 \mu 2.5$	35	30
$b\bar{b} \to \mu 4 \mu 4X$	620	370
$c\bar{c} \to \mu 4 \mu 4X$	1065	368

Table 7.6: J/ψ signal and background events expected at 10 pb^{-1} before and after the last cut of the tag-probe pair selection.

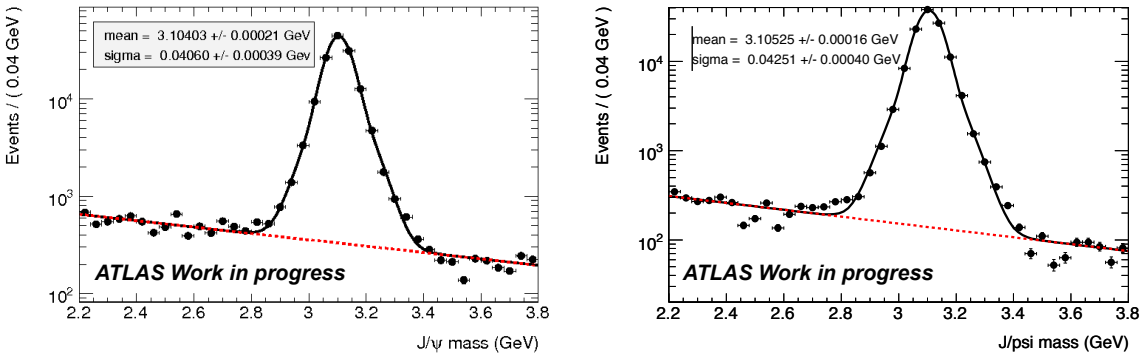

Figure 7.3: Invariant mass distribution of the tag and probe candidates for both signal and backgrounds, before the requirement on the probe to be a muon (left) and after it (right) in the J/ψ study.

Υ selection criteria

The list of selection criteria for the tag-probe pairs in the case of the Υ resonance is similar to the one used in the J/ψ selection but with two differences, in order to account for the different kinematics and mass resolution:

1. 0.7< ΔR_{tp} <3.0: The distance in the $\eta - \phi$ space of di-muon pairs coming from Υ decays should be within the aforementioned range. This selection criterion does not provide a significant background rejection, since it has a large range.

2. Only tag-probe pairs whose invariant mass is within a narrow window of ±500MeV within the Υ mass are kept;

In Tables 7.7,7.8 the effect of each cut for the signal and the background processes in the Υ study is presented, while Table 7.9 gives the expected yields for the signal and background processes at 10 pb^{-1} before and after the last cut of the tag-probe pair selection. In Figure 7.4 the invariant mass distribution of the tag and probe candidates (for both signal and backgrounds) before and after the last requirement for the probe to be a muon is presented. In order to cope with the higher backgrounds in this case, isolation (both track-based and calorimetric) cuts should be applied along with further ID cuts in the studies with real data. In this MC study, these isolation cuts were not applied however.

Sample	$pp \to \Upsilon(1S)X$	$pp \to \Upsilon(2S)X$	$pp \to \Upsilon(3S)X$	$DY \to \mu 2.5 \mu 2.5$
T-P pairs	%	%	%	%
p_{T}-η	8.67	9.03	9.17	10.68
Charge	41.55	43.41	44.25	47.24
Vertexing	26.48	31.58	33.72	46.92
ΔR	79.15	83.17	82.82	70.04
Pseudo λ	46.44	57.54	58.74	65.52
d_0/σ_{d_0}	99.26	98.81	98.60	98.27
Electron veto	99.51	99.69	99.67	99.63
Invariant mass	73.87	83.88	85.57	7.63±0.7
isCB probe muon	83.82	83.17	82.55	79.10±8.0

Table 7.7: The effect of each cut relative to the previous one for the tag and probe selection criteria on the Υ signal and on the various background sources. The percentages quoted are calculated as the ratios of each step over the previous one.

Sample	$b\bar{b} \to \mu 4X$	$c\bar{c} \to \mu 4X$	$b\bar{b} \to \mu 4 \mu 4X$	$c\bar{c} \to \mu 2.5 \mu 2.5X$
T-P pairs	%	%	%	%
p_{T}-η	9.08	9.50	11.22	10.29
Charge	42.60	44.45	48.54	46.66
Vertexing	24.67	30.43	35.42	34.10
ΔR	68.43	61.36	72.21	66.11
Pseudo λ	14.99	19.66	17.02	22.61
d_0/σ_{d_0}	84.12	86.71	78.99	84.68
Electron veto	96.91	97.77	98.93	98.94
Invariant mass	10.49±1.1	8.04±0.8	8.29	8.43
isCB probe muon	8.04±0.25	1.23±1.23	40.12	25.58

Table 7.8: The effect of each cut relative to the previous one for the tag and probe selection criteria on the various background sources in the Υ resonance selection. The percentages quoted are calculated as the ratios of each step over the previous one.

Process	Before	After
$pp \to \Upsilon(1S)(\mu 2.5\mu 2.5\mu 2.5)X$	28966	24280
$pp \to \Upsilon(2S)(\mu 2.5\mu 2.5\mu 2.5)X$	20716	17229
$pp \to \Upsilon(3S)(\mu 2.5\mu 2.5\mu 2.5)X$	21369	17640
$b\bar{b} \to \mu 4X$	147625±13949	11863±3954
$c\bar{c} \to \mu 4X$	91314±10157	1129±1129
$DY \to \mu 2.5\mu 2.5$	376	282
$b\bar{b} \to \mu 4\mu 4X$	4694± 253	1883± 160
$c\bar{c} \to \mu 2.5\mu 2.5X$	6194± 127	1584± 64

Table 7.9: Υ signal and background events expected at 10 pb^{-1} before and after the last cut of the tag-probe pair selection.

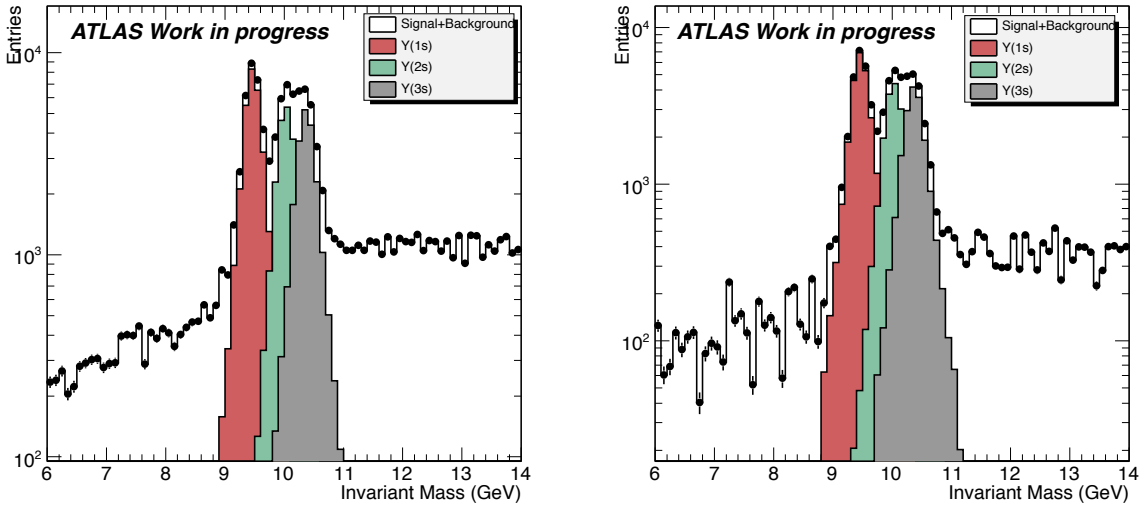

Figure 7.4: Invariant mass distribution of the tag and probe candidates for both signal and backgrounds, before the requirement on the probe to be a muon (left) and after it (right) in the Υ study.

7.2.4 Background subtraction

In order to measure the efficiency using the tag and probe method, the background contributions have to be taken into account and subtracted, especially in the case of the Υ resonance. For this reason the simple side band method has been used in this analysis. A brief description of the method is given in the following.

The simple side band method

The simple side-band method utilises the di-muon invariant mass as the discriminating variable in order to distinguish the signal from the background. The integral of background events is obtained in a fixed number of bins in areas left and right of the resonance, several sigmas away from it in order to ensure the absence of signal events. A linear background shape is assumed in the selected signal region and side bands and by means of interpolation the number of events under the mass peak, where the background subtraction will be applied is calculated. Since the number of bins under the peak of the resonance in use is smaller than in the side bands, a multiplication factor is obtained in order to obtain the correct number of background events.

The shape of the background distributions for the discriminating variable is obtained from either one or both of the side band regions and it is normalised accordingly to the number of events in the signal region as above. The shapes of the p_{T}, η and ϕ distributions of di-muon pairs in our case are obtained and normalised to the number of events in the signal region. These distributions are then subtracted from the ones in the signal region, both before and after the last cut of the muon requirement on the probe track, provided that the background survives this last cut (for instance in the J/ψ case the background contribution after the last step is at the level of a few percent).

7.2.5 Results

The results of the tag and probe method in measuring the reconstruction efficiency of muons are presented in this section for J/ψ and Υ. For both resonances, the efficiency is extracted using the fully simulated MC samples and these results are compared to the ones obtained by using only generator-level particles whose origin is known, coming from the same MC samples. These results are mentioned in the efficiency plots and everywhere else hereafter as the MC Truth.

J/ψ

The efficiency plots, to reconstruct a muon as CB, with respect to p_{T}, η and ϕ are shown in Figure 7.5, while in Figure 7.6 the respective efficiency to reconstruct a muon as CB or MuTag is presented. In both of the cases the results are compared to the ones extracted using the MC Truth.

The efficiency is computed with and without background subtraction (using the simple side-band method), yielding comparable results. This is expected since the background contribution in the J/ψ case is about 1.4% and 0.7% of the signal yield, before and after the last requirement of the probe to be a muon. The agreement with the MC based efficiency is better then 1%.

Υ

In Figure 7.7 the muon reconstruction efficiency is presented for all three Υ states. Contrary to the J/ψ case, the background subtraction procedure is necessary in order to obtain meaningful results, since the contribution to the signal region in this case reaches more than 15% and more than 5% before and after the final requirement of the probe to be a muon respectively. The agreement between the three background subtraction methods tested is at the level of 97%. Finally, MC truth expectations are in good agreement with the results obtained after the background subtraction.

7.2.6 Conclusions

A feasibility study using the tag and probe method and MC simulated data was presented. The goal was to test if it is possible to measure the muon reconstruction efficiency using di-muon pairs from J/ψ and Υdecays, in order to probe the low-p_{T} region. It was shown that the J/ψ resonance may be used for efficiency measurements since the backgrounds (mainly coming from the $b\bar{b} \rightarrow \mu X$ source) can be well estimated so that the method can be applied. However, the Υ resonance, due to different mass resolution as well as the overlap between it's three states, may not be a suitable candle in order to extract the muon reconstruction efficiency with the first LHC data.

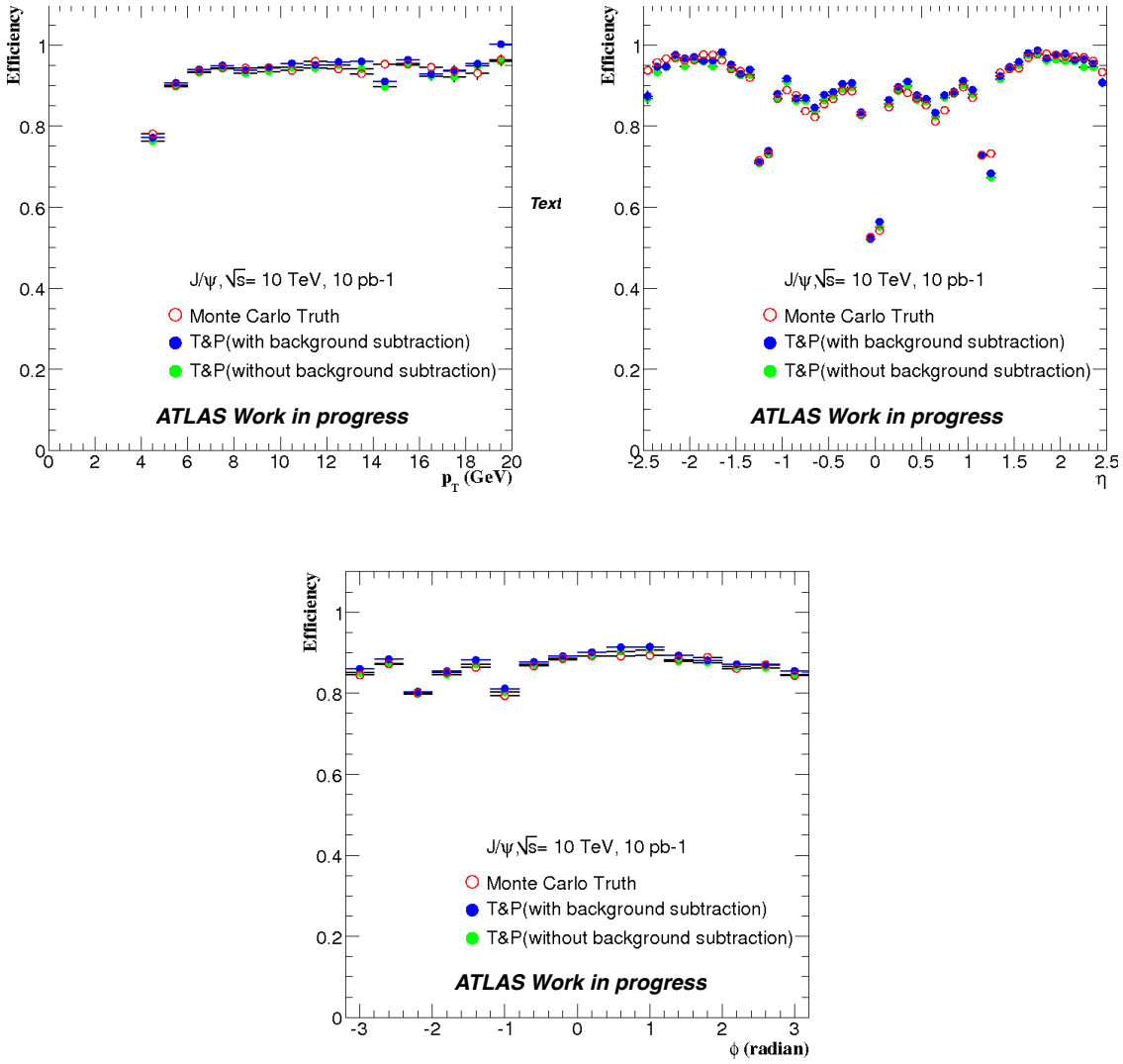

Figure 7.5: Combined muon efficiency using the Tag and Probe method for selecting J/ψ, for p_{T} (top left), η (top right) and ϕ (bottom middle) variables respectively. Blue and green dots: with and without side band background subtraction method, open red circles: results from efficiency extracted using the MC Truth (see text).

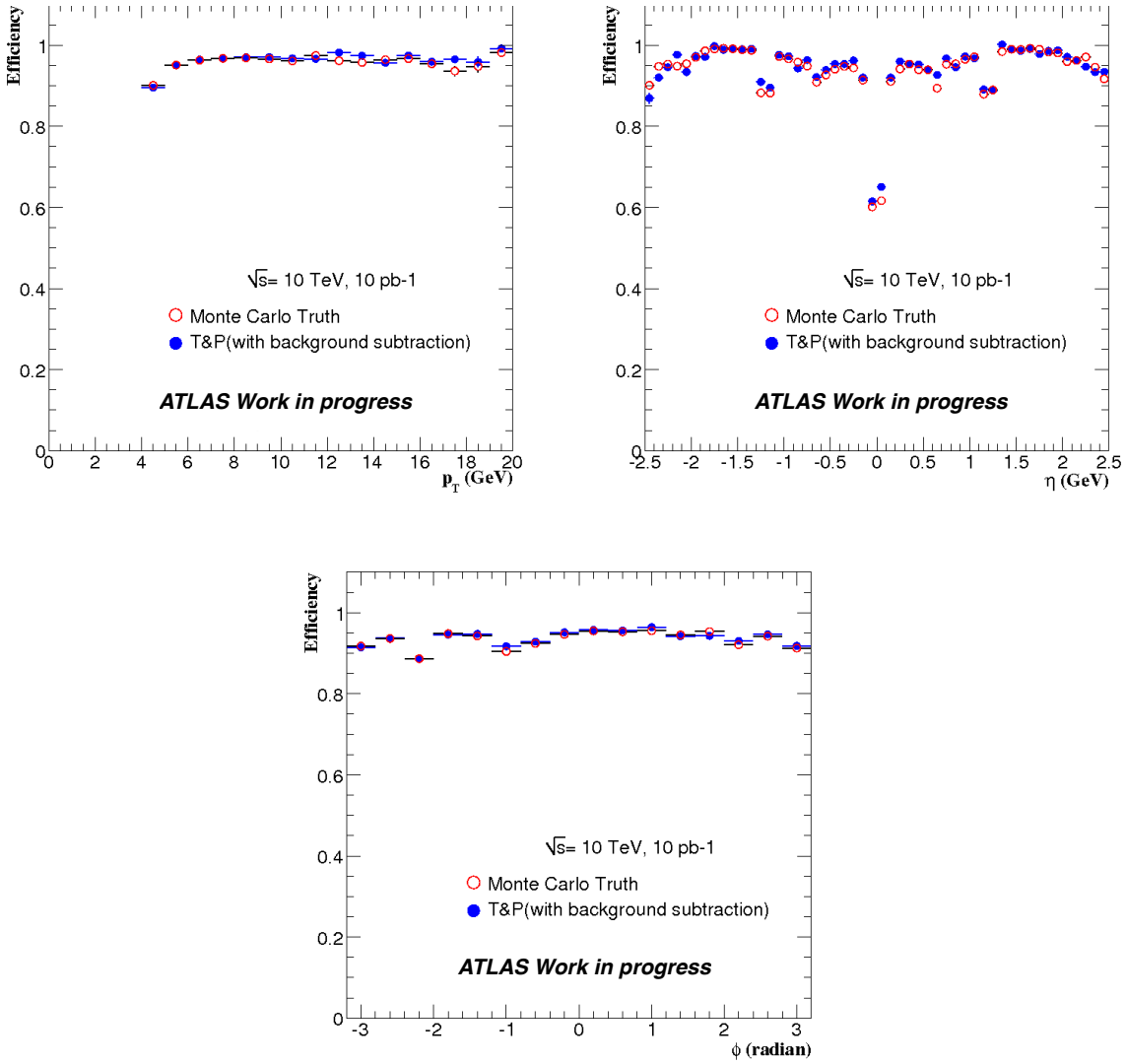

Figure 7.6: Combined and MuTag muon efficiency using the Tag and Probe method for selecting J/ψ, for p_{T} (top left), η (top right) and ϕ (bottom middle) variables respectively. Blue and green dots: with and without side band background subtraction method, open red circles: results from efficiency extracted using the MC Truth (see text).

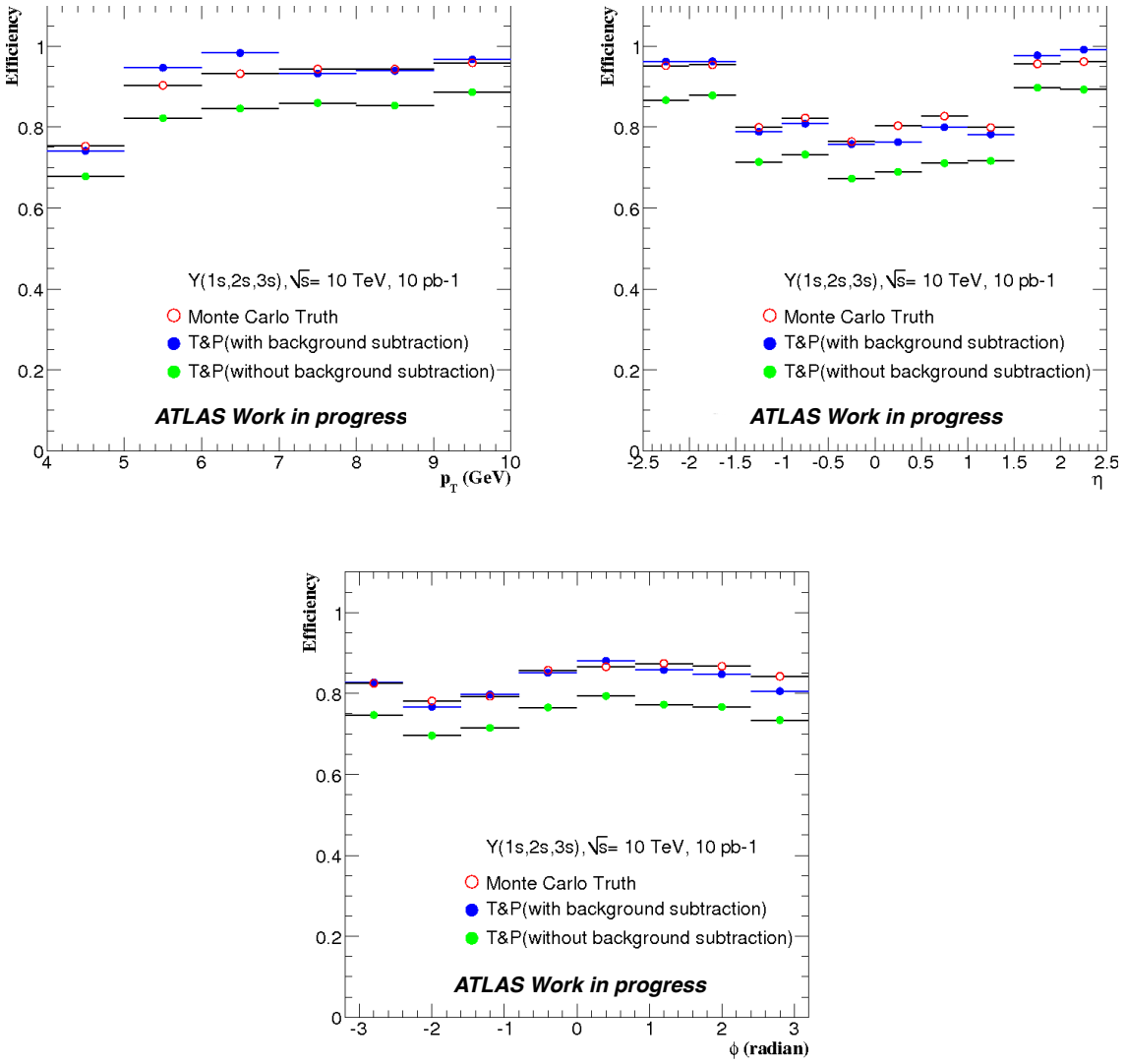

Figure 7.7: Combined muon efficiency using the Tag and Probe method for selecting Υ, for p_{T} (top left), η (top right) and ϕ (bottom middle) variables respectively. Blue and green dots: with and without side band background subtraction method, open red circles: results from efficiency extracted with MC (see text).

7.3 Muon reconstruction efficiency using 2010 data

Using a data sample corresponding to 40 pb^{-1} of pp collisions recorded in 2010, the performance of the muon reconstruction, in terms of reconstruction and isolation efficiency, was studied for different classes of reconstructed muons. Results were obtained from an analysis of J/ψ and Z decays to di-muon pairs and they are compared to MC predictions. The J/ψ candle is used in order to probe the low-p_{T} region (2.2 GeV $< p_{\mathrm{T}} <$ 10 GeV) while the Z candle to access the 20 GeV $< p_{\mathrm{T}} <$ 100 GeV region. The in between region (10 GeV $< p_{\mathrm{T}} <$ 20 GeV) is inaccessible due to the following facts:

- The very limited statistics of muons coming from J/ψ decays with $p_{\mathrm{T}} > 10$ GeV;
- The difficulty to control the backgrounds in the low-p_{T} region when using the sample of Z decays;

7.3.1 Event selection

The dataset used was recorded using a single-muon trigger. The minimum p_{T}-threshold of the muon that triggered the event was required to be 4, 6, 10 or 13 GeV to cope with the increasing trigger rates during the data-taking period. In order to suppress non-collision background events, at least three ID tracks had to be associated with the reconstructed primary vertex. The ID tracks were required to satisfy a series of track-quality criteria:

1. At least two Pixel hits, of which at least one in the B-Layer;
2. At least six SCT hits;
3. At least five hits and outliers in the TRT for $|\eta| <$1.9 with an outlier fraction of <90%, in order to suppress fake tracks and to discriminate muons from π/K decays;

Tag selection

1. The muons has to be CB and to have triggered the event;
2. $p_{\mathrm{T}} > 4$ GeV, $|\eta| <$2.5;
3. $|d_0| <0.3mm$, $|z_0| <1.5mm$, $|d_0|/\sigma_{d_0} <3$, $|z_0|/\sigma_{z_0} <3$;

Probe selection

1. The associated ID tracks to the muons have to pass the track-quality criteria mentioned above;

2. $p > 3$ GeV, $|\eta| < 2.5$;

3. The tag and the probe muons should be oppositely charged and originate from the same vertex;

4. The ΔR opening angle should be less than 3.5;

5. The invariant mass of the tag-probe system should be within 2 and 3.6 GeV;

7.3.2 Results using the J/ψ candle

Figures 7.8, 7.9 show the reconstruction efficiency, with respect to ID tracks, for two different muon reconstruction algorithms (see chapter 5, reconstruction), `Moore` referred to as chain 1 and `MuonBoy` referred to as chain 2 hereafter. The efficiency is given for two distinct reconstructed muon categories, CB and CB+ST muons stemming from J/ψ decays. The efficiency is given as a function of the probe p_{T}, for five bins of $|\eta|$. Unlike the case where the Z-boson is used in the high-p_{T} range, since the J/ψ may be produced inside jets, an isolation requirement in order to select a pure sample cannot be applied; in this case, the invariant mass distribution of the tag-and-probe pairs is fitted using the sum of a Gaussian signal term and a quadratic term to account for the background.

Systematic checks

The following tests were performed in order to evaluate the systematics of the analysis:

- Signal shapes: The Gaussian terms in the fit were allowed to vary independently their means and widths;

- Background shape: Instead of the quadratic parameterisation of the background shape a linear shape was used in the fit. In this case, the fit was performed in the range 2.7-3.5 GeV (instead of the range from 2.0 to 3.6 GeV);

- Alternative fit: By performing a second fit to the matched and the total (matched and unmatched) distributions. This method, even though it does not directly account for the correlations between the two samples nor it provides an easy way to propagate the uncertainties from the background subtraction, profits from a higher stability of the two simpler fits;

7.4 Tag and probe to extract muon isolation efficiency

The tag and probe method is used for the extraction of isolation scale factors for muons coming from the decays of W and/or Z bosons. The selection criteria in this case on the tag muon are as follows:

1. The tag muon has to be CB;
2. p_{T}>25GeV;
3. It has to be trigger matched;
4. ID requirements imposed on the tag track: the number of Pixel hits plus the number of crossed dead Pixel sensors should be more than zero; the number of SCT hits plus the number of crossed dead SCT sensors should be more than four; the number of Pixel holes plus the number of SCT holes should be less than three; finally, let n be the sum of the number of TRT hits (n_{TRT}^{hits}) plus the number of TRT outliers ($n_{TRT}^{outliers}$). Then it is required that $n > 5$ and $n_{TRT}^{outliers} < 0.9\ n$, for tracks in the pseudorapidity region $0.1 < |\eta| < 1.9$.
5. $|\eta| < 2.4$;
6. $z_0^{PVC} \times \sin(\theta) < 0.5$ mm;
7. $|d_0|/\sigma_{d_0} < 3.0$;
8. Track isolation: $\frac{p_T^{\mathrm{cone40}}}{p_T^{\mu}} < 0.1$;

Two "working points" are defined for the probe muon, depending on the selection criteria imposed on the lepton whose isolation scale factor is under study, namely the W and Z working points. As a result, two sets of selection cuts are defined here for the probe muon (mentioned in parentheses are the W working point criteria):

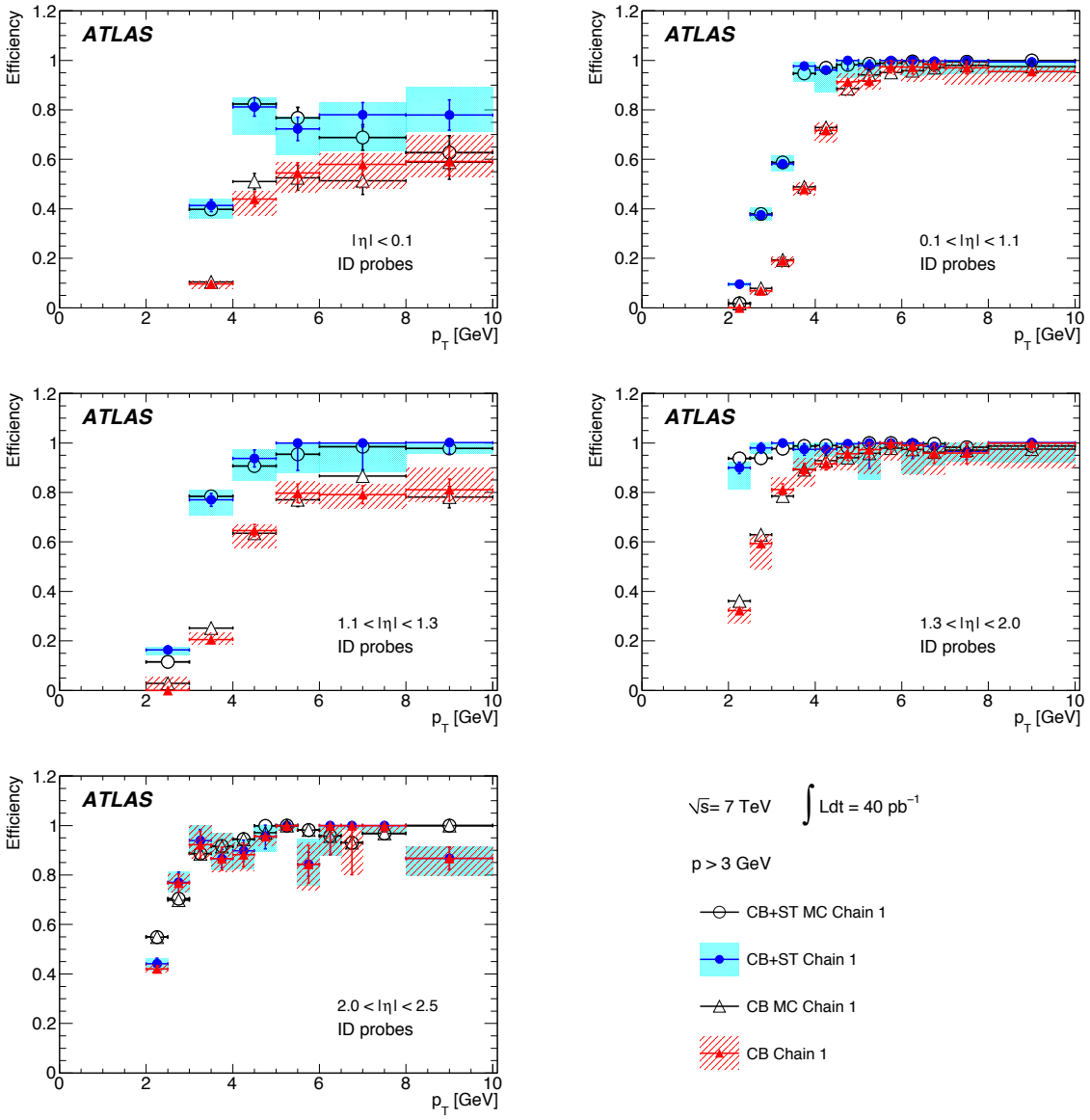

Figure 7.8: Efficiency for chain 1 CB and CB+ST muons with momentum p >3 GeV (from J/ψ decays), as a function of p_{T}, for five bins of $|\eta|$ as described in the legend, for data and MC events. The error bars represent the statistical uncertainties while the bands around the data points represent the statistical and systematic uncertainties added in quadrature.

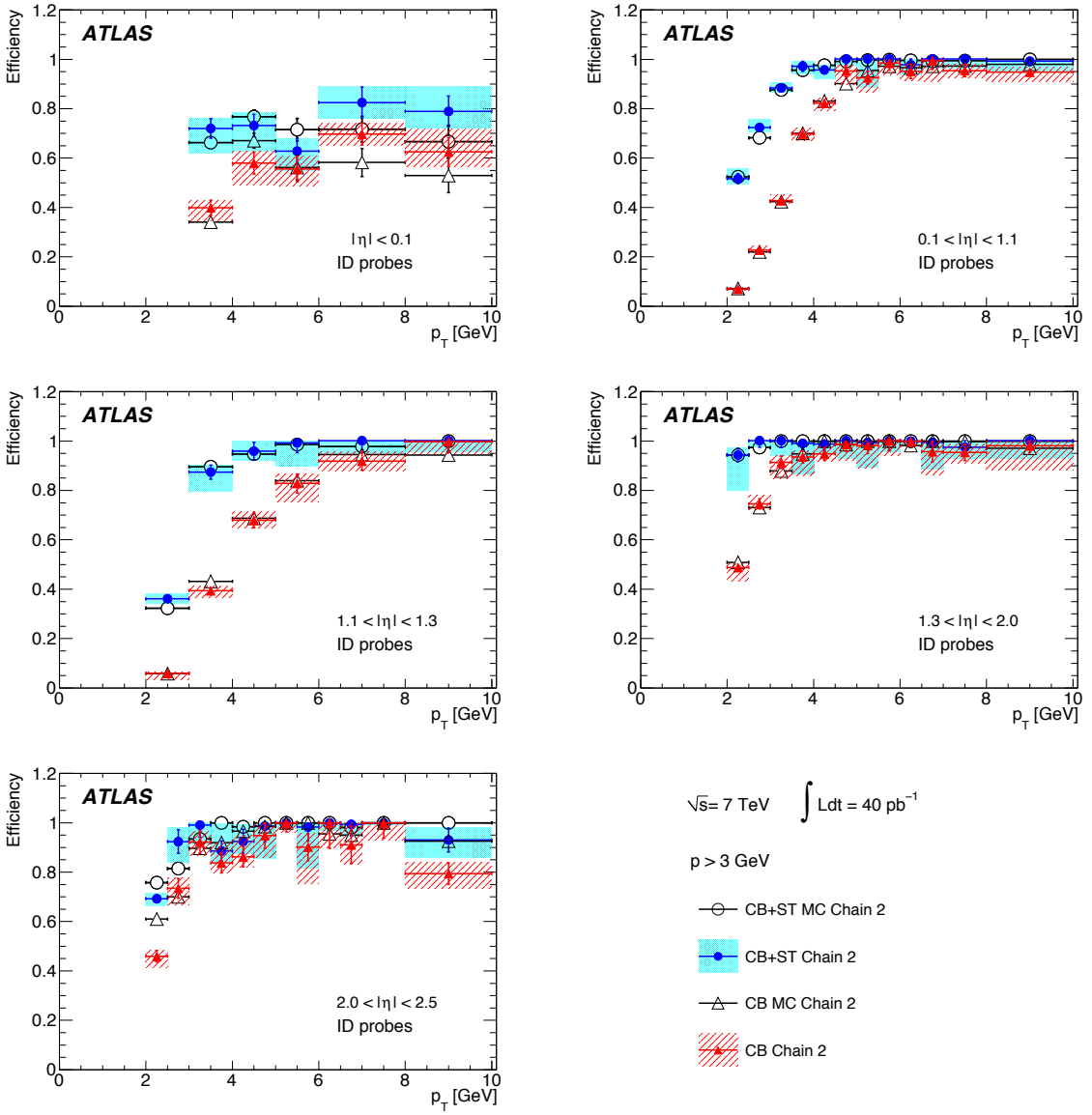

Figure 7.9: Efficiency for chain 2 CB and CB+ST muons with momentum p >3 GeV (from J/ψ decays), as a function of p_{T}, for five bins of $|\eta|$ as described in the legend, for data and MC events. The error bars represent the statistical uncertainties while the bands around the data points represent the statistical and systematic uncertainties added in quadrature.

1. Combined or Segment Tagged muon (Combined);
2. p_{T}>15GeV (20);
3. ID requirements imposed on the tag track: the number of Pixel hits plus the number of crossed dead Pixel sensors should be more than zero; the number of SCT hits plus the number of crossed dead SCT sensors should be more than four; the number of Pixel holes plus the number of SCT holes should be less than three; finally, let n be the sum of the number of TRT hits (n_{TRT}^{hits}) plus the number of TRT outliers ($n_{TRT}^{outliers}$). Then it is required that $n > 5$ and $n_{TRT}^{outliers} < 0.9\ n$, for tracks in the pseudorapidity region $0.1 < |\eta| < 1.9$.
4. $|\eta|$ <2.4;
5. $z_0^{PV} \times \sin(\theta) < 0.5$ mm;

Finally the set of selection criteria imposed on the tag-probe pairs is defined by:

1. Opposite charge;
2. $|\Delta z_0|$ <3.0;
3. $|\Delta d_0|$ <2.0;
4. $|\Delta\phi|$ <2.0;
5. $|\Delta R|$ <0.3;
6. $|M_Z^{\mathrm{PDG}} - M_{\mathrm{TP}}|$ <10GeV;

where Δx refers to the difference between the tag and probe on the specific variable x : z_0, d_0, ϕ, R.

The probe tracks are distributed in η and p_{T} as shown in Figure 7.10 for data and Monte Carlo simulation. An overall acceptable agreement is found. The data invariant mass distribution of the tag and probe pairs also shows a good agreement with the Monte Carlo expectation.

To determine the isolation efficiency, the number of probes which can be matched to a combined reconstructed muon passing the isolation requirement has been counted. The

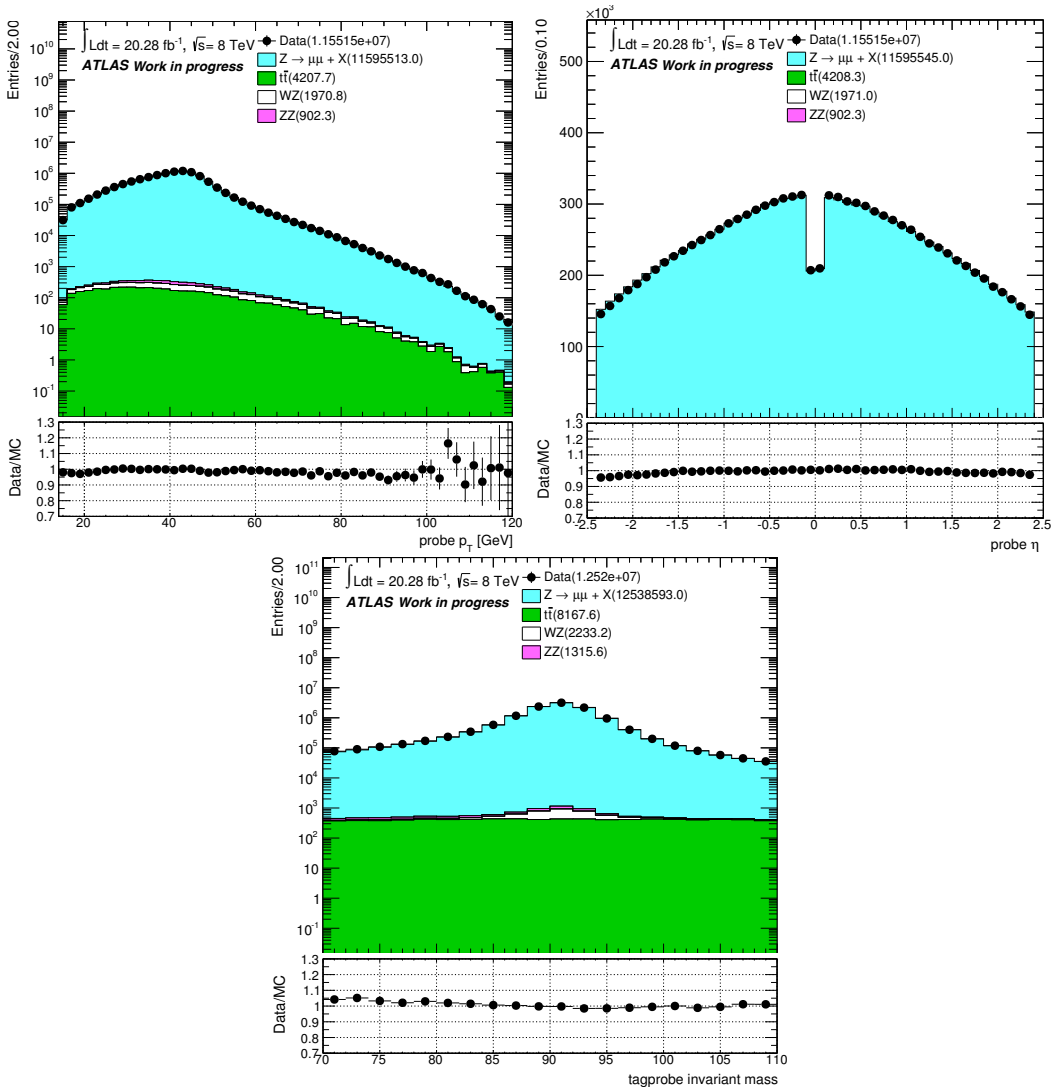

Figure 7.10: Distributions of combined probe tracks used to measure the efficiency of isolation, in comparison with the Monte Carlo expectation.

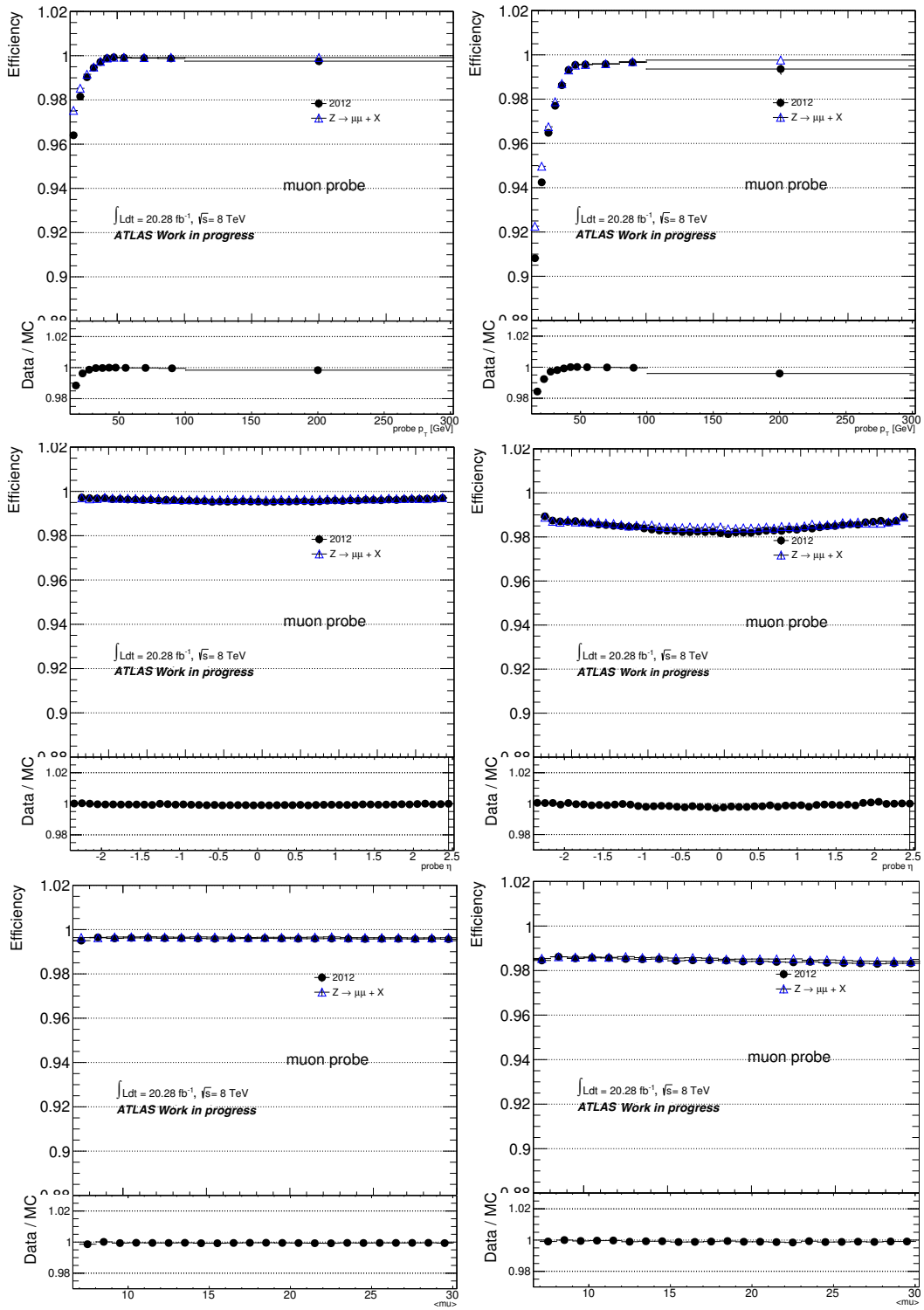

Figure 7.11: Isolation efficiency versus probe p_{T} for the Z working point (top left) and the W working point (top right). Isolation efficiency versus probe η for the Z working point (middle left) and the W working point (middle right). Isolation efficiency versus $< \mu >$ for the Z working point (bottom left) and the W working point (bottom right).

dependence of efficiency and SF from p_{T}, η and $< mu >$ are shown in Figure 7.11. The data-MC efficiency comparison shows that the SF is very close to unity.

From the left plot of Figure 7.11 it is evident that there is a small dependence of the isolation SF on the p_{T}, while with respect to η the dependence can be considered as negligible. The SF values in each of the p_{T} and for both isolation working points (W and Z) are reported in Table 7.10.

Bin[GeV]	Scale Factor - Z muon	Scale Factor - W muon
15 - 20	$0.9885^{+0.0004}_{-0.0004}$	-
20 - 25	$0.9962^{+0.0002}_{-0.0002}$	$0.9924^{+0.0003}_{-0.0004}$
25 - 30	$0.9987^{+0.0001}_{-0.0001}$	$0.9972^{+0.0002}_{-0.0002}$
30 - 35	$0.9997^{+0.0001}_{-0.0001}$	$0.9982^{+0.0001}_{-0.0001}$
35 - 40	$0.9997^{+0.0000}_{-0.0000}$	$0.9992^{+0.0001}_{-0.0001}$
40 - 45	$1.0000^{+0.0000}_{-0.0000}$	$1.0001^{+0.0000}_{-0.0000}$
45 - 50	$1.0000^{+0.0000}_{-0.0000}$	$1.0001^{+0.0000}_{-0.0000}$
50 - 60	$0.9998^{+0.0000}_{-0.0000}$	$1.0000^{+0.0001}_{-0.0001}$
60 - 80	$0.9998^{+0.0001}_{-0.0001}$	$0.9998^{+0.0001}_{-0.0001}$
80 - 100	$0.9995^{+0.0002}_{-0.0002}$	$0.9996^{+0.0003}_{-0.0004}$
100 - inf	$0.9984^{+0.0010}_{-0.0016}$	$0.996^{+0.0017}_{-0.0024}$

Table 7.10: Isolation SF in p_{T}-bins for the Z- and W-working points.

Bibliography

[1] CDF Collaboration Collaboration, A. Abulencia et al., *Measurements of inclusive W and Z cross sections in p anti-p collisions at s**(1/2) = 1.96-TeV*, J.Phys. **G34** (2007) 2457–2544, arXiv:hep-ex/0508029 [hep-ex].

[2] ATLAS Collaboration, H. Samira, P. Chariclia, I. Dimitrios, and B. Konstantinos, *The Tag and Probe method with J/psi and Upsilon candidates in ATLAS, ATL-PHYS-INT-2010-050,*.

[3] ATLAS Collaboration Collaboration, G. Aad et al., *Muon reconstruction efficiency and momentum resolution of the ATLAS experiment in proton-proton collisions at* $\sqrt{s}$*=7 TeV in 2010*, arXiv:1404.4562 [hep-ex].

[4] ATLAS Collaboration, G. Aad et al., *Expected Performance of the ATLAS Experiment - Detector, Trigger and Physics*, arXiv:0901.0512 [hep-ex].

[5] T. Sjostrand, S. Mrenna, and P. Z. Skands, *PYTHIA 6.4 Physics and Manual*, JHEP **0605** (2006) 026, arXiv:hep-ph/0603175 [hep-ph].

[6] M. Smizanska, *PythiaB an interface to Pythia6 dedicated to simulation of beauty events, ATL-COM-PHYS-2003-038,*.

Chapter 8

WZAnalysis

The simultaneous production of the W,Z bosons is studied in this analysis. Only leptonic decays of the bosons are considered and the $W^{\pm}Z$ signature is therefore comprised of three isolated, high-p_{T} leptons accompanied by significant amount of missing transverse energy. There are four distinct final-state topologies (the lepton originating from the W boson decay is mentioned first): $\mu^{\pm}\mu^{+}\mu^{-}$, $e^{\pm}\mu^{+}\mu^{-}$, $\mu^{\pm}e^{+}e^{-}$ and $e^{\pm}e^{+}e^{-}$.

In the following a brief description of the $W^{\pm}Z$ analysis time-line is shown; the goals and the results of the 7 and of the 8 TeV (Moriond analysis) will be presented as well. In this thesis, the latest results from the 8 TeV analysis will be discussed where my contribution was significant and the differences with respect to the Moriond analysis, will be presented. The results of this analysis will appear in a publication which is currently under preparation.

8.1 Time-line of the $W^{\pm}Z$ analysis

8.1.1 7 TeV analysis results

The first measurement, in the context of the ATLAS experiment, of the $W^{\pm}Z$ production cross-section using the full 2011 7 TeV data was delivered by [1] and had focused on the measurement of the fiducial and total cross-sections, the differential cross-section (with respect to p_Z^T, m_{WZ}) and on setting the limits for anomalous Triple Gauge Couplings (aTGCs). The fiducial and total cross-sections were measured to be:

$$\sigma_{WZ}^{fid} = 92^{+7}_{-6}(stat.) \pm 4(syst.) \pm 2(lumi.) \text{ fb}$$

and:

$$\sigma_{WZ}^{tot} = 19.0^{+1.4}_{-1.3}(stat.) \pm 0.9(syst.) \pm 0.4(lumi.) \text{ pb}$$

$$N_{exp} = N_{obs} - N_{bkg} = \sigma_{WZ}^{tot} \times BR_{W\to\ell'\nu,Z\to\ell\ell} \times L \times A_{WZ\to\ell'\nu\ell\ell} \times C_{WZ\to\ell'\nu\ell\ell}$$

respectively, with the total cross-section being consistent with the SM expectation of $17.6^{+1.1}_{-1.0}$ pb. The 95% confidence intervals are $\Delta g_1^Z \in [-0.057, 0.093], \Delta\kappa^Z \in [-0.37, 0.57]$ and $\lambda^Z \in [-0.046, 0.047]$ and they are set without a form factor[1], meaning that the value of Λ has been set to infinity. Figure 8.1 shows the differential cross-section with respect to the Z boson p_{T}, along with the aTGCs limits from the ATLAS, the CDF and the D0 experiments for the 3 aTGCs.

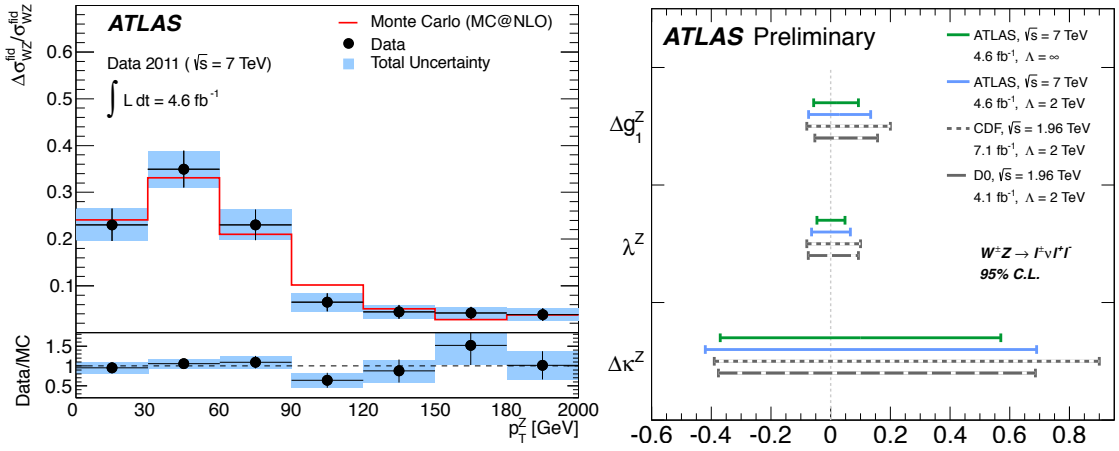

Figure 8.1: Normalised fiducial cross-section $\Delta\sigma_{WZ}^{fid}/\sigma_{WZ}^{fid}$ in bins of p_{T} compared with the SM prediction. The total uncertainty contains statistical and systematic uncertainties added in quadrature (left). 95% confidence intervals for anomalous TGCs from ATLAS, CDF [2] and D0 [3]. Integrated luminosity, centre-of-mass energy and cut-off Λ for each experiment is shown (right).

[1]The form factor is the parameterisation: $a(\hat{s}) = \frac{a_0}{1+\hat{s}/\Lambda^2}$ where a stands for $\Delta g_1^Z, \Delta\kappa^Z, \lambda^Z$, the anomalous couplings with respect to the SM values and Λ is the value of the scale in which New Physics manifests itself.

8.1.2 8 TeV Moriond analysis results

Figure 8.2 summarises the results from the 7 TeV and the first analysis on 8 TeV data that measured the fiducial and total cross-sections using data collected in 2012 corresponding to an integrated luminosity of 13 fb^{-1} [4]. The fiducial and total cross-sections were measured to be:

$$\sigma_{WZ}^{fid} = 99.2^{+2.8}_{-3.0}(stat.)^{+5.1}_{-5.4}(syst.)^{+3.1}_{-3.0}(lumi.) \text{ fb}$$

and:

$$\sigma_{WZ}^{tot} = 20.3^{+0.8}_{-0.7}(stat.)^{+1.2}_{-1.1}(syst.)^{+0.7}_{-0.6}(lumi.) \text{ pb}$$

respectively, a result in excellent agreement with the SM total cross-section expectation of 20.3 $\pm$ 0.8 pb, calculated with fixed renormalisation and factorisation scales of (m_W + m_Z/2). In the following sections the details of the present 8 TeV analysis are given and in particular the event selection details, the optimisation of the muon isolation, the background estimation using the Template Fit method as well as the cross-section measurement.

8.2 Data and simulation samples

8.2.1 Data samples

The full 2012 $\sqrt{s}$ =8 TeV dataset, corresponding to 20.183 fb^{-1} is used in this analysis. The data were collected between April and December 2012 and their corresponding luminosity was estimated with an uncertainty of 2.8%, using the same technique as the one used for all 7 TeV analyses [5]. Events were selected using the Good Run List (GRL) definition: `data12 _8TeV.periodAllYear_DetStatus-v61-pro14-02_DQDefects-00-01-00_PHYS_StandardGRL_All_Good.xml`, based on data quality flags per luminosity block.

In the relevant dataset, two streams are used: `physics_Muons` and `physics_Egamma`. The events are required to have fired the single-muon and single-electron triggers of the analysis, in two schemes, either comprised of a p_{T}-threshold of 24 GeV along with an isolation requirement on the lepton, or with a much higher p_{T}-threshold of 36 (60) GeV for muons (electrons) but no isolation cut imposed. The relevant muon and electron trigger signatures, for the isolated and non-isolated cases, are namely `EF_mu24i_tight`, `EF_mu36_tight`

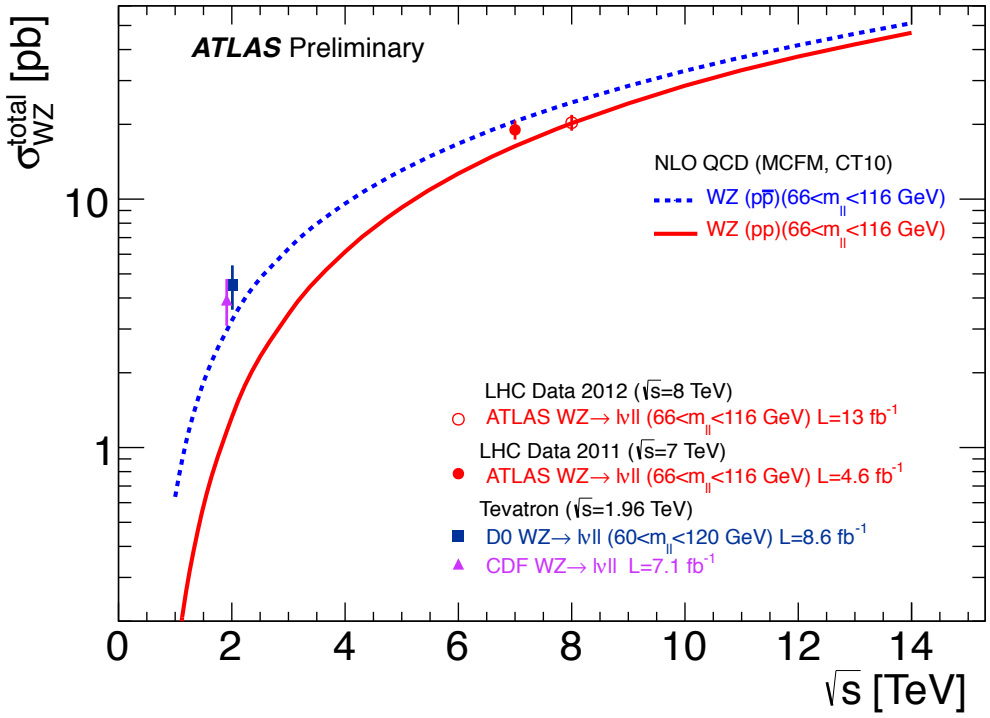

Figure 8.2: Measurements and theoretical predictions of the total $W^{\pm}Z$ production cross-section as a function of the centre-of-mass energy. Experimental measurements from CDF and D0 in proton-antiproton collisions at the Tevatron at $\sqrt{s}$=1.96 TeV and experimental measurements from ATLAS in proton-proton collisions at the LHC at $\sqrt{s}$=7 TeV and $\sqrt{s}$=8 TeV are shown. The blue dashed line shows the theoretical prediction for the $W^{\pm}Z$ production cross-section in proton-antiproton collisions, calculated at NLO using MCFM with PDF set CT10. The solid red line shows the theoretical prediction for the $W^{\pm}Z$ production cross-section in proton-proton collisions, calculated in the same way. The ATLAS results at 8 TeV define the total cross-section with a Z boson with mass between 66 GeV and 116 GeV. The results from CDF define the total cross-section assuming zero-width for the Z boson and neglecting the γ^* contribution. The results from D0 define the total cross-section with a Z boson with mass between 60 GeV and 120 GeV.

and `EF_e24vhi_medium1`, `EF_e60_medium1` respectively. In order to avoid double counting of events, those appearing in both streams are removed from the `Egamma` stream.

The data format used is the `NTUP_SMWZ_D3PD`, which is a *slimmed*[2] version of the original `AOD` files. However, no *skimming*[3] has been imposed on the events. Table 8.1 summarises the details of the data used in this analysis.

Year	2012
Tag	data12_8TeV
Periods	A-L
Streams	physics_Muons, physics_Egamma
Trigger (muon stream)	EF_mu24i_tight, EF_mu36_tight
Trigger (egamma stream)	EF_e24vhi_medium1, EF_mu60_medium1
GRL configuration file	DetStatus-v61-pro14-02_DQDefects-00-01-00
Luminosity (total)	20.28 fb^{-1}

Table 8.1: Summary of the data and the integrated luminosity. Two streams, gathered by the relevant triggers (isolated or not) were used.

8.2.2 MC samples

The full list of the signal and background datasets used in this analysis is presented in detail in Appendix A. For the signal processes `PowhegPythia`, containing all the decays in the four final-state topologies, is used. `Powheg` is a next-to-leading order (NLO) generator interfaced to `Pythia` [6]. The `CT10` parton density function (PDF) set was used, while a generator-level filter requiring same-flavour, opposite-charge lepton pairs to have an invariant mass of $m_{ll} > 5$ GeV was imposed, with at least one of the pairs satisfying $m_{ll} > 30$ GeV.

The backgrounds to the $W^{\pm}Z$ process come from jets associated with the W or the Z gauge bosons (V+jets) and top events ($t\bar{t}$, $t\bar{t}$+V as well as single top). MC@NLO was used in order to model the $t\bar{t}$ and single-top events and Alpgen/Jimmy [7] to model the V+jets background.The di-boson processes $W^{+}W^{-}$, ZZ are modeled with Sherpa and Powheg+Pythia respectively, while $W^{\pm}\gamma$, $Z\gamma$are modeled with Alpgen and Sherpa.

[2] In the *slimming* process, entire data containers within an event are removed (i.e jet containers, calorimeter hits, e.t.c.

[3] *Skimming* is the process in which selection cuts are imposed on the initial set of events, resulting in a reduced set containing fewer events.

8.3 $W^{\pm}Z$ objects selection

A description of the requirements on all the analysis-relevant objects is presented in this section. It includes final-state electrons and muons, missing transverse energy, jets (since MET is built by taking into account all the reconstructed Physics objects) and reconstructed vertices.

8.3.1 Reconstructed vertices

During the 2012 data-taking period, the instantaneous luminosity varied from about $10^{33} cm^{-2} s^{-1}$ to $6.8 \cdot 10^{33} cm^{-2} s^{-1}$. In this environment and taking into account the bunch spacing of 50 ns, the mean number of interactions per bunch-crossing is significantly high (on average 20.7, shown in Figure 8.3).

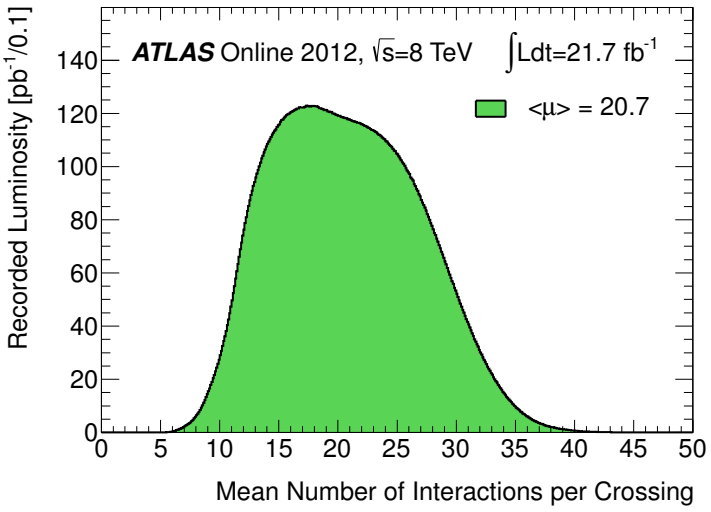

Figure 8.3: Mean number of interactions per bunch-crossing in the 2012 data-taking period, resulting in $< \mu >= 20.7$.

To describe the increased pile-up conditions, the MC samples are re-weighted, in order to reproduce the conditions of the high luminosity and in particular the mean number of interactions per bunch crossing. This is achieved using the ATLAS official tool, `PileUpReweighting-00-02-12` [8]. The $< \mu >$ value in MC is scaled by a factor of $1/1.09$, as described in the recommendations provided in [9], accounting more accurately for the vertex multiplicity observed in the LHC conditions. Finally, the z-coordinate of the primary vertex (the vertex with at least three reconstructed tracks and the largest $\sum p_T^2$) is corrected using

the `VertexPositionReweightingTool` from the `egammaAnalysisUtils` package is used.

8.3.2 Trigger

Events were recorded using single lepton triggers and during the analysis a matching requirement between one of the three leptons and the trigger object (within $\Delta R = \sqrt{\Delta\eta^2 + \Delta\phi^2} < 0.1(0.15)$ for muons (electrons)) is requested. The matched lepton should have p_{T} of at least 25 GeV while scale factors to account for the mis-modelling of the single lepton trigger efficiency in MC are used. The scale factors are derived using the tag-and-probe method.

Scale factors are provided in p_{T} and η for muons, while for electrons in E_{T} and η.

8.3.3 Electrons

Since an electron in the context of the ATLAS experiment is a track in the ID associated to a distinctive shower shape in the CS, a series of selection criteria have to be imposed in order to select solid electrons for Physics analysis. These criteria involve the identification and reconstruction algorithms as well as the conditions of the relevant detectors subsystems and the kinematic demands related to the Physics of the particular analysis. In the $W^{\pm}Z$ analysis, electrons that fulfill the `egamma` *loose++* identification criteria are preselected. Subsequently, the author algorithm is checked; it is required to be 1 or 3 (standard reconstruction algorithm) and then a calorimeter quality check, *OTX/OQ* flag, based on the conditions of the LAr sub-detector at the data-taking period is imposed. At the next step the kinematic criteria of electrons are checked: their p_{T} is required to be greater than 15 GeV and their $|\eta|$ <2.47 (common ID and CS acceptance), imposing on top a veto for the so-called *crack* region[4]. In order to reject electrons coming from other processes and not the $W^{\pm}Z$ production vertex, a cut is applied on the impact parameter significance, $d_0/\sigma_{d_0} < 6.0$, along with a cut on their *unbiased* z-coordinate, $z_0 \cdot sin(\theta) < 0.5$. *Unbiased* refers to the track impact parameters (longitudinal and transverse) that are calculated after the electron track has been removed from the reconstructed primary vertex.

The final part of the selection consists of an isolation requirement (both calorimetric as well as track-based) imposed on all electrons of the analysis. In the calorimetetric

[4]The transition region between the barrel and the end-cap calorimeters where the performance of the CS system is deteriorated.

part of the isolation requirement, the sum of the topological cluster transverse energy, in a cone of ΔR=0.2 around the electron must, be less than 14% of the electron's E_T (where the actual electron E_T has been removed from the sum and p_{T}-leakage and number of primary vertex candidates corrections have been applied). For the track-based part it is required that the sum of the transverse momentum of all tracks of p_{T}>1 GeV, in a cone of ΔR=0.2 around the electron, is less than 13% of the electron p_{T} (again not including the electron itself). Table 8.2 summarises the selection criteria for electrons. Finally, an overlap removal between electrons and muons is performed at the end of the electron selection (more details in subsection Overlap removal).

Electron selection	
Identification	*loose++*
Author	1 || 3
DAQ	*OTX/OQ*
p_{T}	15 GeV
η	$\|\eta\|$ <2.47 (no crack)
$z_0 \cdot sin(\theta)$	< 0.5
d_0/σ_{d_0}	< 6.0
$\sum_{\Delta R<0.2} E_T(i)$	$< 0.14 \cdot E_T$
$\sum_{\Delta R<0.2} p_T(i)$	$< 0.13 \cdot p_T$

Table 8.2: Electron selection criteria.

A residual energy scale calibration is applied in data [10], using the official ATLAS tool, provided by the `egamma` performance group: `EnergyRescalerTool`. In order to match the resolution observed for electrons in W and Z events in 2012 data, the electron energies in MC are smeared with the same tool, keeping their direction fixed.

8.3.4 Muons

Muons selection starts with all the muons reconstructed by the `STACO` algorithm, with loose identification criteria, belonging to the Combined or ST families. A p_{T} cut of 15 GeV is imposed along with a pseudo-rapidity requirement of $|\eta|$ <2.5. Track quality cuts, as suggested by the Muon Combined Performance [11] (`MCP`) group are applied. These include at least 1 hit in the Pixel detector and at least 5 hits in the SCT, where the number of crossed dead sensors has been taken into consideration and less than 3 holes are demanded as well. The last `MCP` track quality cut is an η-dependent condition on the TRT hits and outliers where for the 0.1< $|\eta|$ <1.9 region $N_{hits}+N_{outliers} > 5$ and $N_{outliers}/(N_{outliers}+N_{hits}) < 0.9$

must be satisfied. The muon impact parameter significance is checked in order to ensure primary vertex muons by asking for $d_0/\sigma_{d_0} < 3.0$. In the same spirit, the *unbiased* z-coordinate has to be less than 0.5, $z_0 \cdot sin(\theta) < 0.5$. *Unbiased* refers to the track impact parameters (longitudinal and transverse) that are calculated after the muon track has been removed from the reconstructed primary vertex.

An isolation requirement, to reject secondary muons from hadronic jets, is applied on muons and it consists only of a track-based part defined as the sum of p_{T} inside a cone of ΔR =0.2 around the muon. This has to be less than 15% of the muon p_{T}, where in the sum the muon p_{T} has not been taken into account. Table 8.3 summarises the selection criteria for muons, along with their corresponding efficiency, each one calculated with respect to the previous step. In the MC simulation, the momenta of the muons are smeared, keeping their direction fixed, as suggested by the `MCP` group.

Muon selection

Algorithm	STACO (loose)	Relative efficiency (%)
Family	Combined || ST	91.47
p_{T}	15 GeV	74.47
MCP	Track quality (see text)	99.56
η	$\|\eta\|$ <2.5	99.91
$z_0 \cdot sin(\theta)$	< 0.5	96.15
d_0/σ_{d_0}	< 3.0	80.88
$\sum_{\Delta R<0.2} p_T(i)$	$< 0.15 \cdot p_T$	86.68

Table 8.3: Muon selection criteria.

8.3.5 Jets

Jets selection is focused on their kinematics and quality properties. Their p_{T} is required to be > 30 GeV and to be within $|\eta|$ <4.5. For their reconstruction the anti-$k_{\perp}$ algorithm is used and their energy is calibrated using the Local Hadronic calibration method (LCTopo). Jets satisfying the above criteria must have $JVF < 0.5$ (if they stand within $|\eta|$ <2.4), with JVF being the jet vertex fraction, i.e the probability that a jet came from a primary vertex, described in [12]. All jets are tested for the *looserBad*[5] criterion, which is a series of cuts that probe the most common sources of spurious or out-of-time energy deposits in the calorimeters. Finally, a jet must be separated from selected leptons by at

[5]https://twiki.cern.ch/twiki/bin/view/AtlasProtected/HowToCleanJets

least ΔR =0.3, as suggested by the `JetMET` group [13].

8.3.6 Missing transverse energy

The transverse momentum imbalance in the ATLAS detector defines the missing transverse energy, `MET_RefFinal`, which is build by all the Physics objects: electrons, muons, taus, photons and jets, along with calorimeter soft-terms (non-associated to the aforementioned Physics objects calorimeter cells, calculated from topological clusters that include noise suppression). In events with a large number of pile-up interactions the performance of `MET_RefFinal` deteriorates. For this reason, a flavour of MET with both *JVF* and *STVF* pile-up suppression is used, namely `MET_RefFinal_STVF` [14].

8.3.7 Overlap removal

During the process of reconstruction, an object may be duplicated by reconstruction algorithms in two distinct regions of the ATLAS detector. In order to avoid using twice the same object, an overlap removal process is used, where the $\eta - \phi$ separation is checked. Three types of overlap removal are considered:

1. μ-e: An electron is removed as fake and the muon is kept if they overlap in ΔR <=0.1;
2. μ-jet: A jet is removed if it is closer than 0.3 in ΔR to a muon and the muon is kept;
3. e-jet: A jet is removed if it is closer than 0.3 in ΔR to an electron and the electron is kept;

8.4 Muon isolation study

The association of muons to Z-boson decays is generally "safer" than the corresponding one to W-boson decays, since the Z-boson has a rather clear experimental signature, but also because of the ambiguity the MET introduces, since we are able to reconstruct the neutrino only partially. For these reasons, the selection criteria imposed on the muons that are associated to W decays are stricter than the ones imposed on the muons associated to Z decays.

The isolation cut, being an important part of the $W^{\pm}Z$ analysis in order to discriminate prompt muons (coming from W or Z decays), from muons that are produced

in the quark fragmentation and hadronisation process (and are therefore constituents of a jet). In this section the impact of the isolation cut imposed on the muons coming from W and Z bosons (track-based alone and in combination with calorimetric) is studied upon the yields of the expected MC, the total background and the signal-to-background ratio (S/B), by performing the following two studies:

1. By applying simultaneously track-based isolation $\sum_{\Delta R<0.3} p_{\mathrm{T}}^{i}/p_{\mathrm{T}}^{\ell}$ to the W muon along with track-based isolation $\sum_{\Delta R<0.2} p_{\mathrm{T}}^{i}/p_{\mathrm{T}}^{\ell}$ to the Z muons. The values of isolation imposed varied for the $W(Z)$ muon(s) in the range from 0.15 (0.14) to 0.10 (0.10). Also studied is the effect of imposing calorimetric isolation of $\sum_{DeltaR<0.3} E_t^i/E_t^{\ell}$ on the W muon on top of it's track-based isolation, along with calorimetric isolation of $\sum_{DeltaR<0.2} E_t^i/E_t^{\ell}$ to the Z muons, on top of their track-based isolation.

2. In the second study, the track-based isolation is applied to the W muon alone at the first step and then the effect of applying calorimetric isolation on top of the track-based isolation of the W muon is investigated. For the Z muons in this study, only track-based isolation is applied, by requiring: $\sum_{\Delta R<0.2} p_{\mathrm{T}}^{i}/p_{\mathrm{T}}^{\ell} < 0.15$.

The default values (baseline) of track-based isolation for W and Z muons are $\sum_{\Delta R<0.3} p_{\mathrm{T}}^{i}/p_{\mathrm{T}}^{\ell} < 0.15$ and $\sum_{\Delta R<0.2} p_{\mathrm{T}}^{i}/p_{\mathrm{T}}^{\ell} < 0.15$ respectively. No calorimetric isolation is required in the case where the W and/or the Z bosons decay to muons. In the following this default selection will be referred to as the Nominal analysis. Also, the relative signal efficiency (the percentage of the signal retained) along with the background rejection (the percentage of the background the isolation scheme will reject) will be given for each one of the studies.

8.4.1 Isolation applied to W and Z muons

In this section, the isolation requirements are applied on both the W and Zmuons. The MC expected signal is calculated, along with the total background and the S/B ratio for the two following isolation schemes:

- Track-based isolation only with the following requirements:
  - W muon: $\sum_{\Delta R<0.3} p_{\mathrm{T}}^{i}/p_{\mathrm{T}}^{\ell} < 0.10$ - 0.14
  - Z muons: $\sum_{\Delta R<0.2} p_{\mathrm{T}}^{i}/p_{\mathrm{T}}^{\ell} < 0.10$ - 0.14

- Calorimetric isolation, on top of the baseline track-based isolation, defined by:
  - W muon: $\sum_{DeltaR<0.3} E_t^i/E_t^\ell <$ 0.10 - 0.14
  - Z muons: $\sum_{DeltaR<0.2} E_t^i/E_t^\ell <$ 0.10 - 0.14

Track-based isolation only

Starting with the Nominal analysis, the isolation value is varied in the range 0.15 - 0.10 and the S/B is calculated. Tables 8.4, 8.5, 8.6, 8.7, 8.8, and 8.9 have the observed data 2012 events and the yields for the MC prediction and the total background estimation, along with the S/B ratio, in the range of the track-based isolation values applied. The errors on the yields are statistical only, with error propagation has been used for the estimation of the error on the S/B ratio. Figure 8.4 shows, for the three topologies of interest, the signal efficiency and the background rejection for the range of the isolation requirement applied.

Source	eem	mme	mmm
Observed	438 ± 20.93	454 ± 21.31	569 ± 23.85
Expected MC	301.9 ± 17.38	310.06 ± 17.61	439.09 ± 20.95
Background	48.24 ± 6.95	102.46 ± 10.12	65.56 ± 8.1
S/B	6.26 ± 0.97	3.03 ± 0.35	6.7 ± 0.89

Table 8.4: Track isolation 0.15. The uncertainties quoted are statistical only.

Source	eem	mme	mmm
Observed	437 ± 20.90	453 ± 21.28	563 ± 23.73
Expected MC	301.66 ± 17.37	309.77 ± 17.60	437.85 ± 20.92
Background	48.12 ± 6.94	102.39 ± 10.12	59.18 ± 7.69
S/B	6.27 ± 0.36	3.03 ± 0.17	7.4 ± 0.35

Table 8.5: Track isolation 0.14. The uncertainties quoted are statistical only.

Source	eem	mme	mmm
Observed	433 ± 20.81	452 ± 21.26	560 ± 23.66
Expected MC	301.3 ± 17.36	309.51 ± 17.59	436.27 ± 20.89
Background	47.73 ± 6.91	102.06 ± 10.10	57.87 ± 7.61
S/B	6.31 ± 0.36	3.03 ± 0.17	7.54 ± 0.36

Table 8.6: Track isolation 0.13. The uncertainties quoted are statistical only.

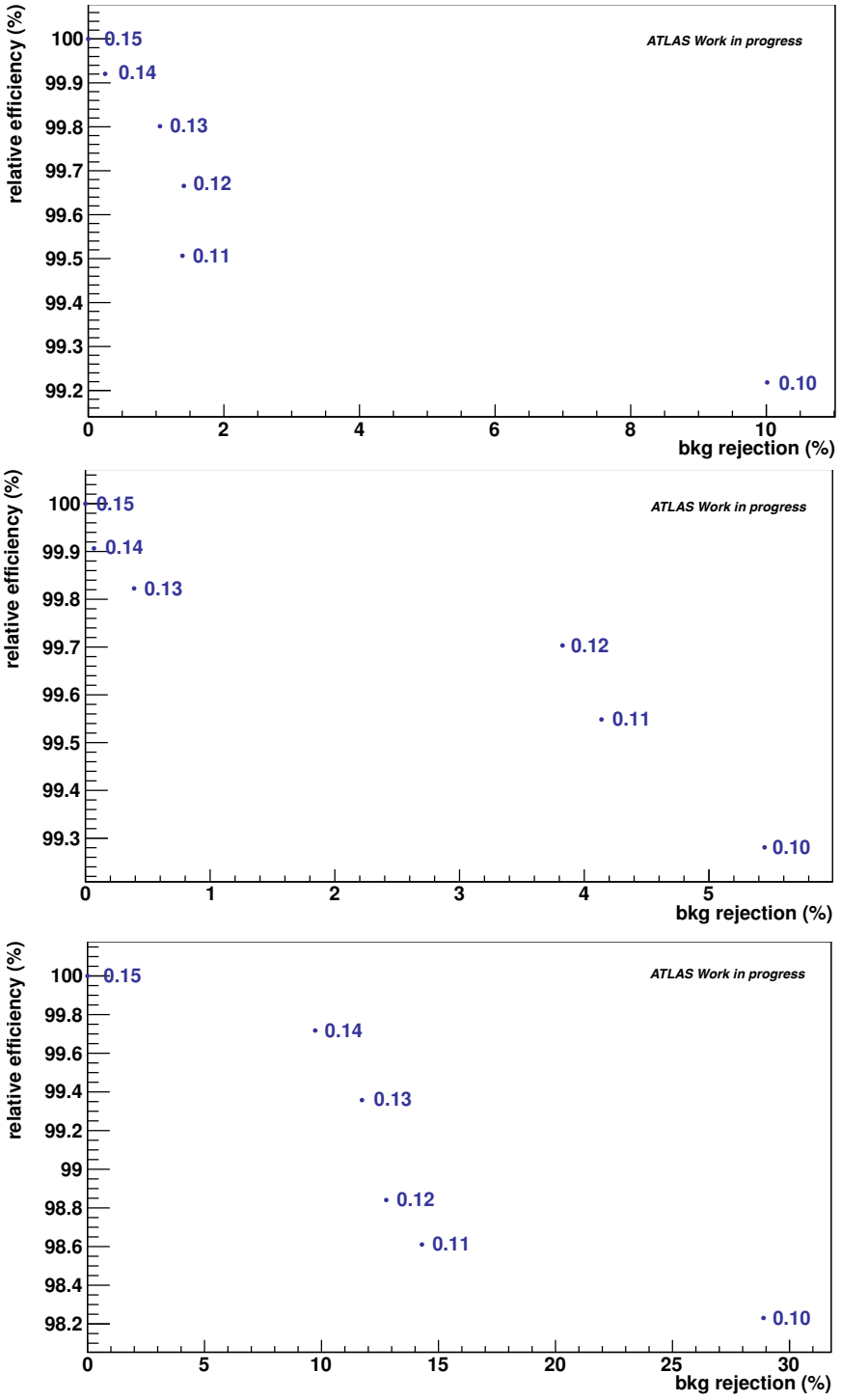

Figure 8.4: The signal efficiency and background rejection percentages for the track-based isolation values applied in the $\mu^{\pm}e^{+}e^{-}$ (top), $e^{\pm}\mu^{+}\mu^{-}$ (middle) and $\mu^{\pm}\mu^{+}\mu^{-}$ (bottom) topologies of interest.

Source	eem	mme	mmm
Observed	431 ± 20.76	451 ± 21.24	553 ± 23.52
Expected MC	300.89 ± 17.35	309.14 ± 17.58	434.00 ± 20.83
Background	47.56 ± 6.90	98.54 ± 9.93	57.19 ± 7.56
S/B	6.33 ± 0.36	3.14 ± 0.18	7.6 ± 0.36

Table 8.7: Track isolation 0.12. The uncertainties quoted are statistical only.

Source	eem	mme	mmm
Observed	425 ± 20.62	450 ± 21.21	548 ± 23.41
Expected MC	300.41 ± 17.33	308.66 ± 17.57	432.99 ± 20.81
Background	47.57 ± 6.90	98.22 ± 9.91	56.19 ± 7.50
S/B	6.32 ± 0.36	3.14 ± 0.18	7.71 ± 0.37

Table 8.8: Track isolation 0.11. The uncertainties quoted are statistical only.

Source	eem	mme	mmm
Observed	423 ± 20.57	450 ± 21.21	539 ± 23.22
Expected MC	299.54 ± 17.31	307.83 ± 17.55	431.32 ± 20.77
Background	43.41 ± 6.59	96.88 ± 9.84	46.62 ± 6.83
S/B	6.9 ± 0.40	3.18 ± 0.18	9.25 ± 0.45

Table 8.9: Track isolation 0.10. The uncertainties quoted are statistical only.

Calorimetric isolation on top of track-based isolation

In the second study, starting again from the Nominal analysis the default track-based isolation is imposed and the calorimetric isolation is varied in the range 0.14 - 0.10. Tables 8.5, 8.6, 8.7, 8.8 and 8.9 have the observed data 2012 events and the yields for the MC prediction and the total background estimation, along with the S/B ratio, in the range of the isolation values applied. The errors on the yields are statistical only, while error propagation has been used for the estimation of the error on the S/B ratio. Figure 8.5 shows the signal efficiency and the background rejection percentages for the range of the calorimetric isolation applied.

Source	eem	mme	mmm
Observed	411 ± 20.27	443 ± 21.05	522 ± 22.85
Expected MC	297.91 ± 17.26	307.58 ± 17.54	429.92 ± 20.73
Background	45.93 ± 6.78	99.61 ± 9.98	43.35 ± 6.58
S/B	6.49 ± 0.38	3.09 ± 0.18	9.92 ± 0.48

Table 8.10: Calorimetric isolation 0.14. The uncertainties quoted are statistical only.

Source	eem	mme	mmm
Observed	410 ± 20.25	441 ± 21.00	520 ± 22.80
Expected MC	297.47 ± 17.25	307.22 ± 17.53	428.04 ± 20.69
Background	45.72 ± 6.76	99.38 ± 9.97	42.57 ± 6.52
S/B	6.51 ± 0.37	3.09 ± 0.18	10.06 ± 0.49

Table 8.11: Calorimetric isolation 0.13. The uncertainties quoted are statistical only.

Source	eem	mme	mmm
Observed	407 ± 20.17	441 ± 21.00	516 ± 22.72
Expected MC	296.82 ± 17.23	306.92 ± 17.52	426.57 ± 20.65
Background	42.05 ± 6.48	98.90 ± 9.94	42.23 ± 6.50
S/B	7.06 ± 0.41	3.10 ± 0.18	10.1 ± 0.49

Table 8.12: Calorimetric isolation 0.12. The uncertainties quoted are statistical only.

8.4.2 Isolation on W muon

In this section, starting again from the baseline track-based isolation, the impact on the MC yields for the following three isolation scenarios is studied:

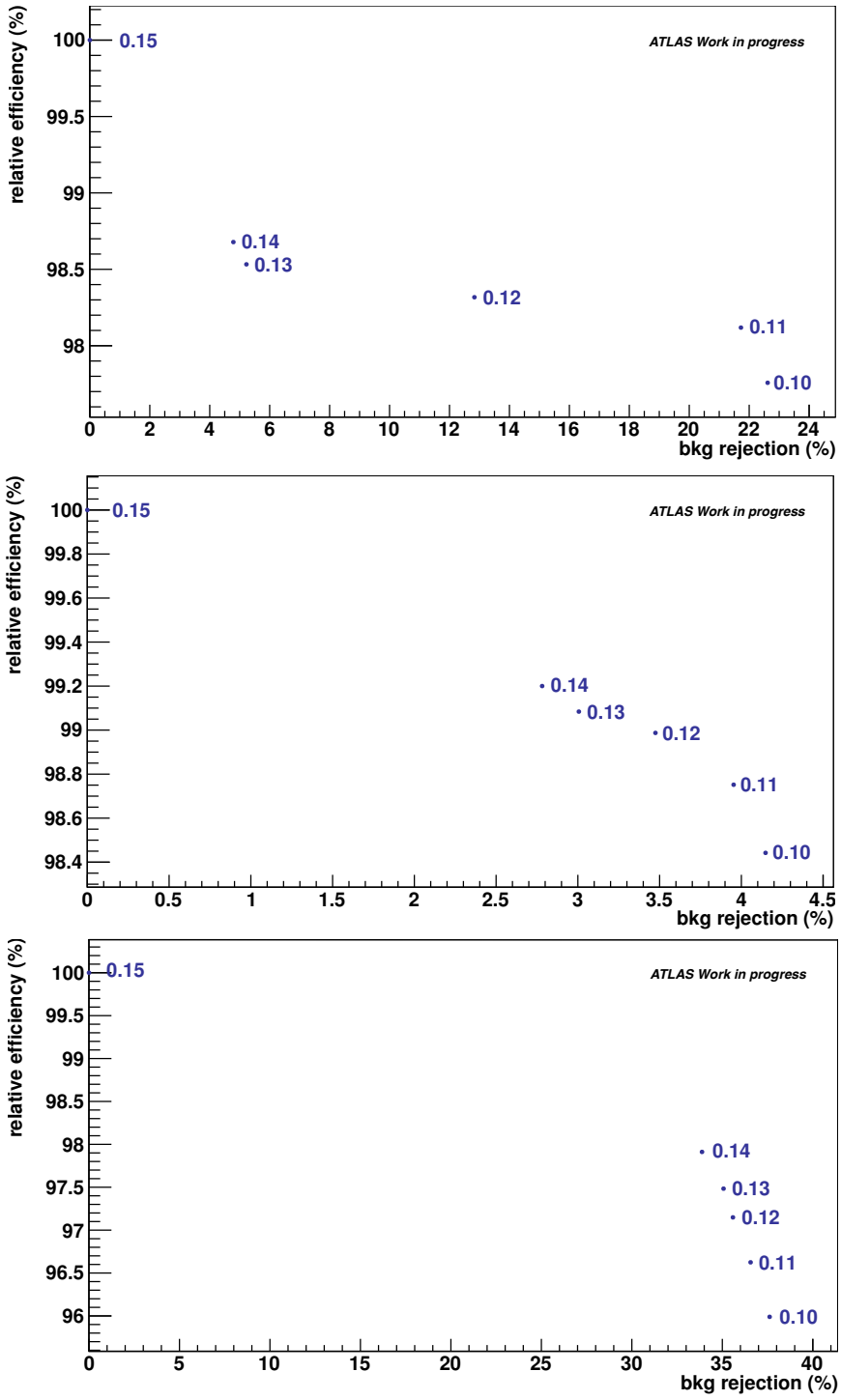

Figure 8.5: The signal efficiency and background rejection percentages for the calorimetric-based isolation values applied in the $\mu^{\pm}e^{+}e^{-}$ (top), $e^{\pm}\mu^{+}\mu^{-}$ (middle) and $\mu^{\pm}\mu^{+}\mu^{-}$ (bottom) topologies of interest.

Source	eem	mme	mmm
Observed	405 ± 20.12	439 ± 20.95	511 ± 22.61
Expected MC	296.22 ± 17.21	306.19 ± 17.50	424.27 ± 20.60
Background	37.76 ± 6.14	98.41 ± 9.92	41.59 ± 6.45
S/B	7.84 ± 0.46	3.11 ± 0.18	10.2 ± 0.50

Table 8.13: Calorimetric isolation 0.11. The uncertainties quoted are statistical only.

Source	eem	mme	mmm
Observed	399 ± 19.97	436 ± 20.88	508 ± 22.54
Expected MC	295.13 ± 17.18	305.23 ± 17.47	421.48 ± 20.53
Background	37.33 ± 6.11	98.21 ± 9.91	40.90 ± 6.40
S/B	7.91 ± 0.46	3.11 ± 0.18	10.31 ± 0.50

Table 8.14: Calorimetric isolation 0.10. The uncertainties quoted are statistical only.

1. Vary the W muon track-based isolation in the range 0.10 - 0.14.

2. Vary the calorimetric isolation in the range 0.10 - 0.15, on top of the default track-based isolation.

3. Apply one of the three combined track-based and calorimetric isolation schemes on W muon, namely:

   - $\sum_{\Delta R<0.3} p_{\mathrm{T}}^{i}/p_{\mathrm{T}}^{\ell} < 0.10$, $\sum_{DeltaR<0.3} E_{t}^{i}/E_{t}^{\ell} < 0.15$
   - $\sum_{\Delta R<0.3} p_{\mathrm{T}}^{i}/p_{\mathrm{T}}^{\ell} < 0.10$, $\sum_{DeltaR<0.3} E_{t}^{i}/E_{t}^{\ell} < 0.12$
   - $\sum_{\Delta R<0.3} p_{\mathrm{T}}^{i}/p_{\mathrm{T}}^{\ell} < 0.10$, $\sum_{DeltaR<0.3} E_{t}^{i}/E_{t}^{\ell} < 0.10$

Track-based isolation

In this isolation scheme the W muon track-based isolation is varied in the range 0.10 - 0.14 while applying $\sum_{\Delta R<0.2} p_{\mathrm{T}}^{i}/p_{\mathrm{T}}^{\ell} < 0.15$ on the Z muons. The signal efficiency and the background rejection factors are visible on Figure 8.6. Tables 8.16, 8.17, 8.18, 8.19 and 8.20 show the yields for the data, the expected MC signal, the total background and finally the S/B ratio. The uncertainties quoted are statistical only and the uncertainty on the S/B ratio was calculated by simple error propagation. Finally, in Figure 8.7 the plots with the number of events for the MC signal, the total background and the S/B ratio are presented.

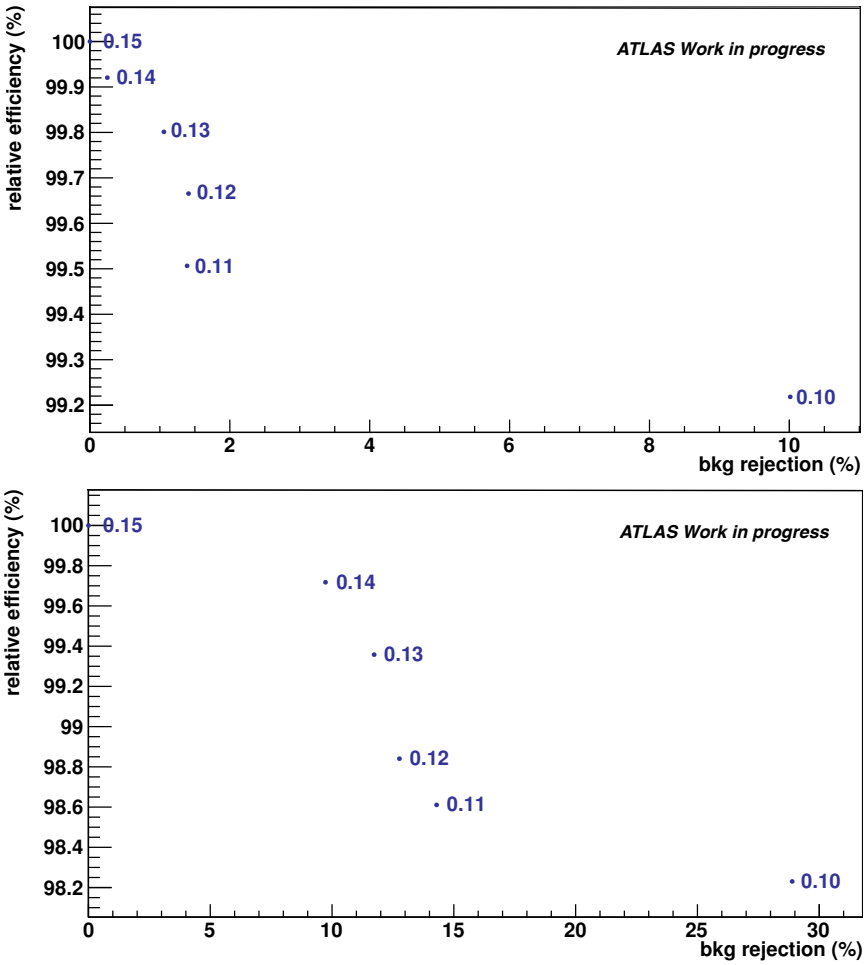

Figure 8.6: The signal efficiency and background rejection percentages for the track-based isolation values applied in the $\mu^{\pm}e^{+}e^{-}$ (top) and $\mu^{\pm}\mu^{+}\mu^{-}$ (bottom) topologies of interest.

Source	eem	mmm
Observed	438 ± 20.93	569 ± 23.85
Expected MC	301.90 ± 17.38	439.09 ± 20.95
Background	48.24 ± 6.95	65.56 ± 8.10
S/B	6.26 ± 0.97	6.70 ± 0.89

Table 8.15: Track isolation 0.15. The uncertainties quoted are statistical only.

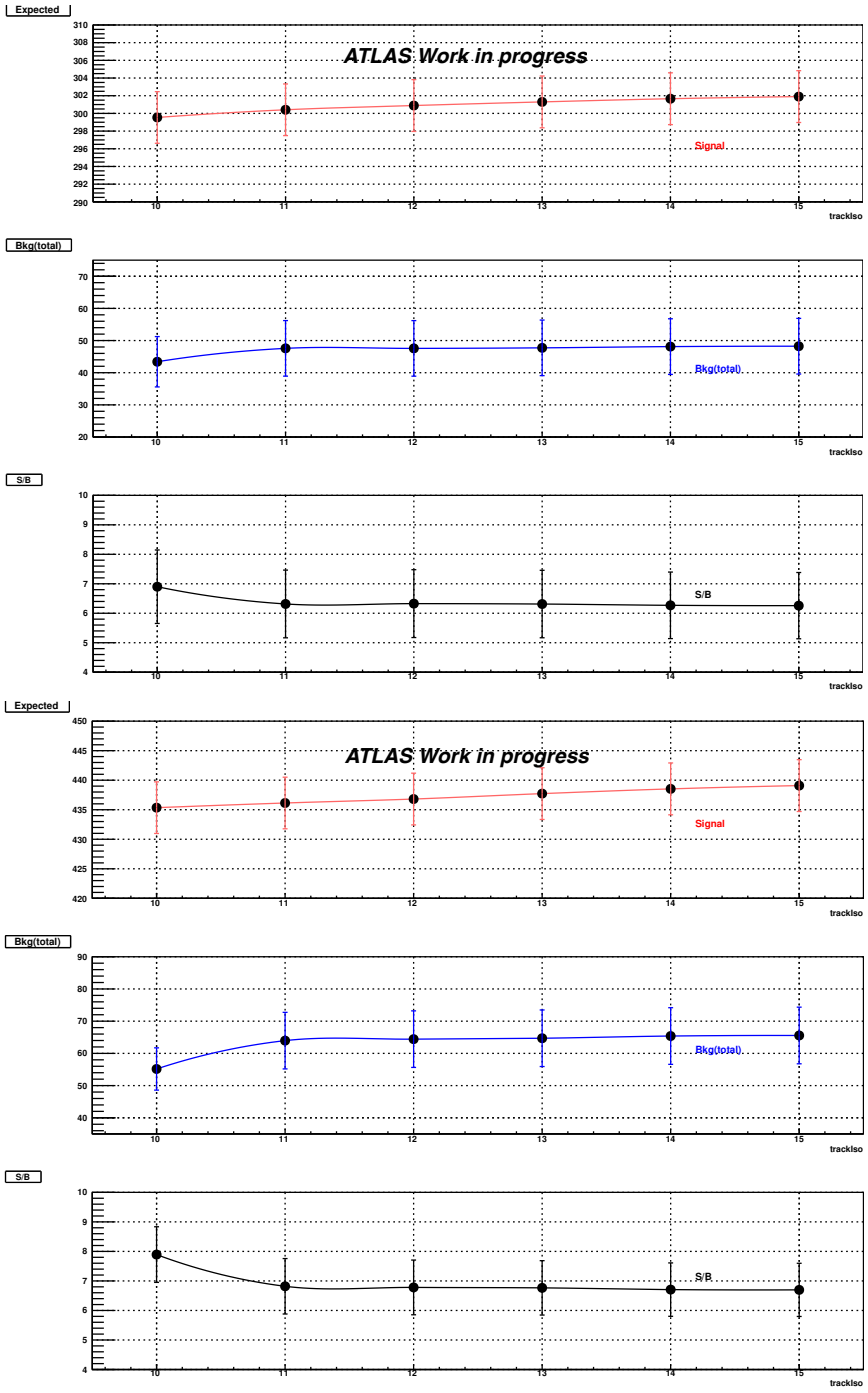

Figure 8.7: The W muon track isolation study results, with the expected events for the MC signal region, the total background and the S/B ratio for the $\mu^{\pm}e^{+}e^{-}$ (top) and $\mu^{\pm}\mu^{+}\mu^{-}$ (bottom) topologies of interest.

Source	eem	mmm
Observed	437 ± 20.90	566 ± 23.79
Expected MC	301.66 ± 17.37	438.53 ± 20.94
Background	48.12 ± 6.94	65.39 ± 8.09
S/B	6.27 ± 0.97	6.71 ± 0.89

Table 8.16: Track isolation 0.14. The uncertainties quoted are statistical only.

Source	eem	mmm
Observed	433 ± 20.81	565 ± 23.77
Expected MC	301.30 ± 17.36	437.73 ± 20.92
Background	47.73 ± 6.91	64.70 ± 8.04
S/B	6.31 ± 0.98	6.77 ± 0.90

Table 8.17: Track isolation 0.13. The uncertainties quoted are statistical only.

Source	eem	mmm
Observed	431 ± 20.76	560 ± 23.66
Expected MC	300.89 ± 17.35	436.81 ± 20.90
Background	47.56 ± 6.90	64.42 ± 8.03
S/B	6.33 ± 0.99	6.78 ± 0.90

Table 8.18: Track isolation 0.12. The uncertainties quoted are statistical only.

Source	eem	mmm
Observed	425 ± 20.62	558 ± 23.62
Expected MC	300.41 ± 17.33	436.14 ± 20.88
Background	47.57 ± 6.90	63.96 ± 8.00
S/B	6.32 ± 0.99	6.82 ± 0.91

Table 8.19: Track isolation 0.11. The uncertainties quoted are statistical only.

Source	eem	mmm
Observed	423 ± 20.57	553 ± 23.52
Expected MC	299.54 ± 17.31	435.33 ± 20.86
Background	43.41 ± 6.59	55.16 ± 7.43
S/B	6.09 ± 0.99	8.89 ± 1.13

Table 8.20: Track isolation 0.10. The uncertainties quoted are statistical only.

Calorimetric isolation on top of track-based isolation

In this isolation scheme the W muon calorimetric isolation is varied in the range 0.10 - 0.15 on top of it's default track-based isolation of $\sum_{\Delta R<0.3} p_{\mathrm{T}}^{i}/p_{\mathrm{T}}^{\ell} < 0.15$, track-based isolation of $\sum_{\Delta R<0.2} p_{\mathrm{T}}^{i}/p_{\mathrm{T}}^{\ell} < 0.15$ is applied on the Z muons. The signal efficiency and the background rejection factors are visible on Figure 8.8. Tables 8.21, 8.22, 8.23, 8.24, 8.25 and 8.26, show the yields for the data, the expected MC signal, the total background and finally the S/B ratio. The uncertainties quoted are statistical only and the uncertainty on the S/B ratio was calculated by error propagation. Finally, in Fig 8.9 the plots with the number of events for the MC signal, the total background and the S/B ratio are presented.

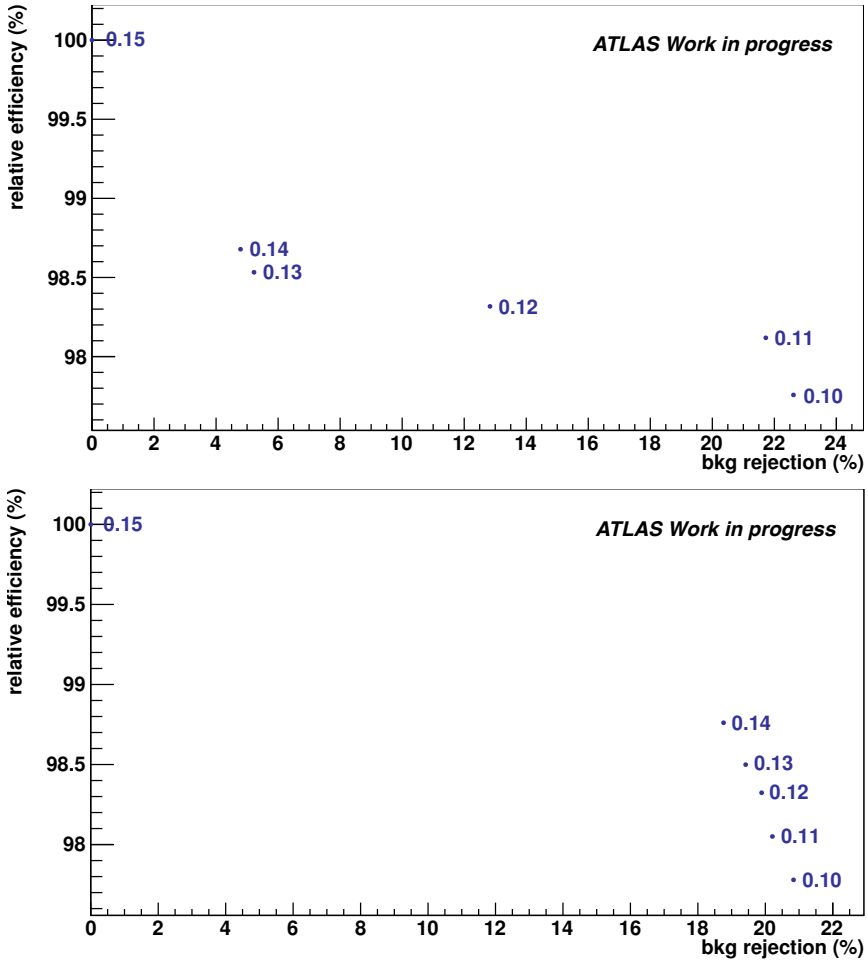

Figure 8.8: The signal efficiency and background rejection percentages for the calorimetric isolation values applied in the $\mu^{\pm}e^{+}e^{-}$ (top) and $\mu^{\pm}\mu^{+}\mu^{-}$ (bottom) topologies of interest.

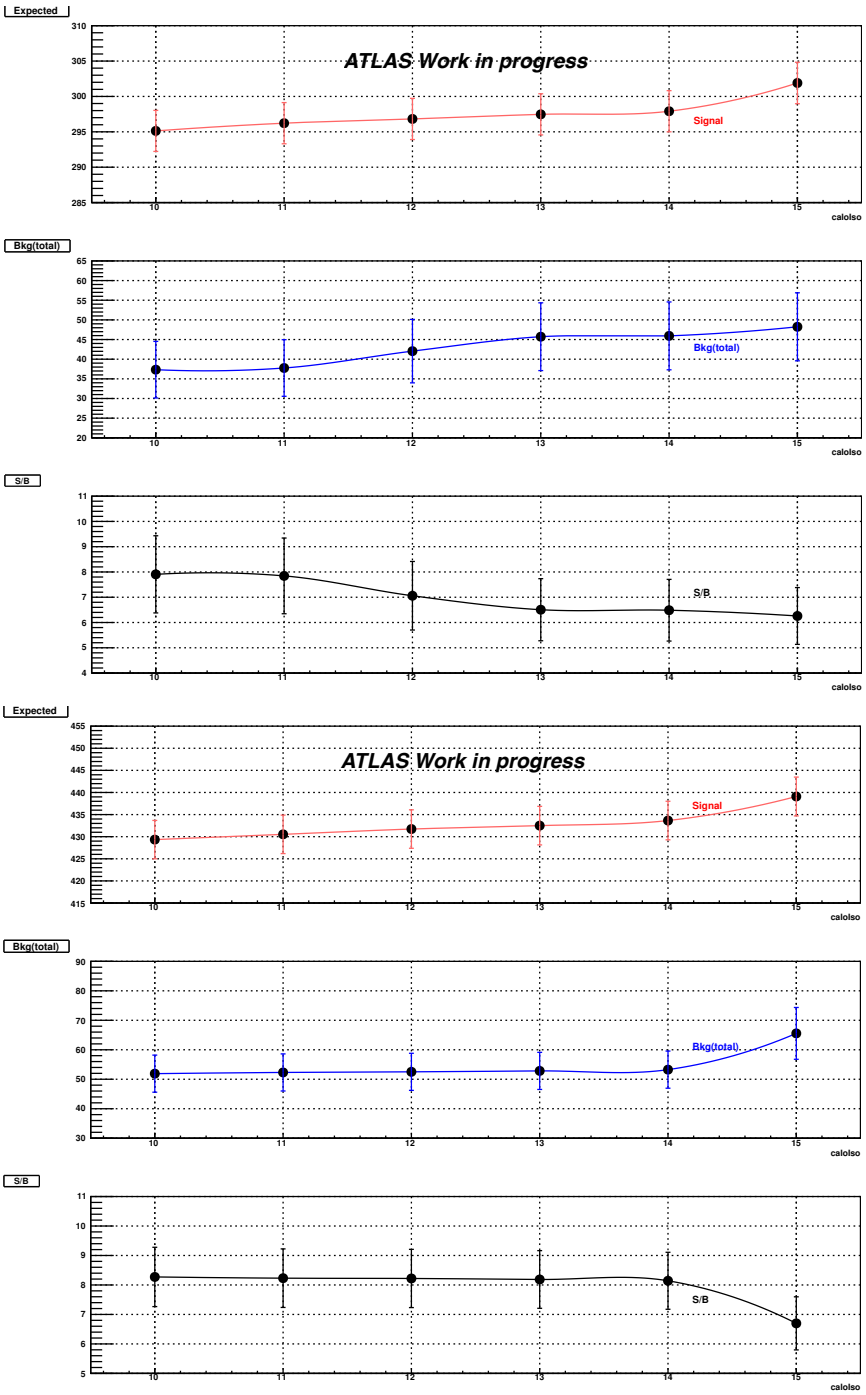

Figure 8.9: The W muon calorimetric isolation study results, with the expected events for the MC signal region, the total background and the S/B ratio for the $\mu^{\pm}e^{+}e^{-}$ (top) and $\mu^{\pm}\mu^{+}\mu^{-}$ (bottom) topologies of interest.

Source	eem	mmm
Observed	411 ± 20.27	537 ± 23.17
Expected MC	301.90 ± 17.38	439.09 ± 20.95
Background	48.24 ± 6.95	65.56 ± 8.10
S/B	6.26 ± 0.97	6.70 ± 0.89

Table 8.21: Calorimetric isolation 0.15. The uncertainties quoted are statistical only.

Source	eem	mmm
Observed	411 ± 20.27	537 ± 23.17
Expected MC	297.91 ± 17.26	433.65 ± 20.82
Background	45.93 ± 6.78	53.26 ± 7.30
S/B	6.49 ± 1.03	8.14 ± 1.18

Table 8.22: Calorimetric isolation 0.14. The uncertainties quoted are statistical only.

Source	eem	mmm
Observed	410 ± 20.25	537 ± 23.17
Expected MC	297.47 ± 17.25	432.5 ± 20.80
Background	45.72 ± 6.76	52.83 ± 7.27
S/B	6.51 ± 1.03	8.19 ± 1.19

Table 8.23: Calorimetric isolation 0.13. The uncertainties quoted are statistical only.

Source	eem	mmm
Observed	407 ± 20.17	536 ± 23.15
Expected MC	296.82 ± 17.23	431.73 ± 20.78
Background	42.06 ± 6.48	52.52 ± 7.25
S/B	7.06 ± 1.15	10.01 ± 1.46

Table 8.24: Calorimetric isolation 0.12. The uncertainties quoted are statistical only.

Source	eem	mmm
Observed	405 ± 20.12	533 ± 23.09
Expected MC	296.22 ± 17.21	430.53 ± 20.75
Background	37.76 ± 6.14	52.31 ± 7.23
S/B	7.84 ± 1.35	8.23 ± 1.21

Table 8.25: Calorimetric isolation 0.11. The uncertainties quoted are statistical only.

Source	eem	mmm
Observed	399 ± 19.97	530 ± 23.02
Expected MC	295.13 ± 17.18	429.34 ± 20.72
Background	37.33 ± 6.11	51.90 ± 7.20
S/B	7.91 ± 1.37	10.31 ± 1.52

Table 8.26: Calorimetric isolation 0.10. The uncertainties quoted are statistical only.

Combined track-based and calorimetric isolation

Finally several distinct combined isolation scenarios are investigated by imposing both track- and calorimetric-based isolation on the W muon. The combinations used are listed on Table 8.27, while the signal efficiency versus the background rejection factors are shown in Figure 8.10. It is evident in both topologies that the only combined isolation scheme retaining more than 99% of the signal, while rejecting more than 10% of the background is the one that track-based isolation of 0.10 and no calorimetric isolation is applied in the W muon.

track	calo	signal eff. $\mu^{\pm}e^{+}e^{-}$	bkg rej. $\mu^{\pm}e^{+}e^{-}$	signal eff. $\mu^{\pm}\mu^{+}\mu^{-}$	bkg rej $\mu^{\pm}\mu^{+}\mu^{-}$
15	-	100	0	100	0
15	15	98.8	4.8	98.9	18.7
10	-	99.2	10	99.2	15.8
10	15	98.1	13	98.1	20.4
10	12	97.6	21	97.6	20.8
10	10	97.1	23	97.1	21.8

Table 8.27: Track- and calorimetric-based combined isolation schemes. The second and third columns give the values of the isolation multiplied by 100. The signal efficiency and background rejection factors are given in columns 4-7.

8.4.3 Conclusions

This study investigated various isolation schemes imposed on muons coming from the decays of the W and Z bosons. Several scenarios of track-based isolation alone or in combination with calorimetric-based isolation, applied to muons coming either from decays of the W-boson alone or applied to all muons, were tested. The isolation scheme that provided the largest background rejection was the one where a combination of track- and calorimetric-based isolation was applied on all muons, rejecting up to ˜37% of background yield in the $\mu^{\pm}\mu^{+}\mu^{-}$ topology.

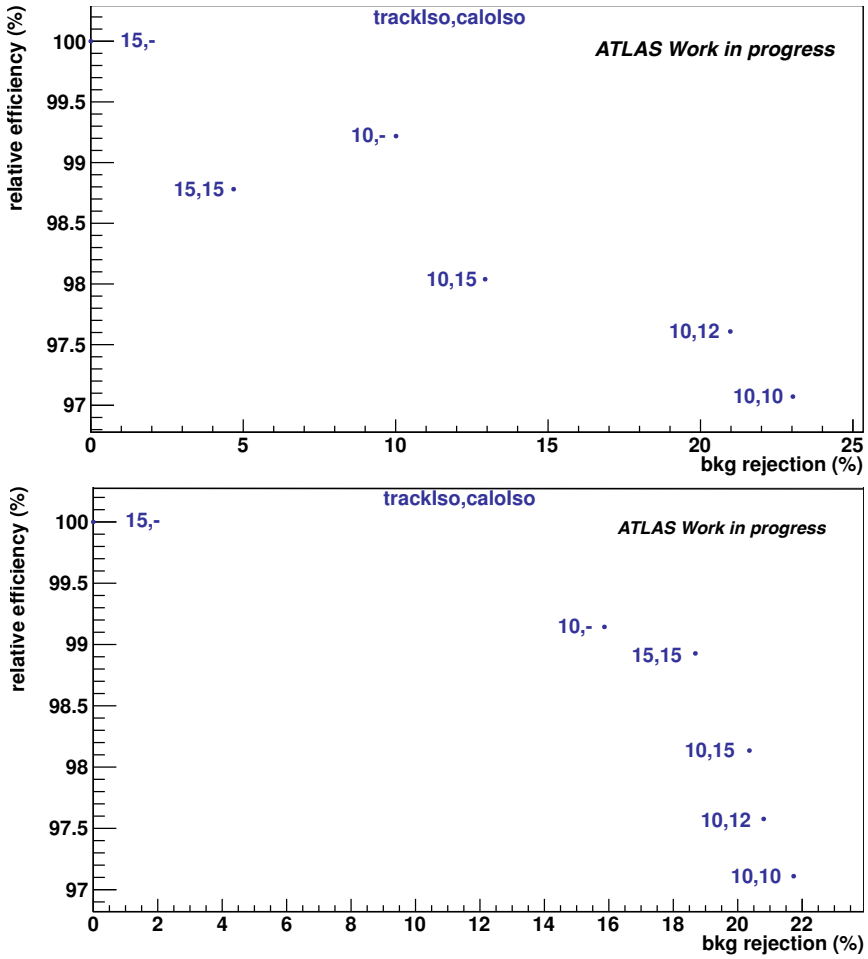

Figure 8.10: The signal efficiency and background rejection percentages for the combined track- and calorimetric-based isolation schemes applied in the $\mu^{\pm}e^{+}e^{-}$ (top) and $\mu^{\pm}\mu^{+}\mu^{-}$ (bottom) topologies of interest.

Nevertheless, since this analysis is mainly a precision measurement of the $W^{\pm}Z$ production cross-section, the signal yield should remain as high as possible. Therefore, the signal efficiency is the main parameter of interest. With this under consideration, the adopted isolation scheme was the one that was retaining most of the signal yield. This isolation scheme is the one where only track-based isolation of 0.1% is applied on the muon coming from the decay of the W-boson, with no calorimetric-based isolation applied on it.

8.5 $W^{\pm}Z$ event selection

The event selection is based on a series of selection cuts, applied on all four final-state topologies: $\mu^{\pm}\mu^{+}\mu^{-}$, $e^{\pm}\mu^{+}\mu^{-}$, $\mu^{\pm}e^{+}e^{-}$, $e^{\pm}e^{+}e^{-}$ indifferently, except for the trigger matching cut. The event selection is as follows:

1. **Good run list:** In the Good Run List (GRL) cut, the events that are part of the GRL [15] list (`data12_8TeV.periodAllYear_DetStatus-v61-pro14-02_DQDefects-00-01-00_PHYS_StandardGRL_All_Good.xml`) are kept. This cut is applied only on data. The luminosity these events correspond to is calculated [16] to be 20.28 fb^{-1}.

2. **Trigger:** Events that have fired the single-electron or single-muon triggers are selected;

3. **Primary vertex:** A good reconstructed primary vertex must be present in order not to discard the event and this is valid when it contains at least three good tracks, following all track-quality suggestions by the MCP group.

4. **MET cleaning:** All the jets with $p_{\mathrm{T}} > 20$ GeV that do not overlap with a selected lepton are tested for the "looser bad" criterion. If at least one jet fails them, the event is discarded, since it is associated with out-of-time energy depositions in the CS and/or noise.

5. **Event cleaning: LAr/Tile noise:** If a noise flag in the LAr or Tile subsystems is raised, the events are removed (applied only in data). The flag for corrupted events (coreFlags&0x40000!=0) is also checked.

6. **ZZ veto:** The total number of selected leptons (electrons plus muons) passing the selections cuts defined in the previous sections is checked. If there are four or more

leptons, over a p_{T}-cut of 7 GeV the event is not considered. This cut efficiently rejects events coming from the ZZ background process.

7. **Z candidate:** At least two opposite-charge, same-flavour leptons forming a candidate of invariant mass in the window $|m_{ll} - 91.1876|$ <10 GeV must be present. In case of more than one combinations satisfying the above criterion, the closest one to the PDG [17] value of the Z boson mass is taken as valid. Electrons forming the candidate must pass the *medium++* quality flag (instead of the *loose++* one used in the preselection).

8. **Three leptons:** Only events with exactly three leptons are considered. The third lepton, associated to the W, must be of the *tight++* quality definition. Also, the p_{T} cut is raised to 20 GeV and the isolation opening cone is ΔR =0.3.

9. **W transverse mass:** A 30 GeV cut on the transverse mass of the reconstructed W boson is applied. The transverse mass of the $\ell\nu$ system is defined by 8.1:

$$M_T^2 = 2E_T^l E_T^\nu - 2\mathbf{p}_T^l \mathbf{p}_T^\nu \tag{8.1}$$

where E_T^l, E_T^ν the transverse energy components and $\mathbf{p}_T^l$, $\mathbf{p}_T^\nu$ the transverse momentum vectors of the lepton and the neutrino.

10. **Trigger matching:** One of the three reconstructed leptons used in the analysis, that is associated with the W or Zdecay and with p_{T} at least 25 GeV must match the online lepton that fired the trigger. In case the EF trigger with the isolation requirement was fired, the track-based isolation of the reconstructed lepton is checked as well.

8.5.1 Kinematic distributions

Figures 8.11, 8.12 and 8.13 present the distributions of several kinematic variables of the reconstructed W and Z bosons. All four reconstructed final-state topologies are included. POWHEG is used for the modelling of the $W^{\pm}Z$ signal expectation while for the several background sources, their MC expectation, normalised to the integrated luminosity of the data, is used.

8.6 Background estimation

In order to measure the $W^{\pm}Z$ fiducial cross-section, an estimation of the number of background events is necessary. The $W^{\pm}Z$ signature consists of three high-p_{T}, isolated

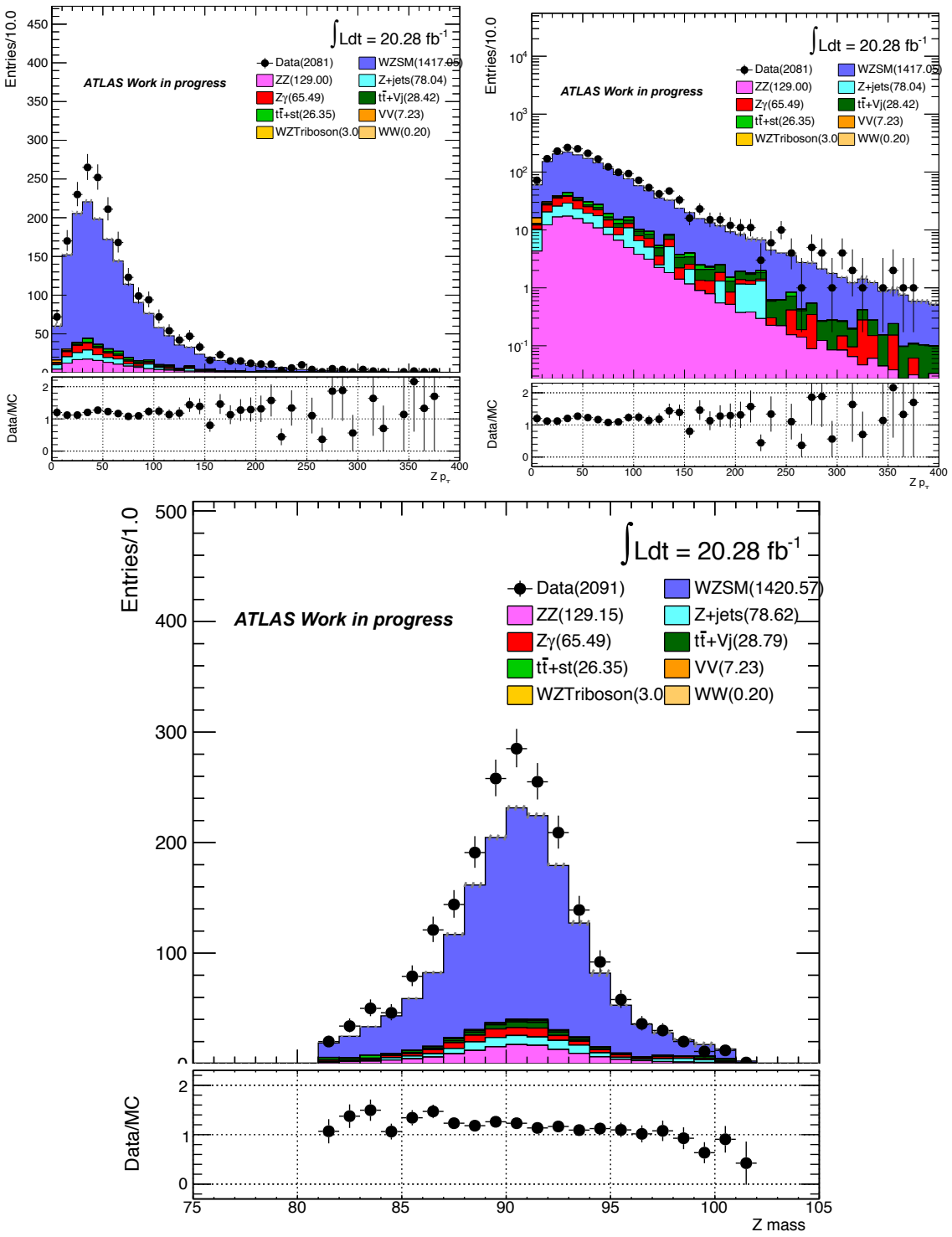

Figure 8.11: Control distributions of the Z-boson: p_{T} (upper left), p_{T} (log, upper right) and invariant mass (bottom). All MC expectations are scaled to the integrated luminosity of the data.

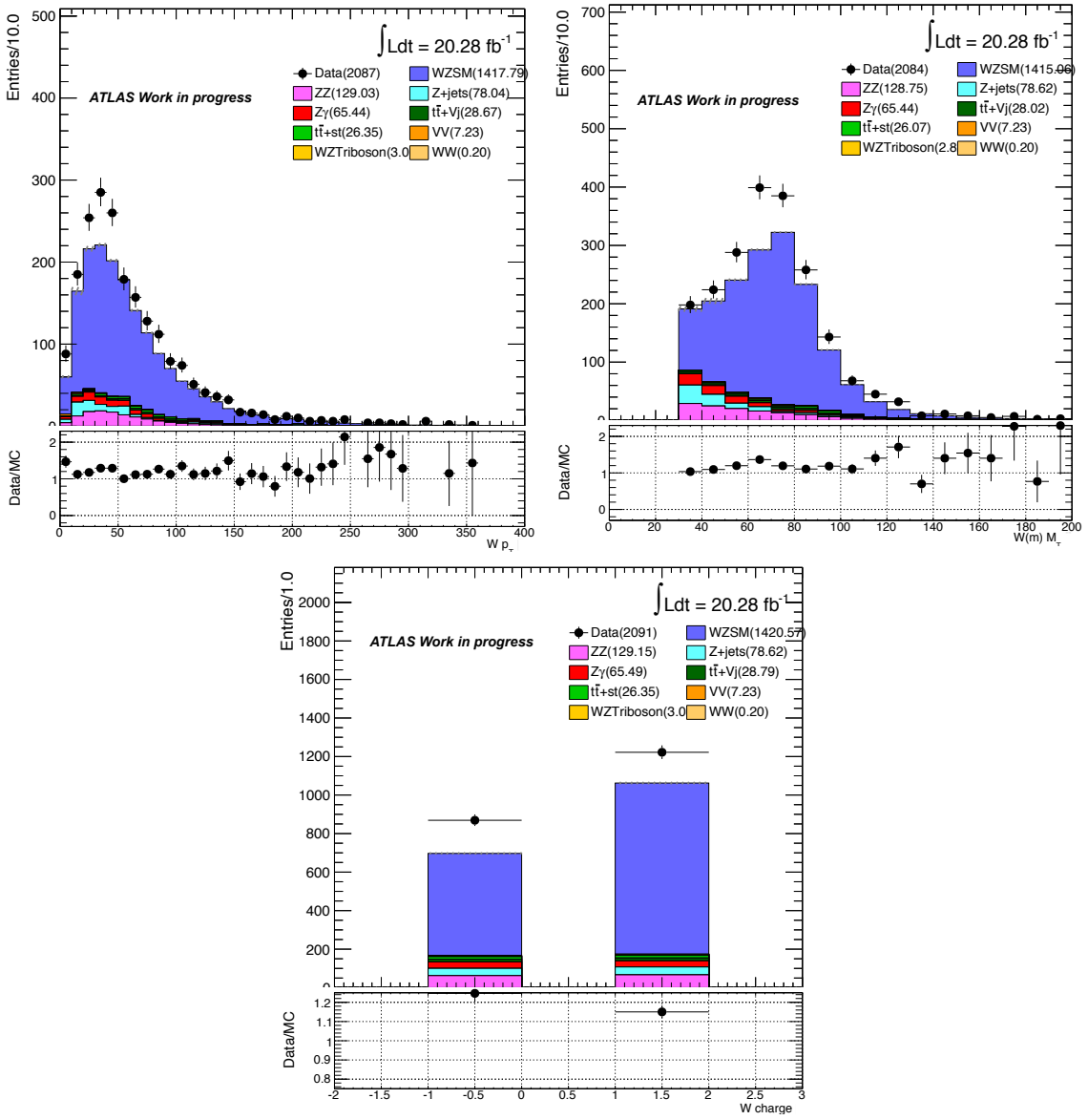

Figure 8.12: Control distributions of the W-boson: p_{T} (upper left), transverse mass (upper right) and charge (bottom). All MC expectations are scaled to the integrated luminosity of the data.

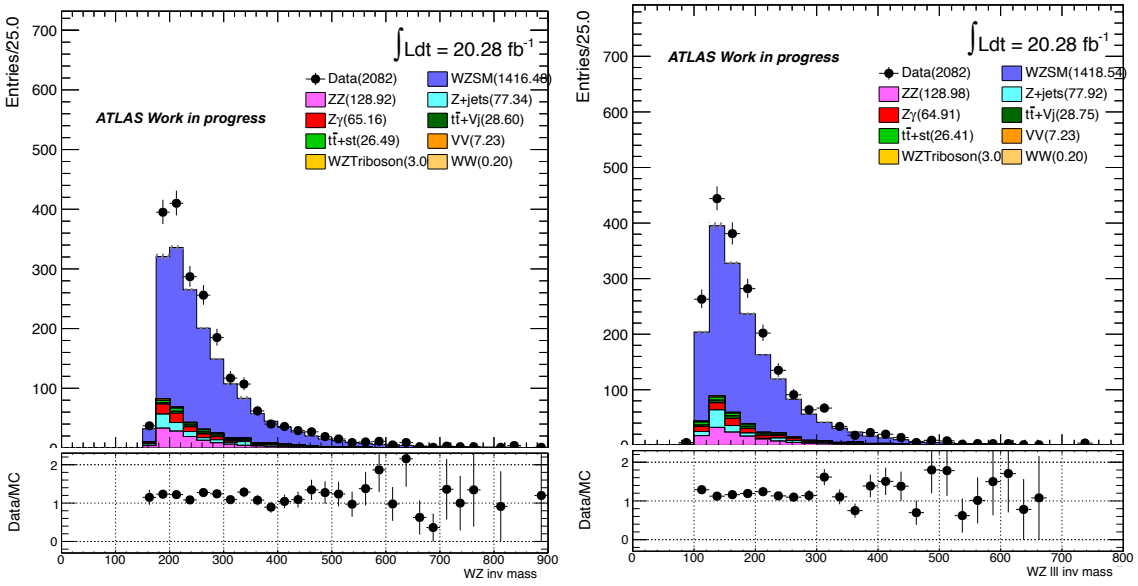

Figure 8.13: Invariant mass of the WZ-system (left) and of the three leptons (right). All MC expectations are scaled to the integrated luminosity of the data.

leptons accompanied by large missing transverse energy. However, several sources can mimic this characteristic signature (listed in order of significance):

- The simultaneous ZZ production, in which one of the leptons escaped detection or it falls outside the detector acceptance. The latter will appear as (potentially significant) missing transverse energy. The three remaining leptons may pass all event selection criteria and thus constitute one of the main background sources.

- A general category with two real leptons coming from Z or W decays and a "fake" lepton. Sources of "fake" leptons are the decays-in-flight of pions and kaons along with heavy-flavor quark decays (b or c). The processes that contribute to this background category are Z+jets, top-quark events ($t\bar{t}$ and single-top) as well as the $Z+\gamma$ process, in which a jet or a photon is misidentified as an electron. These background sources are estimated using a data-driven method.

- The $t\bar{t}$+V process in which, $t\bar{t}$ production is associated with a vector-boson production.

- The simultaneous production of three ElectroWeak (EW) bosons; this background contains the following combinations of simultaneous EW bosons production: ZZZ,

WWW, ZWW, $t\bar{t}WW$ and $WW\gamma$. The total contribution from these sources is very small.

- The Double Parton Scattering (DPS) sources, which include the following processes: W+W, Z/γ^*+ Z/γ^* and W+ Z/γ^*. The contribution from the DPS processes in the total background yield is small.

A data-driven method, namely the Template Fit (TF) method was used in this analysis in order to estimate the background yields of the Z+jets, the $t\bar{t}$, the single-top and the $Z+\gamma$ processes whenever appropriate. The rest of the background sources are estimated taking their MC predictions. In the following section a description of the TF method along with the results on the background yields are given.

8.6.1 Templated Fit method

The Templated Fit [18] method (TF) is based on a binned, maximum-likelihood fit. Selecting an observable, that has sufficient discriminating power between signal and background, a region enriched in background is created. Then the data-driven template is extracted from the aforementioned region. A fit in the signal region is performed using template components that account for contributions from the various processes and that are taken either from data or MC. The method relies on two assumptions: That the total number of events in each template is not too small and that the number of events in each bin is much smaller than the total number of events in each template. In case the aforementioned assumptions are not satisfied then biased fit uncertainties may result.

In this analysis, two template components are used: one collectively accounting for Z+jets, top-quark (single-top and $t\bar{t}$) and $Z+\gamma$ processes and one modelling all the ElectroWeak background processes along with the $W^{\pm}Z$ signal contribution. The first component is estimated using dedicated control samples constructed in data while for the second component the MC predictions, normalised appropriately to the integrated luminosity of the data, are used.

"Fake" leptons (see section 8.6 for their definition) are associated to either W or Z boson decays. Depending on the "fake" lepton flavour and its association to the parent boson (W or Z), the following cases are considered:

1. **"fake" leptons associated to W decays:** Can be either an electron or a muon

leading to the following two categories:

$\mu\mu\mu$, μee: In order to construct the control sample in data the track-based isolation requirement imposed on the muon associated to the W decay is dropped. Furthermore, its d_0 significance cut is reversed so that it satisfies $d_0/\sigma_{d_0} > 3.0$. A common data-driven template is used for the fit in the $\ell\ell + \mu$ cases ($\ell = \mu, e$). Figure 8.14 shows the distribution of the track isolation variable of the muon associated to the decay of the W-boson in the range $[0.0, 0.5]$ in data and the comparison with the MC predictions. It is evident that this control sample is dominated by Z+jets and top-quark processes. The starting values for the fractions of the data-driven and EW components are taken from MC. The fit is then performed and the background contribution is estimated by integrating in the range $[0.0, 0.1]$ (since this is the value of the track-based isolation cut imposed in the analysis). Figure 8.15 shows the fit results for the $\mu\mu\mu$ and μee cases while Table 8.28 depicts the estimated background yields in this case. The χ^2/NDF values for the $\mu\mu\mu$ and μee cases are 1.49 and 1.46 respectively.

Topology	$\mu\mu\mu$	μee	Total
Background Events	$38.0 \pm 3.5 \pm 2.8$	$25.5 \pm 2.3 \pm 5.4$	$63.5 \pm 4.2 \pm 6.1$

Table 8.28: Background estimation fit results for each topology in the W-muon case.

The systematics of the method considered in this analysis include the fit range and the bin size. The default fit range $[0.0, 0.5]$ is varied by $\pm 20\%$, while the default bin size of 0.02 is variated to 0.01 and 0.05 and the measurements are repeated. The largest deviation from the nominal values is taken as the uncertainty of each source and the total systematic uncertainty is their quadratic sum.

$e\mu\mu$, eee: In this case the control sample is constructed by dropping the isolation requirement on the electron and by requiring it to fail the `tight++` identification requirement. Again, a common template is used for the fit, accounting for the $\ell\ell + e$ topologies. Figure 8.16 shows the distribution of the track isolation variable in the range $[0.0, 0.5]$. In this case the control region is dominated by Z+jets and $Z+\gamma$ processes. Figure 8.17 shows the fit results for the eee and $e\mu\mu$ topologies and in Table 8.29 the estimated background yields are listed. The χ^2/NDF values for the eee and $e\mu\mu$ cases are 1.21 and 0.91 respectively. Finally, the same systematic uncertainties

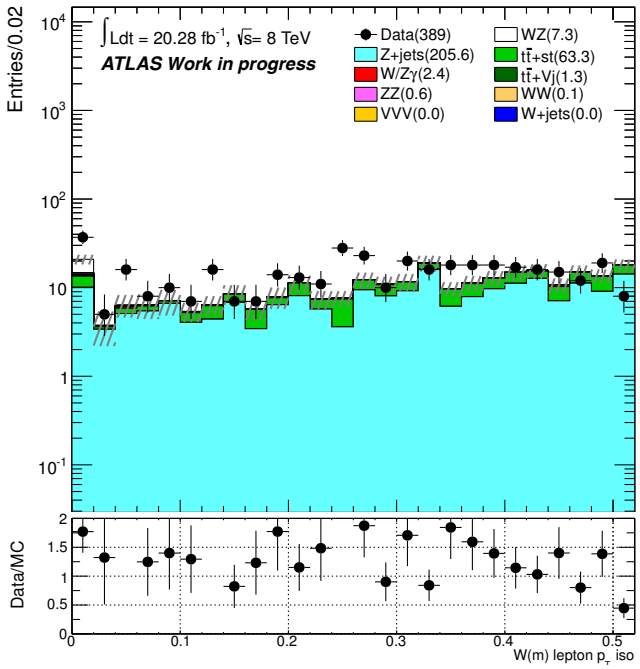

Figure 8.14: Isolation variable template constructed from the dedicated control region in data in the case where the "fake" lepton is a muon associated to W decays. The control region is dominated by the Z+jets and top-quark processes.

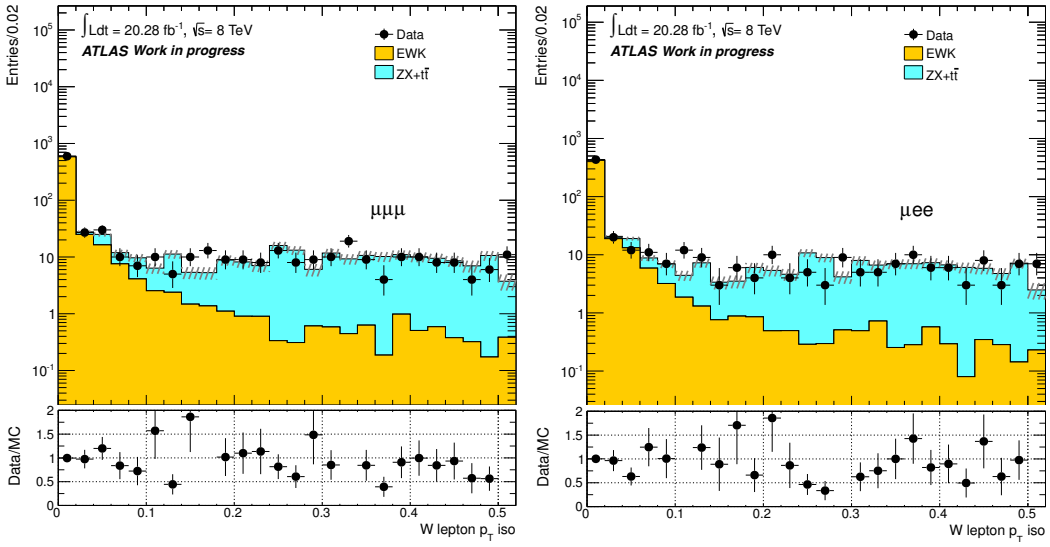

Figure 8.15: The simultaneous fit result (on the isolation of the W-muon) for the $\mu\mu\mu$ (left) and μee (right) topologies.

are considered here as in the previous case.

Topology	$e\mu\mu$	eee	Total
Bakgr. Events	$66.3 \pm 4.9 \pm 0.8$	$42.8 \pm 3.9 \pm 1.7$	$109.1 \pm 6.3 \pm 1.9$

Table 8.29: Background estimation fit results for each topology in the W-electron case.

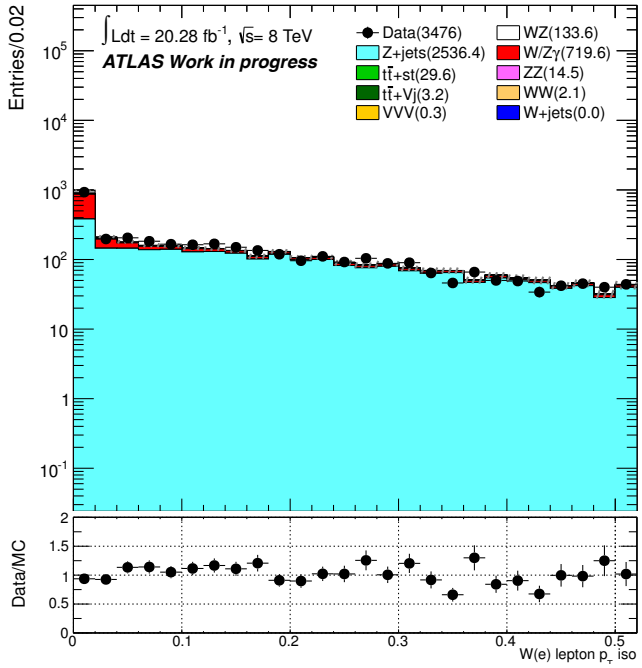

Figure 8.16: Isolation variable template constructed from the dedicated control region in data in the case where the "fake" lepton is an electron associated to W decays. The control region is dominated by the Z+jets and Z/γ processes.

2. **"fake" leptons associated to Z decays:** In this case, a good Z-candidate is not found (as defined by the analysis selection criteria), leading to the absense of a signal event. Similarly to the W-decays, the "fake" lepton can be either an electron or a muon and it may be associated to any of the two leptons of the Z-decay. The construction of the relevant dedicated control samples in data is done by dropping the lepton isolation cut and by reverting the (a) d_0 significance cut, in case of a "fake" muon or (b) by requiring any of the electrons to fail the `tight++` identification requirement. In case that both of the decay leptons satisfy these criteria, one of them is selected in random. The variable to fit in this case is the mass of the Z candidate.

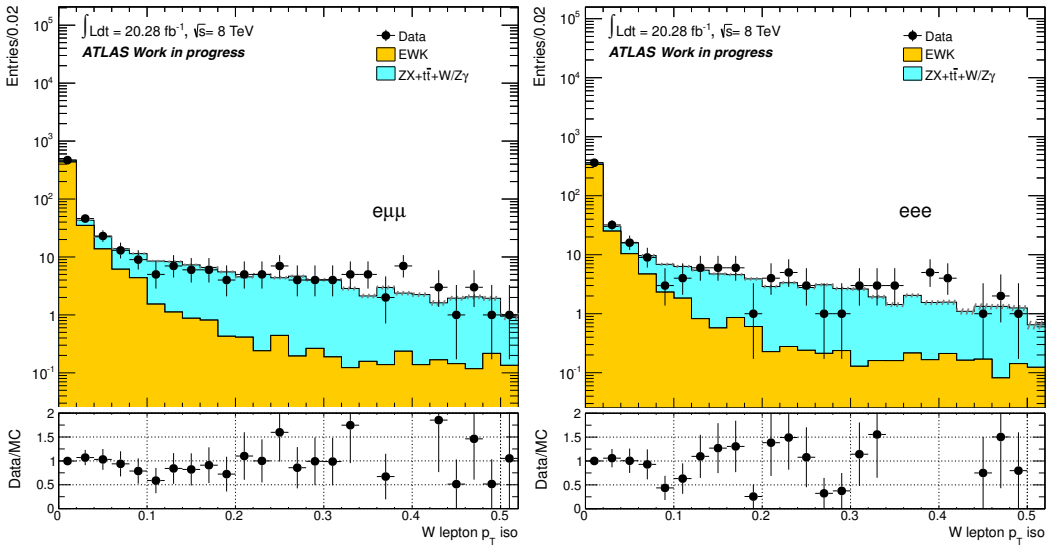

Figure 8.17: The simultaneous fit result (on the isolation of the W-electron) for the $e\mu\mu$ (left) and eee (right) topologies.

The sources of systematic uncertainty are the fit range, the bin size and the choice of the Z candidate. For the fit range, the default range $[41, 141]$ is varied by $\pm$ 10 GeV and three measurements in the regions $[41, 131]$, $[51, 141]$ and $[51, 131]$ are taken. The bin size (default: 2 GeV) is halved and doubled and finally the uncertainty due to the random choice of the Z candidate is estimated by using a template where the candidate chosen is the one closer to the Z `PDG` mass. In each case the maximum deviation from the nominal values is taken as the uncertainty and the total systematic is given by the quadratic sum of all sources. Figure 8.18 shows the results of the fits to data while the total yields estimated for the "fake" leptons associated to the Z-decays are shown in Table 8.30.

Topology	$\mu\mu\mu$	$e\mu\mu$	μee	eee	Total
Bakgr. Events	$8.6 \pm 1.3 \pm 2.3$	$8.0 \pm 1.9 \pm 2.2$	$8.7 \pm 2.1 \pm 2.9$	$11.6 \pm 1.5 \pm 2.5$	$36.9 \pm 3.5 \pm 5.0$

Table 8.30: Background estimation fit results for each topology in the case where the "fake" lepton is associated to the Z-decay.

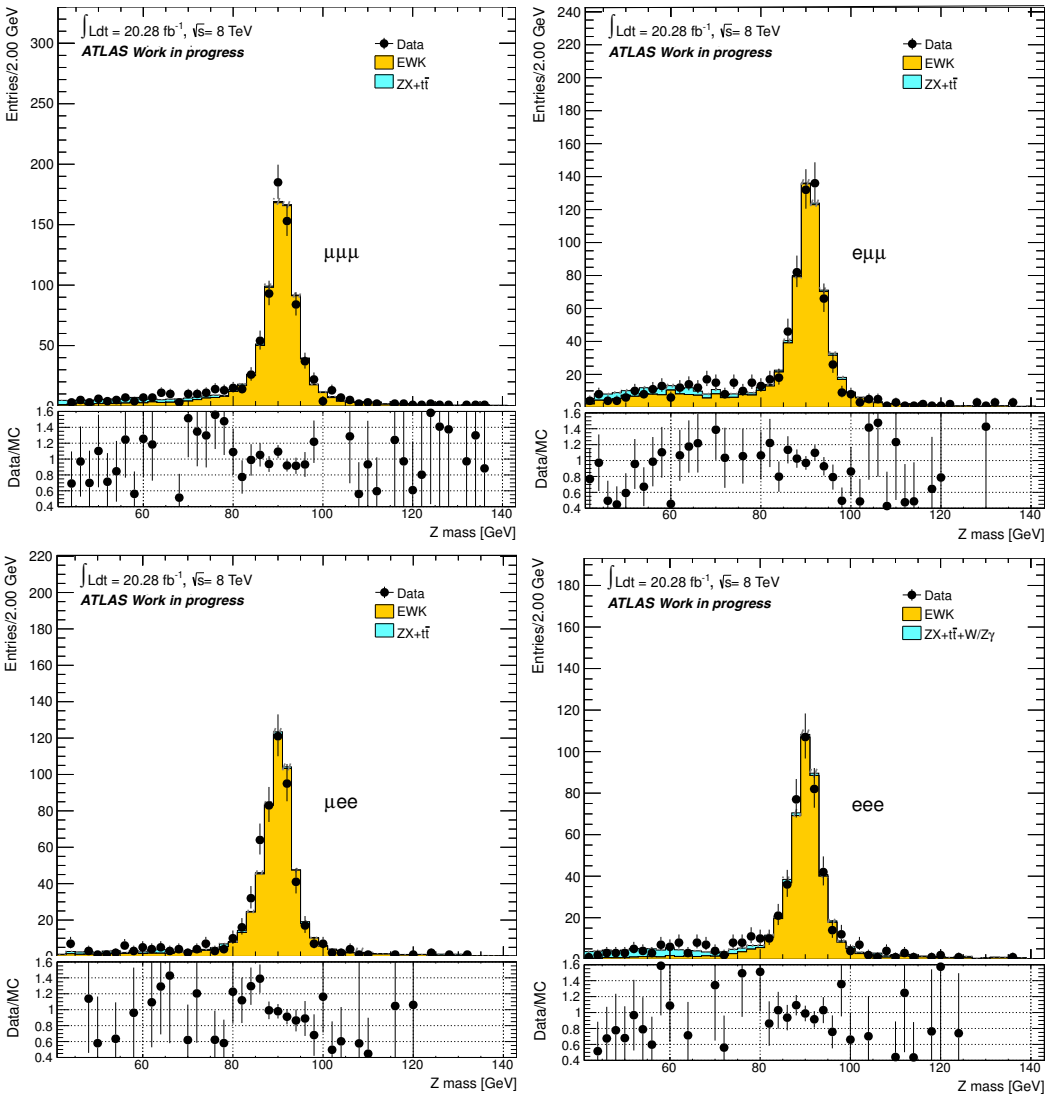

Figure 8.18: Template fit results for the $\mu\mu\mu$ (top left), $e\mu\mu$ (top right), μee (bottom left) and eee (bottom right) topologies respectively. The fit is done on the mass of the Z-boson.

8.7 Cut-based analysis yields

Table 8.31 presents the data and MC, both from signal and background processes, expectation yields. The uncertainties quoted here are statistical only and in the table are depicted along with the yields the overall signal-to-background ratio as well as the fractional difference between data and MC.

Topology	$\mu\mu\mu$	$e\mu\mu$	μee	eee	Total
Data	663±26	539±23	483±22	406±20	2091±46
Total expected	584.1±4.4	477.9±5.4	397.7±3.3	334.4±4.3	1794.0±8.9
WZ Signal	484.2±2.3	357.2±1.1	327.3±1.1	246.7±1.0	1415.4±3.0
Total background	99.9±3.7	120.7±5.3	70.4±3.1	87.6±4.2	378.6±8.3
DD background	46.6±3.7	74.3±5.3	34.2±3.1	54.4±4.2	209.5±8.3
MC background	53.3±0.5	46.4±0.5	36.2±0.5	33.2±0.3	169.1±0.9
ZZ	40.1±0.3	36.5±0.3	26.9±0.3	25.9±0.2	129.4±0.6
$t\bar{t}$+V	10.0±0.3	7.9±0.3	7.3±0.3	5.9±0.2	31.2±0.5
W^+W^-	0.1±0.1	0.1±0.1	0.1±0.1	0.1±0.1	0.3±0.1
VVV	1.0±0.0	0.8±0.0	0.7±0.0	0.5±0.0	3.1±0.1
VVDPS	2.2±0.2	1.1±0.2	1.2±0.1	1.4±0.1	8.2±0.3
(Data-MC)/MC [%]	13.5	12.8	21.4	21.4	16.6
S/B	4.9	3.0	4.7	2.8	3.8

Table 8.31: Data and expected yields, total and for each topology. The uncertainties shown are statistical alone. The background sources calculated with the data-driven method (TF) are the Z+jets, $t\bar{t}$+single-top and the Z/γ.

8.8 Systematic uncertainties

Three categories of systematic uncertainties are present in this analysis: theoretical uncertainties on the estimation of the cross-sections, reconstructed object uncertainties and normalisation uncertainties on the background sources estimated from MC.

8.8.1 Theoretical uncertainties

QCD scale uncertainties

The predicted total cross-section using `MCFM 6.8` [19] is:

$$\sigma_{MCFM}^{NLO,tot} = 20.311 \pm 0.013(stat)$$

All possible combinations of independent variations by x_i =2 and x_i =1/2, on the factorisation (i=F, x_F) and renormalisation (i=R, x_R) scales are considered. These are compared to the nominal dynamic scale combination of $x_R = x_F$ =1. A fixed scale consisting of $\mu_R = \mu_F = (M_W + M_Z)/2$ is treated as well and the difference from the nominal case is taken as the total scale uncertainty on the $W^{\pm}Z$ predicted cross-sections. Table 8.32 lists the scale combinations. The last line is the comparison between the nominal dynamic scale of $\mu_R = \mu_F$ =1 and the fixed scale.

Scale variation		Phase space	
x_R	x_F	total	fiducial
0.5	0.5	3.45%	4.11%
0.5	1	3.20%	3.59%
0.5	2	3.11%	3.26%
1	0.5	0.17%	0.27%
1	1	0.00%	0.00%
1	2	−0.10%	−0.33%
2	0.5	−2.58%	−2.78%
2	1	−2.69%	−3.04%
2	2	−2.74%	−3.27%
$\mu_F = \mu_R = (M_W + M_Z)/2$		6.97%	7.38%

Table 8.32: Deviations of the WZ production cross section for different theoretical choices of the QCD scales compared to the nominal value with $\mu_F = \mu_R = M_{WZ}$. The renormalisation and factorisation scale are varied independently by x_R and x_F. The deviations between the nominal scale values and fixed scales of $\mu_F = \mu_R = (M_W + M_Z)/2$ are presented in the last line.

PDF uncertainties

The PDF uncertainties are estimated by adding the errors from the 52 CT10 eigenvector sets in quadrature, for the fiducial and the total phase-space. The result is divided by 1.645 in order to have the 68% Confidence Level (CL) intervals. Calculations of the fiducial and total cross-sections are also performed using the MSTW2008 NLO PDF and the ATLAS NLO PDF sets and the difference with the CT10 calculations is quoted. The total uncertainty on the theoretical prediction of the cross-section is estimated by adding linearly the PDF and QCD scale uncertainties, as suggested in [20]. Table 8.33 lists the PDF uncertainties on the $W^{\pm}Z$ fiducial and total cross-sections.

	W^+Z		W^-Z	
	total	fiducial	total	fiducial
CT10 eigenvectors (68% C.L)	+2.11%	+2.22%	+2.30%	+2.34%
	-2.41%	-2.47%	-2.51%	-2.40%
CT10 to MSTW2008	+0.33%	+0.11%	+2.80%	+3.82%
CT10 to ATLAS	+1.27%	+0.20%	+4.78%	+3.54%

Table 8.33: PDF uncertainties on the $W^{\pm}Z$ fiducial and total production cross-sections.

8.8.2 Systematic uncertainties on the reconstructed objects

The reconstructed objects relevant to this analysis are muons, electrons and $E_{\mathrm{T}}^{\mathrm{miss}}$. The following sections describe the systematic uncertainties affecting each one of them.

Electrons

Electron reconstruction and identification efficiency, energy scale and smearing, calorimeter isolation and charge misidentification are the sources of systematic uncertainties. They are evaluated in MC by varying each source within its uncertainty and measuring the fractional yield change. The uncertainties used are provided by the `Egamma` group. Table 8.34 lists the effect of the electron systematic uncertainties.

1. **Reconstruction and identification efficiency:** The MC is weighted by scale factors provided by the `Egamma` group in order to account for the differences between data and MC. These scale factors are varied within their uncertainties and the total electron efficiency uncertainty is the quadratic sum of the reconstruction and identification efficiency uncertainties.

2. **Energy scale and smearing:** Using decays of the Z-boson to electron pairs, the energy scale is calibrated in data and MC. The most important factors that affect the energy scale are the description of the material in ATLAS and the calibration of the EM calorimeter. Also, in order to match the data, the electron resolution is corrected in MC. The `Egamma` provides the `EnergyRescalerUpgrade` tool which is used in order to perform the corrections associated with the energy scale and resolution smearing.

3. **Isolation:** Isolation scale factors are provided and applied by the `ElectronEfficiency` tool. This systematic is evaluated by varying the scale factors within their uncertainty and measuring the yield fractional change.

Muons

There are four sources of systematic uncertainties in the case of muons: the reconstruction efficiency, the momentum resolution, the momentum scale and the isolation. Table 8.34 lists the effect of the muon systematic uncertainties.

1. **Reconstruction efficiency:** The `MCP` group provides the tool in order to apply and estimate the uncertainty due to the muon reconstruction scale factors. The scale factors are varied within their uncertainties and the fractional yield change is quoted as the associated uncertainty.

2. **Scale and Resolution:** These affect the determination of the muon p_{T}. The options the official tool accepts for the estimation of the scale and resolution uncertainties are `IDUP`, `IDLOW`, `MSUP`, `MSLOW` for resolution and `SCALEUP`, `SCALELOW` for the scale respectively. Analytic information on the aforementioned sources of systematic uncertainty are available in [21].

3. **Charge misidentification:** No evidence of (significant) charge misidentification for CB muons have been found on 8 TeV data [22] and therefore this contribution is considered to be negligible.

4. **Isolation:** The isolation scale factor is given in p_{T}-bins and it is derived from data using the tag and probe method.

Missing transverse energy

The $E_{\mathrm{T}}^{\mathrm{miss}}$ uncertainties can be evaluated using the prescriptions in [14]. $E_{\mathrm{T}}^{\mathrm{miss}}$ is build from other physical objects and therefore the uncertainties on these objects can be propagated to extract the uncertainty on $E_{\mathrm{T}}^{\mathrm{miss}}$, i.e jet energy scale. The following are the sources of systematic uncertainties on the $E_{\mathrm{T}}^{\mathrm{miss}}$calculation:

1. Soft $E_{\mathrm{T}}^{\mathrm{miss}}$ terms energy scale and resolution;

2. Muon energy scale and resolution;

3. Electron energy scale and resolution;

4. Jet energy scale;

5. Pile-up description by the MC;

All MET uncertainties, apart from the muon and electron resolution and scale uncertainties that are evaluated separately in their relevant sections and are not considered here again, are propagated as recommended by the relevant performance groups to the $E_{\mathrm{T}}^{\mathrm{miss}}$. The soft terms resolution uncertainty is at the order of 1% and the scale uncertainty is 6%, for the $E_{\mathrm{T}}^{\mathrm{miss}}$ type of `MET_RefFinal_STVF` used in the 2012 analysis. The effect on the scale is calculated by varying the $E_{x,y}^{soft-Terms}$ up and down by 6% and recalculating the $E_{\mathrm{T}}^{\mathrm{miss}}$. The effect on the resolution uncertainty is evaluated by selecting a Gauss shift from the resolution uncertainty and applying it to $E_{x,y}^{soft-Terms}$.

8.8.3 Normalisation uncertainties on background processes

The ZZ, $t\bar{t}$+V and VVV background sources contributions are estimated from MC. Their normalisation uncertainties are 7% for the ZZ source [23] and 30% for the $t\bar{t}$ [24] and VVV sources. Finally, a 50% uncertainty is assigned to the VV DPS background source. Table 8.34 list the impact of all systematic uncertainties considered in this analysis.

8.9 Changes of the current analysis with respect to Moriond

This analysis utilises the full set of 8 TeV data collected in 2012 with the ATLAS detector and aims at several Physics goals. More specific, it aims in measuring the fiducial and total cross-sections, to provide the differential cross-section with respect to the Z boson p_{T}, the m_{WZ}, the W boson p_{T} and the $|y_Z - y_{\ell,W}|$ variables and also in setting stringent limits on the aTGCs as well as on anomalous Quartic Gauge Couplings (aQGCs). Finally, among the goals are polarisation searches for spin measurements. The main differences with respect to the 8 TeV Moriond analysis are listed below:

1. The Moriond analysis provided the cross-sections measurements using a sample of 2012 8 TeV data that corresponded to an integrated luminosity of 12.83 fb^{-1}, while this analysis is using the full 2012 data set, rising the integrated luminosity to 20.18 fb^{-1};

2. In the present thesis the Template Fit method is the default background method for all topologies (instead of the mixed strategy used in the previous publication where

Total Relative Uncertainties [%]				
Source	eee	$ee\mu$	$\mu\mu e$	$\mu\mu\mu$
e - Energy Scale	$^{+0.67}_{-0.84}$	$^{+0.28}_{-0.49}$	$^{+0.39}_{-0.41}$	$^{-0.01}_{+0.01}$
e - Energy Smearing	$^{-0.17}_{+0.16}$	$^{-0.14}_{+0.10}$	$^{-0.02}_{+0.02}$	$^{-0.00}_{+0.00}$
e - Id. Efficiency	$^{+2.60}_{-2.56}$	$^{+1.61}_{-1.60}$	$^{+0.93}_{-0.93}$	$^{+0.00}_{+0.00}$
e - Rec. Efficiency	$^{+0.96}_{-0.95}$	$^{+0.64}_{-0.64}$	$^{+0.30}_{-0.30}$	$^{+0.00}_{+0.00}$
e - Iso. Efficiency	$^{+0.66}_{-0.65}$	$^{+0.43}_{-0.43}$	$^{+0.22}_{-0.22}$	$^{+0.00}_{+0.00}$
μ - p_T Scale	$^{+0.00}_{+0.00}$	$^{+0.04}_{-0.04}$	$^{+0.03}_{-0.03}$	$^{+0.08}_{-0.08}$
μ - p_T Smearing MS	$^{+0.00}_{+0.00}$	$^{-0.01}_{+0.00}$	$^{-0.07}_{+0.03}$	$^{-0.02}_{+0.01}$
μ - p_T Smearing ID	$^{+0.00}_{+0.00}$	$^{+0.00}_{-0.01}$	$^{-0.03}_{+0.03}$	$^{-0.02}_{-0.01}$
μ - Rec. Efficiency	$^{+0.00}_{+0.00}$	$^{+0.33}_{-0.33}$	$^{+0.60}_{-0.60}$	$^{+0.92}_{-0.94}$
μ - Iso. Efficiency	$^{+0.00}_{+0.00}$	$^{+0.03}_{-0.03}$	$^{+0.06}_{-0.06}$	$^{+0.08}_{-0.08}$
jet - Effective NP1	$^{-0.08}_{+0.09}$	$^{-0.05}_{+0.04}$	$^{-0.05}_{+0.06}$	$^{-0.05}_{+0.05}$
jet - Effective NP2	$^{+0.09}_{-0.09}$	$^{+0.05}_{-0.05}$	$^{+0.06}_{-0.06}$	$^{+0.04}_{-0.05}$
jet - Effective NP3	$^{-0.01}_{+0.00}$	$^{-0.00}_{+0.02}$	$^{+0.01}_{-0.01}$	$^{-0.01}_{+0.03}$
jet - Effective NP4	$^{+0.00}_{+0.01}$	$^{-0.00}_{+0.01}$	$^{-0.01}_{+0.01}$	$^{+0.01}_{+0.00}$
jet - Effective NP5	$^{+0.01}_{+0.00}$	$^{+0.01}_{-0.01}$	$^{+0.00}_{-0.01}$	$^{-0.00}_{+0.00}$
jet - Effective NP6	$^{-0.01}_{+0.02}$	$^{-0.00}_{+0.00}$	$^{-0.01}_{+0.00}$	$^{+0.00}_{-0.01}$
jet - *eta* inter. calib. modelling	$^{-0.15}_{+0.15}$	$^{-0.13}_{+0.10}$	$^{-0.16}_{+0.12}$	$^{-0.12}_{+0.10}$
jet - *eta* inter. calib. stat. and method	$^{-0.01}_{+0.03}$	$^{-0.01}_{+0.01}$	$^{-0.01}_{+0.02}$	$^{-0.02}_{+0.02}$
jet - Pileup Offset NPV	$^{-0.00}_{+0.01}$	$^{-0.02}_{+0.00}$	$^{-0.00}_{+0.02}$	$^{-0.00}_{+0.01}$
jet - Pileup Offset MU	$^{-0.01}_{+0.00}$	$^{-0.02}_{+0.00}$	$^{-0.01}_{+0.00}$	$^{+0.00}_{+0.00}$
jet - Pileup PtTerm	$^{-0.01}_{+0.02}$	$^{-0.01}_{+0.01}$	$^{-0.00}_{+0.00}$	$^{-0.01}_{+0.01}$
jet - Pileup RhoTopology	$^{-0.04}_{+0.06}$	$^{-0.02}_{+0.02}$	$^{-0.02}_{+0.05}$	$^{-0.03}_{+0.03}$
jet - FlavorCompUncert.	$^{-0.13}_{+0.13}$	$^{-0.09}_{+0.07}$	$^{-0.10}_{+0.11}$	$^{-0.08}_{+0.06}$
jet - FlavorResponseUncert.	$^{-0.08}_{+0.08}$	$^{-0.05}_{+0.05}$	$^{-0.06}_{+0.07}$	$^{-0.05}_{+0.05}$
jet - Res. Smearing	$^{+0.01}_{-0.06}$	$^{-0.04}_{-0.09}$	$^{-0.04}_{-0.10}$	$^{-0.02}_{-0.02}$
E_T^{miss} - SoftTerm Scale	$^{+0.03}_{+0.01}$	$^{-0.02}_{+0.00}$	$^{+0.00}_{-0.02}$	$^{-0.02}_{-0.01}$
E_T^{miss} - SoftTerm Res.	$^{+0.02}_{-0.01}$	$^{+0.02}_{-0.01}$	$^{-0.02}_{+0.02}$	$^{-0.01}_{-0.02}$
Pile-up	$^{+-.25}_{+0.29}$	$^{-0.16}_{+0.17}$	$^{-0.11}_{+0.11}$	$^{-0.09}_{+0.07}$
Trigger (e and μ)	$^{+0.03}_{-0.03}$	$^{+0.07}_{-0.07}$	$^{+0.14}_{-0.14}$	$^{+0.29}_{-0.29}$
Signal stat. (MC)	$^{0.41}_{0.41}$	$^{0.29}_{0.29}$	$^{0.28}_{0.28}$	$^{0.30}_{0.30}$

Table 8.34: Summary of the effect of $\pm 1\sigma$ variations of the different "object" systematics on the number of reconstructed WZ signal events. Upper and lower numbers corresponds to a $+1\sigma$ and -1σ variation of the corresponding systematic uncertainty source, respectively. The high statistic POWHEG+PYTHIAMC sample is used.

the side-band fit method was used for the $Z+\mu$ channels and the Reduced matrix method was adopted for the Z+e channels);

3. The p_{T} value on the ZZ veto cut was lowered from 15 GeV to 7 GeV;

4. The track-based isolation criterion imposed on the lepton originating from the W boson was tightened to 10% (from 15%).

5. A tighter requirement on the W boson transverse mass is applied (from 20 GeVto 30 GeV). This change was imposed as a necessity derived from the next step;

6. The $E_{\mathrm{T}}^{\mathrm{miss}}$ requirement was dropped. The reason for abandoning the $E_{\mathrm{T}}^{\mathrm{miss}}$ cut was the distortion it created on the $\cos\theta_W^*$ distribution, which is critical in the polarisation measurement procedure;

8.10 Cross-section extraction

8.10.1 Analysis phase-space

The selection cuts imposed in the analysis reduce furthermore the coverage that ATLAS provides on the phase-space. The differences in the selection requirements for muons and electrons dictate that the fiducial volumes of the four distinct final-state topologies will be different. In order to be able to estimate the combined fiducial cross-section, a common fiducial phase-space among the four topologies must be defined. This fiducial phase-space is defined by a series of cuts, similar to the ones imposed in the analysis, that are very close to the detector acceptance. The following cuts are applied to generator-level objects (electrons and muons) which are "dressed" with photons from Final State Radiation (FSR), before any simulation:

- All leptons must be within $|\eta|$ <2.5.

- Leptons originating from Z boson decays must have p_{T}>15 GeV.

- The W boson lepton must have p_{T}>20 GeV.

- The condition 66 GeV < m_{ll} <116 GeV must be satisfied for the leptons assigned to the Z boson.

- The W boson transverse mass is required to be greater than 30 GeV.

- There must be a separation in the $\eta-\phi$ space of ΔR >0.2 between the Z boson leptons and of ΔR >0.3 between the W boson lepton and each of the Z boson leptons.

- The Z boson candidate must have an invariant mass which rests within a 10 GeV window from the `PDG` mass: $|m_{ll} - 91.1876|$ <10 GeV.

Regarding the total phase-space of the $W^{\pm}Z$ analysis, there is only one restriction, imposed on the invariant mass of the reconstructed Z boson: 66 GeV $< m_{ll} <$ 116 GeV.

Following the recommendations from the ATLAS Truth Particle Workshop [25], a user-defined algorithm has been developed, namely the *Resonant shapes* algorithm, whose details are presented in the following subsection. The usage of such a user-defined algorithm provides the possibility to associate a lepton to its parent boson irrespective of the presence or not of the parent association algorithm in the generator.

Resonant shapes algorithm

According to the Quantum Mechanics principles, it is not possible to have the per event filiation of every final-state particle to their parental partons or bosons. However, it is necessary to be able to associate generator-level leptons to a parent boson in order to be able to correct the raw measurements to a phase space at "particle level", that is close to the detector fiducial phase space. For this reason the *Resonant shapes* algorithm has been developed. It uses the final-state generator-level leptons (status=1) that are *dressed* with Final State Radiation (FSR) photons. The process of dressing consists of gathering all photons closer than 0.1 in ΔR to a lepton and adding their four-momenta to the lepton's four-momentum. The photons used should be generator-level quantities[6] and they should not originate from a hadron nor a τ lepton. Events with τ leptons are not considered. The dressed with FSR leptons are then matched to the three highest-p_{T} Matrix Element (ME) leptons (the generator-level leptons before any radiation). The final input element for the algorithm are the neutrinos; the highest-p_{T} is selected and the event is kept in case it does not violate leptonic number conservation.

[6]This is implemented in the analysis by asking for photons with a barcode of less than 200000, in order to avoid `GEANT` particles, i.e before simulation.

After gathering the three dressed leptons and the neutrino, all possible combinations, preserving leptonic flavour, of lepton-neutrino are considered along with all possible same-flavour, opposite-charge lepton pairs. The invariant masses of the combinations are calculated ($M_{(\ell\nu)k}$ and $M_{(\ell\ell)k}, k = 1, 2$) and the decision is made based on the highest probability, calculated by Equation 8.2:

$$P_k = \frac{1}{(M^2_{(\ell\ell)k} - M^2_Z)^2 + \Gamma^2_Z M^2_Z} \times \frac{1}{(M^2_{(\ell\nu)k} - M^2_W)^2 + \Gamma^2_W M^2_W} \tag{8.2}$$

with Γ_Z and Γ_W the total width of the Z and W bosons respectively (`PDG` values). The two terms in Equation 8.2 represent the Breit-Wigner distributions of the two bosons, while the final choice corresponds to the combination that yields the highest P_k.

8.10.2 C_{WZ} correction factor

In order to be able to correct the reconstructed cross-section to the truth-level cross-section, which is defined in the fiducial volume, an efficiency correction term C_{WZ} is used. This comprises of all the event and objects corrections applied to the MC signal sample, such as pileup re-weighting, z-vertex position re-weighting, trigger efficiency, reconstruction, identification and isolation efficiency, e.t.c. The C_{WZ} correction factor can be defined from Equation 8.3:

$$C_{WZ} = \frac{N^{MC}_{reco,WZ\to\ell\nu\ell'\ell'}}{N^{MC}_{gen,WZ\to\ell\nu\ell'\ell'}} \tag{8.3}$$

where $N^{MC}_{reco,WZ\to\ell\nu\ell'\ell'}$ is the number of MC signal events that pass all the reconstruction level analysis cuts and $N^{MC}_{gen,WZ\to\ell\nu\ell'\ell'}$ the number of events that pass the fiducial volume cuts (as defined in section 8.10.1) at generator level.

The C_{WZ} factor gives the probability of reconstructing an event. Since there are four discrete signatures (coming from all the possible decays of the W and Z bosons to electrons and muons) and different correction factors are applied to electrons and muons, the C_{WZ} factor is calculated separately for the four final-states. The resonant shapes algorithm has been used in this analysis at generator level in order to extract the C_{WZ} factors. Table 8.35 shows the calculated C_{WZ} factors with both the resonant shapes algorithm as well as the usage of the POWHEGbuilt-in association algorithm.

Association algorithm	*eee*	*μee*	*eμμ*	*μμμ*
Resonant Shapes	0.406 ± 0.002	0.543 ± 0.002	0.589 ± 0.002	0.803 ± 0.003
POWHEG built-in	0.404 ± 0.002	0.538 ± 0.002	0.548 ± 0.002	0.797 ± 0.003

Table 8.35: C_{WZ} factors calculated per final-state topology for the resonant shapes and the POWHEG built-in algorithm. The factors computed with the two algorithm are in good agreement.

8.10.3 A_{WZ} correction factor

The fiducial cross-section is measured in the fiducial volume of the detector. To determine the total $W^{\pm}Z$ production cross-section, i.e in the total production phase-space, the acceptance of the fiducial cuts must be estimated. As it has been mentioned, there is only one requirement on the total phase-space: the mass of the Z-boson should rest between 66 and 116 GeV. The correction factor for the extrapolation of the fiducial cross-section to the total phase-space is defined by Equation 8.4:

$$A_{WZ} = \frac{N^{MC}_{gen,WZ\to\ell\nu\ell'\ell',fid}}{N^{MC}_{gen,WZ\to\ell\nu\ell'\ell',all}} \tag{8.4}$$

where $N^{MC}_{gen,WZ\to\ell\nu\ell'\ell',fid}$ is the number of events generated in the fiducial volume, and $N^{MC}_{gen,WZ\to\ell\nu\ell'\ell',all}$ the total number of generated events. The resonant shapes algorithm has been used in order to calculate the A_{WZ} factors per final-state topology. Table 8.36 shows the calculated A_{WZ} factors with both the resonant shapes as well as the POWHEG built-in algorithm.

Association algorithm	*eee*	*μee*	*eμμ*	*μμμ*
Resonant Shapes	0.389 ± 0.001	0.398 ± 0.001	0.398 ± 0.001	0.388 ± 0.001
POWHEG built-in	0.397 ± 0.001	0.398 ± 0.001	0.399 ± 0.001	0.397 ± 0.001

Table 8.36: A_{WZ} factors calculated per final-state topology for the resonant shapes and the POWHEG built-in algorithm. The factors computed with the two algorithm are in good agreement.

8.10.4 Cross-section measurement

In order to measure the $W^{\pm}Z$ fiducial cross-section in pp collisions, all four topologies are taken into account. The fiducial cross-section is given by Equation 8.8:

$$\sigma_{fid}(pp \to WZ\ X) \cdot Br_{W\to\ell\nu} \cdot Br_{Z\to\ell'\ell'}\ X = \frac{N_{\text{data}} - N_{\text{bg}}}{L \cdot C_{WZ}^{\ell,\ell'}} \times (1 - \frac{N_{\text{MC,rec}}^{\tau}}{N_{\text{MC,rec}}^{all}}) \tag{8.5}$$

where $\ell, \ell' = e, \mu$, $all = e + \mu + \tau$. N_{data} is the number of selected events in data, N_{bg} the number of corresponding background events and L is the integrated luminosity of the data samples. The $C_{WZ}^{\ell,\ell'}$ factor constitutes of the reconstruction, identification and trigger efficiency along with FSR effects. The last term in Equation 8.8 defines the correction factor applied in order to account for the number of simulated events containing τ decays of the W, Z bosons, where the ratio inside the parentheses is found to be at the order of 4%.

Using a negative log-likelihood function the cross-section is estimated as the one that minimises this function. Estimates from the different decay channels are combined, where each channel can be treated as a different measurement of the cross-section and the total likelihood is the product of the individual channel probabilities. The likelihood function is defined in Equation 8.6:

$$-\ln L(\sigma, \{x_k\}) = \sum_{i=1}^{4} -\ln\left(\frac{e^{-(N_s^i(\sigma,\{x_k\})+N_b^i(\{x_k\}))} \times (N_s^i(\sigma,\{x_k\}) + N_b^i(\{x_k\}))^{N_{obs}^i}}{(N_{obs}^i)!} \right) + \sum_{k=1}^{n} \frac{x_k^2}{2} \tag{8.6}$$

where the expression inside the log is the Poisson probability that the expected number of signal and background events produce the observed number of events and the last term accounts for all the Gaussian constraints on the nuisance parameters. The error returned by the minimisation corresponds to the total error. In order to decompose it to the statistical and systematic uncertainties, all the values of the nuisance parameters are fixed to the ones returned by the main fit and the fit is performed again. This would account for the statistical component of the total uncertainty. The systematic component can be then estimated as the quadratic difference between the total and the statistical uncertainty.

Table 8.37 presents the results of the fiducial cross-sections for each of the four topologies as well as the combined cross-section. The total cross-section is estimated by extrapolating these measurements to the total phase-space, using the average A_{WZ} factor of the $\mu^{\pm}e^{+}e^{-}$ and $e^{\pm}\mu^{+}\mu^{-}$ topologies, and it is calculated to:

$$\sigma_{WZ}^{tot} = 23.89^{+0.64}_{-0.63}(stat.)^{+0.43}_{-0.36}(syst.)^{+0.75}_{-0.72}(lumi.) \pm 0.33(th.)[pb] \tag{8.7}$$

Fiducial cross section in Equation 8.8:

$$\sigma_{WZ}^{fid} = 34.56^{+0.93}_{-0.92}(stat.)^{+0.61}_{-0.50}(syst.)^{+1.09}_{-1.02}(lumi.)[fb] \tag{8.8}$$

Figure 8.19 shows the likelihood function versus the total cross-section is shown, with the vertical lines marking the positions of the $\pm\sigma$ confidence interval. The result in Equation 8.7 can be compared with the prediction of $\sigma_{W^{\pm}Z}$ =22.7±2.7 [pb] from [26] that has full NLO QCD and EW corrections.

Channel	Cross-Section [fb]
$\mu\mu\mu$	$33.42^{+1.55}_{-1.51}(\text{stat})^{+0.57}_{-0.42}(\text{syst})^{+1.06}_{-0.99}(\text{lumi})$
$e\mu\mu$	$33.72^{+1.90}_{-1.84}(\text{stat})^{+0.75}_{-0.62}(\text{syst})^{+1.08}_{-1.02}(\text{lumi})$
μee	$36.25^{+1.96}_{-1.90}(\text{stat})^{+1.04}_{-0.90}(\text{syst})^{+1.13}_{-1.08}(\text{lumi})$
eee	$37.16^{+2.39}_{-2.31}(\text{stat})^{+1.50}_{-1.27}(\text{syst})^{+1.18}_{-1.22}(\text{lumi})$
Combined	$34.56^{+0.93}_{-0.92}(\text{stat})^{+0.61}_{-0.50}(\text{syst})^{+1.09}_{-1.02}(\text{lumi})$

Table 8.37: Measured fiducial cross-sections for each of the four topologies and combined.

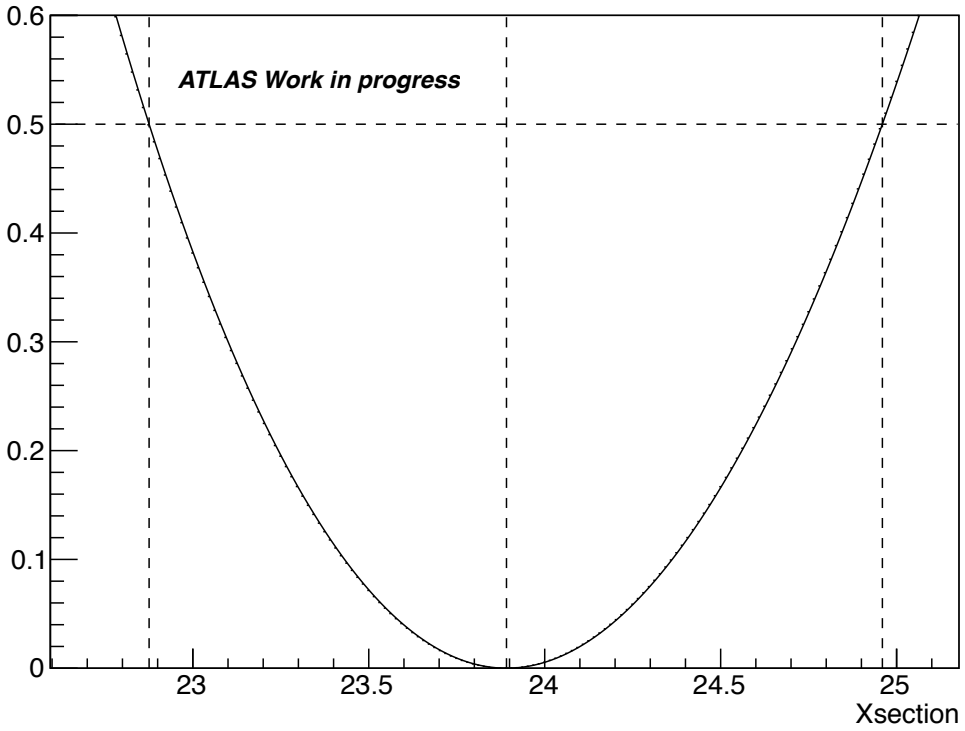

Figure 8.19: The profile likelihood function versus the combined cross-section. The vertical lines represent the $\pm\sigma$ confidence intervals.

Bibliography

[1] ATLAS Collaboration, G. Aad et al., *Measurement of WZ production in proton-proton collisions at $\sqrt{s} = 7$ TeV with the ATLAS detector*, Eur.Phys.J. **C72** (2012) 2173, arXiv:1208.1390 [hep-ex].

[2] CDF Collaboration Collaboration, T. Aaltonen et al., *Measurement of the WZ Cross Section and Triple Gauge Couplings in $p\bar{p}$ Collisions at $\sqrt{s} = 1.96$ TeV*, Phys.Rev. **D86** (2012) 031104, arXiv:1202.6629 [hep-ex].

[3] D0 Collaboration Collaboration, V. M. Abazov et al., *Measurement of the $WZ \to \ell\nu\ell\ell$ cross section and limits on anomalous triple gauge couplings in $p\bar{p}$ collisions at $\sqrt{s} = 1.96$ TeV*, Phys.Lett. **B695** (2011) 67–73, arXiv:1006.0761 [hep-ex].

[4] ATLAS Collaboration, *A Measurement of WZ Production in Proton-Proton Collisions at $\sqrt{(s)} = 8$ TeV with the ATLAS Detector*, ATLAS Note (2013). https://cds.cern.ch/record/1525557?ln=en.

[5] ATLAS Collaboration, G. Aad et al., *Improved luminosity determination in pp collisions at $\sqrt{s} = 7$ TeV using the ATLAS detector at the LHC*, Eur.Phys.J. **C73** (2013) 2518, arXiv:1302.4393 [hep-ex].

[6] T. Sjostrand, S. Mrenna, and P. Z. Skands, *PYTHIA 6.4 Physics and Manual*, JHEP **0605** (2006) 026, arXiv:hep-ph/0603175 [hep-ph].

[7] M. L. Mangano, M. Moretti, F. Piccinini, R. Pittau, and A. D. Polosa, *ALPGEN, a generator for hard multiparton processes in hadronic collisions*, JHEP **0307** (2003) 001, arXiv:hep-ph/0206293 [hep-ph].

[8] ATLAS Collaboration.
https://twiki.cern.ch/twiki/bin/viewauth/AtlasProtected/ExtendedPileupReweighting.

[9] ATLAS Collaboration.
https://twiki.cern.ch/twiki/bin/viewauth/AtlasProtected/InDetTrackingPerformanceGuidelines.

[10] ATLAS Collaboration Collaboration, G. Aad et al., *Electron and photon energy calibration with the ATLAS detector using LHC Run 1 data*, Eur.Phys.J. **C74** no. 10, (2014) 3071, arXiv:1407.5063 [hep-ex].

[11] ATLAS Collaboration,
"https://twiki.cern.ch/twiki/bin/viewauth/atlasprotected/mcpanalysisguidelinesdata2012.".

[12] ATLAS Collaboration,
"https://twiki.cern.ch/twiki/bin/viewauth/atlasprotected/jetvertexfraction.".

[13] ATLAS Collaboration,
"https://twiki.cern.ch/twiki/bin/viewauth/atlasprotected/howtocleanjets2012.".

[14] ATLAS Collaboration, *Performance of Missing Transverse Momentum Reconstruction in ATLAS studied in Proton-Proton Collisions recorded in 2012 at* $\sqrt{s}$ *= 8 TeV*, ATLAS Note no. ATLAS-CONF-2013-082, (2013).

[15] ATLAS Collaboration,
"https://twiki.cern.ch/twiki/bin/viewauth/atlas/goodrunsliststutorial,
http://atlasdqm.web.cern.ch/atlasdqm/grlgen/.".

[16] ATLAS Collaboration, "https://atlas-datasummary.cern.ch/lumicalc.".

[17] J. Beringer et al., *The Review of Particle Physics*, Phys. Rev. **D86** (2012).

[18] R. J. Barlow and C. Beeston, *Fitting using finite Monte Carlo samples*, Comput. Phys. Commun. **77** (1993) 219–228.

[19] J. M. Campbell and R. Ellis, *MCFM for the Tevatron and the LHC*, Nucl.Phys.Proc.Suppl. **205-206** (2010) 10–15, arXiv:1007.3492 [hep-ph].

[20] LHC Higgs Cross Section Working Group Collaboration, S. Dittmaier et al., *Handbook of LHC Higgs Cross Sections: 1. Inclusive Observables*, arXiv:1101.0593 [hep-ph].

[21] M. Goblirsch, M. Vanadia, A. Salvucci, F. Sforza, O. Kortner, A. Dimitrievska, and N. Vranjes, *Preliminary results on the muon reconstruction efficiency, momentum resolution, and momentum scale in ATLAS 2012 pp collision data*, Tech. Rep. ATLAS-COM-CONF-2013-096, CERN, Geneva, Jul, 2013.

[22] https://cds.cern.ch/record/1555805/files/ATL-COM-PHYS-2013-810.pdf.

[23] J. Baglio, L. D. Ninh, and M. M. Weber, *Massive gauge boson pair production at the LHC: a next-to-leading order story*, Phys.Rev. **D88** (2013) 113005, arXiv:1307.4331.

[24] https://twiki.cern.ch/twiki/bin/viewauth/AtlasProtected/TTplusV.

[25] ATLAS Collaboration, "https://twiki.cern.ch/twiki/bin/viewauth/atlasprotected/particledefinitionworkshop.".

[26] J. Baglio, L. D. Ninh, and M. M. Weber, *Massive gauge boson pair production at the LHC: a next-to-leading order story*, Phys.Rev. **D88** (2013) 113005, arXiv:1307.4331.

Chapter 9

Unfolding

In the Platonic philosophy, we can only perceive part of the real world; beyond our senses rests the true physical object, which we can never grasp. However, spectra of physical observables measured in HEP experiments, can be corrected for various detector effects, namely finite resolution, limited acceptance and imperfect efficiency, through the process of unfolding. Thus, measured spectra can be reduced to 'true' spectra, allowing cross-experiment results comparison.

9.1 Unfolding notion and methods

Considering the detector-related factors that distort the generated distributions of physical observables and modelling them, along with the theoretical models adopted for a particular analysis, MC simulation can be used in order to construct a map describing the migration of events: from a generated bin to a reconstructed. This is known as the response matrix $\mathbf{A}$ (or migration matrix) and the relation between the *true* spectra $\mathbf{x}$ and the measured ones $\mathbf{y}$ can be expressed as:

$$\mathbf{y} = \mathbf{A} \cdot \mathbf{x} \tag{9.1}$$

In order to translate measured distributions to generated ones, one has to calculate the inverse of $\mathbf{A}$, namely $\mathbf{A}^{-1}$. Then the 'true' spectra can be obtained from:

$$\mathbf{x} = \mathbf{A^{-1}} \cdot \mathbf{y} \tag{9.2}$$

Alas, the simplicity of this notion is crippled by wildly oscillating solutions that occur, since simple algebraic manipulation of the response matrix is (usually) not feasible. A number of methods that deal with the problem of the unfolding of differential distributions have been developed; the following list is by all means not exhaustive nor elaborate:

1. Bayesian Iterative [1]: by D'Agostini. Iterative unfolding is an old concept [2]; however D'Agostini re-invented it and interpreted it in the context of Bayesian statistics.

2. Iterative Dynamically Stabilised, (IDS) [3]: It is based on the idea that if two conditions are satisfied, namely the MC simulation provides a relatively good description of the data and of the detector effects, then one could use the transfer matrix in order to compute a matrix of unfolding probabilities. It uses a regularisation function[1] in order to dynamically reduce the fluctuations,preventing thus the transfer of events, particularly in the subtracted background. IDS has only one regularisation parameter, λ, to be optimised during the unfolding process. Developed by Bogdan Malaescu.

3. Singular Value Decomposition, (SVD) [4]: A method developed by Andreas Hocker and Vakhtang Kartvelishvili that uses the singular value decomposition of the response matrix in order to overcome the wildly oscillating solutions emerging from solving the system of linear equations that derive from equation 9.1. It contains one regularisation parameter, τ, with the best choice being the one yielding the smallest χ^2 between the test and the unfolded distributions.

4. Hit Backspace Once More, (HBOM) [5]: A model-independent, (potentially) data-driven method that applies a detector effects parameterisation iterative to observed data, thus unfolding by extrapolating them to a detector effect of zero. Developed by Monk and Oropeza-Barrera, it does not depend on a particular Physics model nor bin optimisation (in order to avoid migration effects).

5. TUnfold [6]: Developed by Sebastian Schmitt, this method is based on a least-square fit that used the Tikhonov regularisation and an optional area constraint. One regularisation parameter is present and for the determination of it's strength the L-curve method, along with global correlation coefficients scans are used.

[1] $f(\Delta x, \sigma, \lambda)$ where Δx is defined as the absolute deviation between data and simulation in a given bin, with respect to the corresponding error σ and λ is the regularisation parameter.

6. Bin-by-bin: The simplest of the unfolding methods[2] that uses MC, both fully simulated and not, in order to extract factors with which data bins are corrected. Correlations between bins are ignored; the method yields the smaller uncertainties than any other unfolding method but it depends heavily on the MC description.

In this analysis, among the plethora of methods available, the method of choice is D'Agostini's Iterative Bayesian, for the following reasons:

- The mathematical treatment of the response matrix, as the collection of probabilities of measured data given the true data, avoids the 'direct attack' of finding $\mathbf{A}^{-1}$.
- It is very fast, allowing uncertainties to be computed via ToyMC pseudo-experiments in reasonable time O(min).
- It is already implemented in the `RooUnfold` [7] framework.
- There is only one regularisation parameter, the number of iterations and the regularisation process is straight-forward.
- Dependence of the posterior (output of an iteration during unfolding) on the prior (input distribution) is negligible.

9.2 Work-flow and inputs to the unfolding process

The unfolding process begins with the construction of the response (migration) matrix that contains the description of the detector effects. It is a two-dimensional histogram filled with the `True` vs `Reconstructed` values of the observable of interest, which in this analysis is the differential distribution of the Z p_{T}. The response matrix is constructed from MC simulated events. For this purpose, starting from the true level objects in the signal MC before simulation (generator level), a cut-based selection is imposed so that the particular analysis phase-space is constructed, obtaining the `Truth` level observable of interest. Then the analysis proceeds at reconstruction level, where the relevant quantities are extracted.

[2] Actually there is quite a lot of dispute among statistician *gurus* within the ATLAS experiment on whether it should be called an *unfolding* method at the first place!

In general, the unfolding procedure can be viewed as a three-step process: initially, the estimated background is subtracted from data and fiducial factors are applied in order to correct for the number of events that fall out of the detector phase-space. Then the inversion of the response matrix takes place while in the final step, efficiency factors are applied to account for the detector's imperfect efficiency. The whole process is pictorially represented in Figure 9.1.

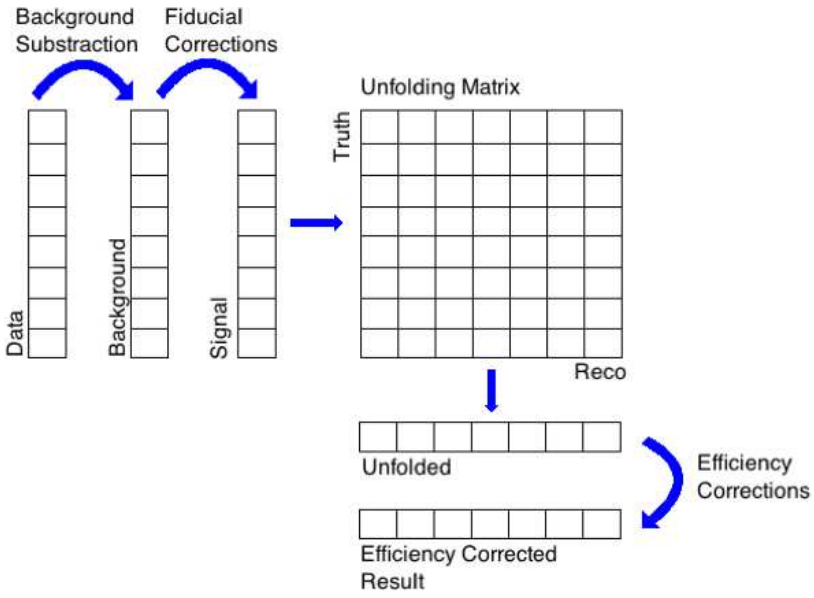

Figure 9.1: Schematic view of the unfolding procedure. Fiducial corrections are applied to the signal yield before the actual unfolding process. The result is corrected with efficiency factors.

Steering of the unfolding process, including correction factors, normalisation and uncertainties calculation and propagation is provided by the `EWUnfolding` framework [8]. It is a wrapper around the `RooUnfold` framework, providing an interface to all the unfolding methods implemented along with functions for calculating and propagating uncertainties through the usage of ToyMC pseudo-experiments (a more detailed description of how uncertainties related to the unfolding process are treated is given in the next section).

The `EWUnfolding` framework uses as inputs either histograms or `ROOT` trees, containing the necessary variables. In this analysis the histogram implementation is used and the inputs include the following one-dimentional histograms:

- **fiducialCorrectionNumerator:** It is filled with the reconstructed value of the

Z p_{T} if the event is successfully reconstructed and if at the generator-level analysis it passes all phase-space cuts;

- **fiducialCorrectionDenominator:** Same as the numerator, without the generator-level requirement.

- **efficiencyCorrectionNumerator:** Same as the fiducial correction numerator, but filled with the generated Z p_{T} (instead of the reconstructed value).

- **efficiencyCorrectionDenominator:** There is only one requirement, that the event falls in the fiducial phase-space in the generator-level analysis. Then the histogram is filled with the generated Z p_{T}.

- **purityNumerator:** Same as the fiducial correction numerator, but with the extra requirement that the Z p_{T} at generator and reconstructed levels fall into the same bin.

- **purityDenominator:** Same as the efficiency correction numerator.

- **stabilityNumerator:** Same as the fiducial correction denominator, but filled with the generated Z p_{T}.

9.3 Uncertainties treatment

ToyMC pseudo-experiments are used in order to evaluate the statistical uncertainty of the unfolding procedure. For each iteration a the data distribution is Poisson-fluctuated and then nominal unfolding is performed. The procedure is repeated 2000 times and the RMS of the resulting distribution is quoted as the statistical uncertainty of data after unfolding.

The statistical uncertainty on the amount of subtracted background events is estimated by using the same technique. The number of subtracted background events in each bin of the distribution is randomly fluctuated within a Gaussian of width equal to the statistical error on the number of background events in the bin. Gaussian fluctuations instead of Poisson fluctuations are used here because the expected number of background events in each bin is estimated using weighted MC events. The statistical uncertainty of the signal MC event sample is propagated by varying the value of each bin of the response

matrix randomly in a Gaussian of width corresponding the the statistical uncertainty of the bin. The new response matrix is used to repeat the unfolding procedure. The histogram of efficiency for signal MC events is also varied with the same procedure. The procedure is repeated 2000 times and the RMS of the resulting distribution is quoted as the statistical uncertainty from the signal MC events.

For the systematic uncertainties, a unique input file is produced for each of the systematics under consideration (be it scale, efficiency, resolution or theory variation). The unfolding procedure is repeated and the (maximum) difference from the nominal unfolding is quoted as the uncertainty. Also, for each of the systematic uncertainties, a corresponding covariance matrix is calculated, defined by:

$$Cov_{i,j} = \delta_i^{sys} \times \delta_j^{sys} \tag{9.3}$$

The global correlation matrix can be defined from the linear addition of the various covariance matrices:

$$C_{i,j} = \frac{Cov_{i,j}}{\sqrt{Cov_{i,i}}\sqrt{Cov_{j,j}}} \tag{9.4}$$

9.4 Application in the $W^{\pm}Z$ analysis

For the measurements of normalised differential distributions, all four decay channels, eee, $e\mu\mu$, μee, $\mu\mu\mu$, are added together. The response matrix is then constructed using a full simulated MC signal sample containing all four topologies. The POWHEG+PYTHIAMC event sample is used. An event is accounted for if it is reconstructed and inside the fiducial phase space. At truth level, "dressed" leptons are used, i.e gather all photons in a cone of $\delta R = 0.1$ around the lepton to account for FSR radiation.

9.5 Results

The following binning scheme is used for the measurement of the normalised differential p_T^Z measurement: (0-30), (30-60), (60-90), (90-120), (120-150), (150-220) (220-2000). In this binning scheme there is a small difference with respect to the binning scheme used in the previous publication at 7 TeV: The limits of the last two bins [(150-180), (180-2000)] have been switched to [(150-220), (220-2000)], allowing us to retain the shape of the p_T^Z

distribution while reducing the (large) uncertainty in the (150-180) bin. From Figure 9.2 it is evident that the migration is very low, at the order of 7.5% on average. The purity in Figure 9.2 is defined as a ratio of histograms, with the numerator calculated only from the diagonal elements of the response matrix, while the denominator includes all the events that are both reconstructed and within the fiducial volume. Unlike the response matrix, it does not include the bin migrations effects of events around the boundaries defining the fiducial phase space.

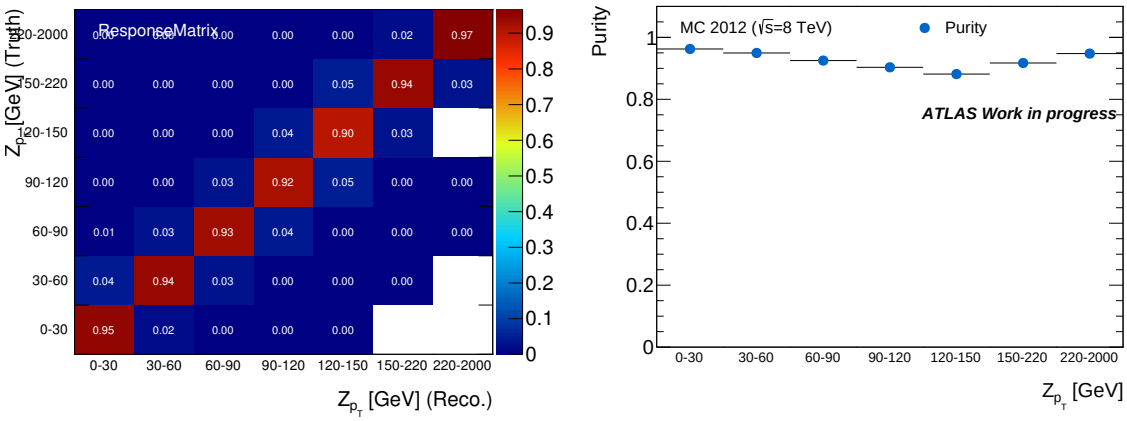

Figure 9.2: Response matrix (left) and purity (right).

Table 9.1 presents the data and total background yields per bin. The data and background distributions along with the unfolded distribution using the `EWUnfold` package are shown in Figure 9.3, while Figure 9.4 shows the absolute and relative uncertainties plot. On the plot of the unfolded distribution the MC prediction along with the total uncertainty are also shown. Finally, a closure test where the MC prediction is used instead of the data and the unfolding procedure is repeated is shown in Figure 9.5.

Bin	Data	Background
0-30	472	110.25
30-60	728	144.21
60-90	390	94.16
90-120	220	44.71
120-150	122	18.85
150-220	103	17.17
220-2000	56	9.32

Table 9.1: Data and total background yields per bin.

In Table 9.2 the results are presented along with their uncertainties.

Bin	0 - 30	30 - 60	60 - 90	90 - 120	120 - 150	150 - 220	220 - 2000
Results	0.2118	0.3575	0.1801	0.1083	0.06334	0.05117	0.02779
Comb. Unc.	(5.69%)	(4.10%)	(6.67%)	(9.09%)	(11.2%)	(12.6%)	(16.3%)
Stat. Unc.	(5.57%)	(4.05%)	(6.59%)	(9.00%)	(11.1%)	(12.5%)	(16.1%)
Sys. Unc.	(0.70%)	(0.22%)	(0.30%)	(0.40%)	(0.91%)	(0.96%)	(2.04%)
Bkg. Unc.	(0.91%)	(0.58%)	(1.00%)	(1.18%)	(1.20%)	(1.34%)	(1.25%)
Stat. Unc. (MC)	(0.18%)	(0.13%)	(0.20%)	(0.29%)	(0.41%)	(0.42%)	(0.63%)
MuonRecoSF	(0.00%)	(0.00%)	(0.00%)	(0.00%)	(0.00%)	(0.00%)	(0.00%)
MuonIsoSF	(0.00%)	(0.00%)	(0.00%)	(0.00%)	(0.06%)	(0.10%)	(0.14%)
MuonCScale	(-0.0%)	(0.00%)	(0.00%)	(0.00%)	(0.00%)	(0.07%)	(0.00%)
MuonIDSmearing	(0.00%)	(0.00%)	(0.00%)	(0.00%)	(-0.1%)	(-0.0%)	(0.00%)
MuonMSScaling	(0.43%)	(0.15%)	(-0.1%)	(-0.0%)	(-0.6%)	(-0.6%)	(-1.6%)
ElectronScaling	(-0.4%)	(0.00%)	(0.10%)	(0.15%)	(0.27%)	(0.48%)	(0.89%)
ElectronSmearing	(0.00%)	(0.00%)	(0.06%)	(0.00%)	(-0.1%)	(0.12%)	(0.00%)
ElectronRecoSF	(-0.1%)	(0.00%)	(0.00%)	(0.09%)	(0.12%)	(0.14%)	(0.16%)
ElectronIDSF	(-0.2%)	(0.00%)	(0.09%)	(0.14%)	(0.15%)	(0.19%)	(0.23%)
ElectronIsoSF	(0.00%)	(0.00%)	(0.00%)	(0.00%)	(0.00%)	(0.00%)	(0.00%)
LeptonTriggerSF	(0.00%)	(0.00%)	(0.00%)	(0.00%)	(0.00%)	(0.00%)	(-0.0%)
METRecoSoftTerms	(0.00%)	(0.00%)	(0.00%)	(0.00%)	(0.00%)	(0.00%)	(0.00%)
METScaleSoftTerms	(0.00%)	(0.00%)	(0.00%)	(0.00%)	(0.00%)	(0.00%)	(0.00%)
JER	(0.00%)	(0.00%)	(0.00%)	(0.06%)	(0.00%)	(-0.1%)	(0.09%)
JETEffectiveNP1	(0.00%)	(0.00%)	(0.00%)	(0.00%)	(0.00%)	(-0.0%)	(-0.1%)
JETEffectiveNP2	(0.00%)	(0.00%)	(0.00%)	(0.00%)	(-0.0%)	(0.00%)	(0.00%)
JETEffectiveNP3	(0.00%)	(0.00%)	(0.00%)	(0.00%)	(0.00%)	(0.00%)	(0.05%)
JETEffectiveNP4	(0.00%)	(0.00%)	(0.00%)	(0.00%)	(0.00%)	(0.00%)	(0.00%)
JETEffectiveNP5	(0.00%)	(0.00%)	(0.00%)	(0.00%)	(0.00%)	(0.00%)	(0.00%)
JETEffectiveNP6restTerm	(0.00%)	(0.00%)	(0.00%)	(0.00%)	(0.00%)	(0.00%)	(0.00%)
JETEtaIntercalibrationMod	(0.00%)	(0.00%)	(0.00%)	(0.00%)	(0.00%)	(-0.0%)	(-0.0%)
JETEtaIntercalibrationSta	(0.00%)	(0.00%)	(0.00%)	(0.00%)	(0.00%)	(0.00%)	(0.00%)
JETFlavourComp	(0.00%)	(0.00%)	(0.00%)	(0.08%)	(0.00%)	(-0.0%)	(0.00%)
JETFlavourResp	(0.00%)	(0.00%)	(0.00%)	(0.00%)	(0.00%)	(0.00%)	(0.00%)
JETNPVOffset	(0.00%)	(0.00%)	(0.00%)	(0.00%)	(0.00%)	(0.00%)	(0.00%)
JETMuOffset	(0.00%)	(0.00%)	(0.00%)	(0.00%)	(0.00%)	(0.00%)	(0.00%)
JETPt	(0.00%)	(0.00%)	(0.00%)	(0.00%)	(0.00%)	(0.00%)	(0.00%)
JETRho	(0.00%)	(0.00%)	(0.00%)	(0.00%)	(0.00%)	(0.00%)	(0.00%)
PileUp	(-0.0%)	(0.00%)	(0.00%)	(0.00%)	(0.19%)	(-0.0%)	(0.09%)

Table 9.2: Unfolding results and uncertainties. The total uncertainty shown is the quadratic sum of the statistical and the systematic uncertainty.

9.6 Estimation of the Z p_{T}-shape uncertainty.

For any unfolding method, the MC shape uncertainty of the observable under study can be estimated using a data-driven "closure test" [3]. The procedure followed was first introduced in [3] and the main points are as follows:

1. The signal MC truth distribution is compared to the raw data (before any background subtraction or unfolding) and it is reshaped by extracting per-bin data/MC factors;
2. The re-weighted truth MC distribution is folded using a folding matrix;
3. A reconstructed MC distribution is then obtained from the folding matrix;
4. The unfolding procedure is repeated using as inputs the reconstructed MC distribution from step 3 and the Nominal response matrix;
5. The difference between the unfolded reconstructed MC and the re-weighted truth MC distributions is to be quoted as the systematic uncertainty of the MC shape;

There are two delicate points during this procedure:

- The per-bin weighting factors, particularly in situations with very low populated bins (or even empty in some cases), should be extracted using a smoothing function. However, in this analysis there are sufficient entries in each bin so that a direct comparison of the data and MC distributions for the extraction of the aforementioned weights is feasible;
- In order to test the sensitivity of the unfolding method to statistical fluctuations in the MC, the folding matrix is derived from the original response matrix, after introducing statistical fluctuations (Poisson) in each bin;

Figure 9.6 shows the folding matrix used (along with the Nominal response matrix from which it derives, before the latter is normalised), while Table 9.3 contains the weighting factors over the binning scheme used in this analysis.

[3] The term closure test is used in quote marks here because a real closure test is expected to present no disagreement. In this case, whichever deviation in the final result is quoted as the uncertainty, hence the usage of the quote marks.

Bin	0 - 30	30 - 60	60 - 90	90 - 120	120 - 150	150 - 220	220 - 2000
Weight	1.52288	1.62159	1.44981	1.59348	1.73819	1.553	1.79533

Table 9.3: Per-bin weighting factors extracted as the data/MC truth distributions ratio.

overall good, yielding an average difference between the unfolded re-weighted reconstructed MC and the re-weighted truth MC distributions which is at the order of 4%, calculated as the arithmetic mean of the differences in all seven bins. However, this result is mainly driven by the difference in the last bin, which rises up to 13.65 %. This last bin, extending from 220 GeV up to infinity, is the least populated bin and therefore there is a statistical component in the uncertainty mentioned above. If it is left out, then the average deviation falls down to 2.44 %. Table 9.4 contains the uncertainties per-bin as calculated by the shape-dependence uncertainty estimation procedure.

Bin	0 - 30	30 - 60	60 - 90	90 - 120	120 - 150	150 - 220	220 - 2000
Uncertainty (%)	1.21	1.20	0.37	2.62	4.02	5.20	13.65

Table 9.4: Per-bin uncertainties estimated by the shape-dependence procedure. The final result is driven by the last bin.

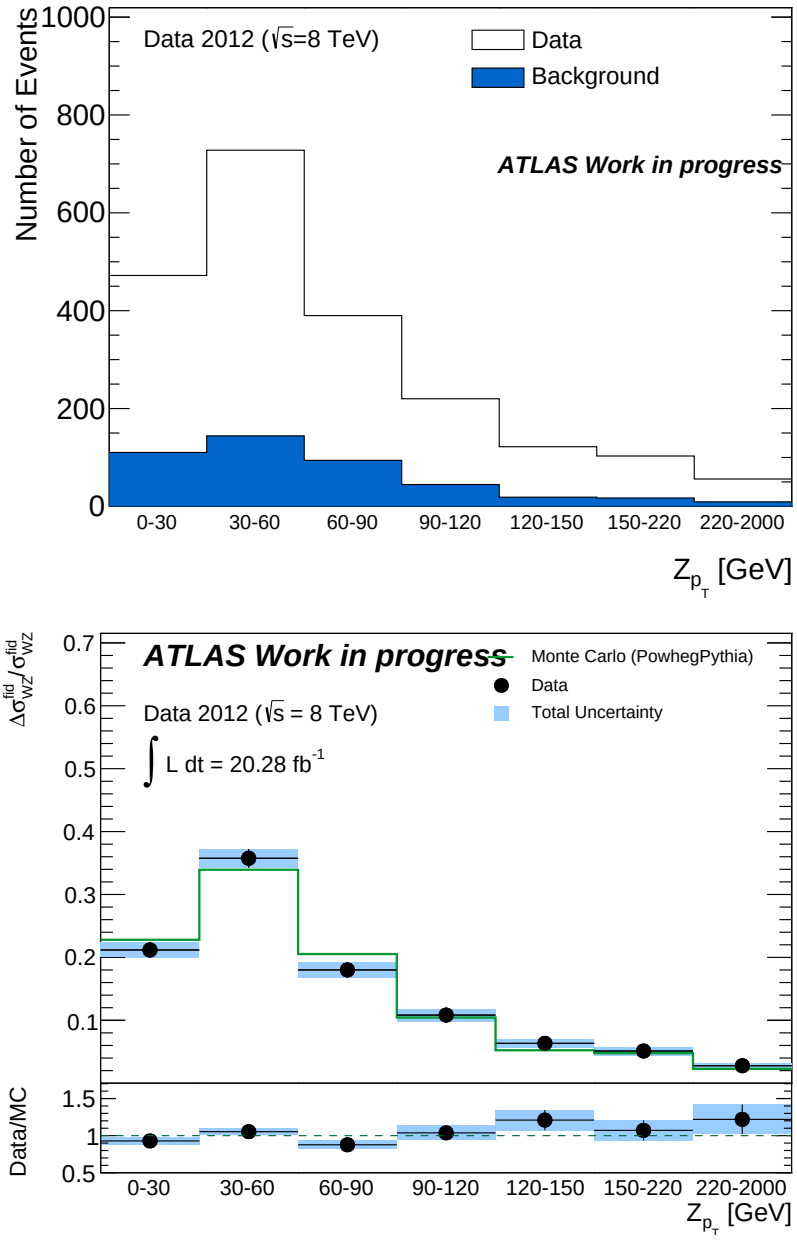

Figure 9.3: Data and background yields (top). Final unfolded distribution using `EWUnfold`. The band is the total uncertainty, green is the MC prediction, black points are data (bottom).

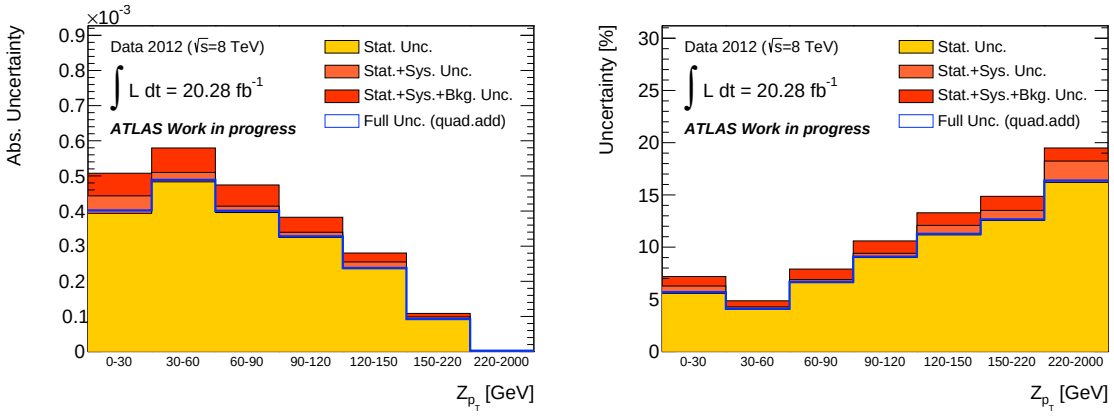

Figure 9.4: Absolute (left) and relative (right) uncertainties of the unfolding.

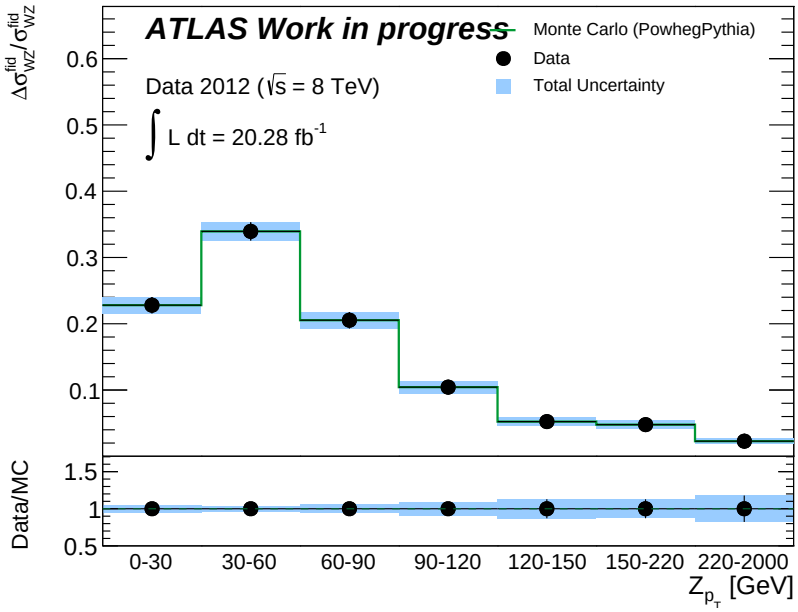

Figure 9.5: Closure test. The MC prediction is used as input instead of the data. The perfect agreement between "unfolded data" and the MC prediction verifies the solidity of the method. The band is the statistical uncertainty.

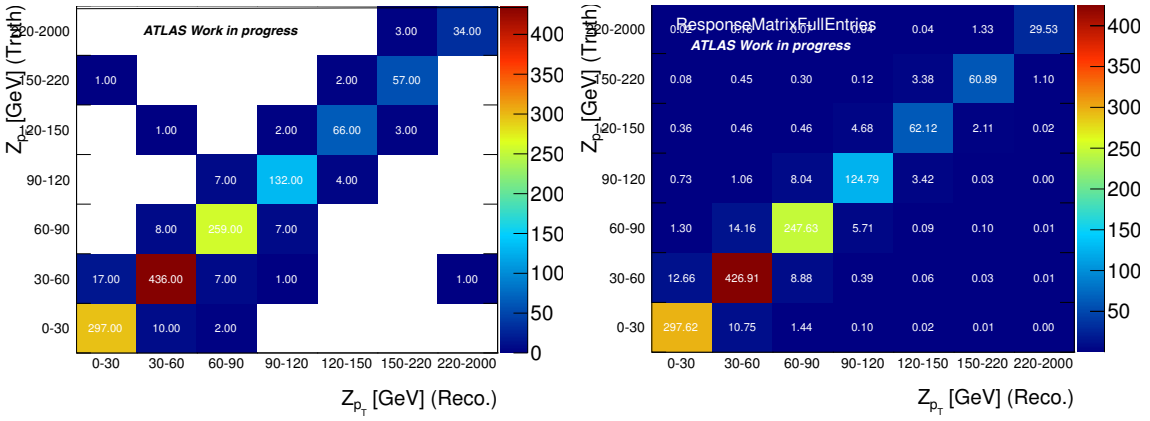

Figure 9.6: The folding matrix (left) and the Nominal response matrix, prior to any normalisation (right). The folding matrix derives from the Nominal response matrix after introducing (Poisson) statistical fluctuations in each bin.

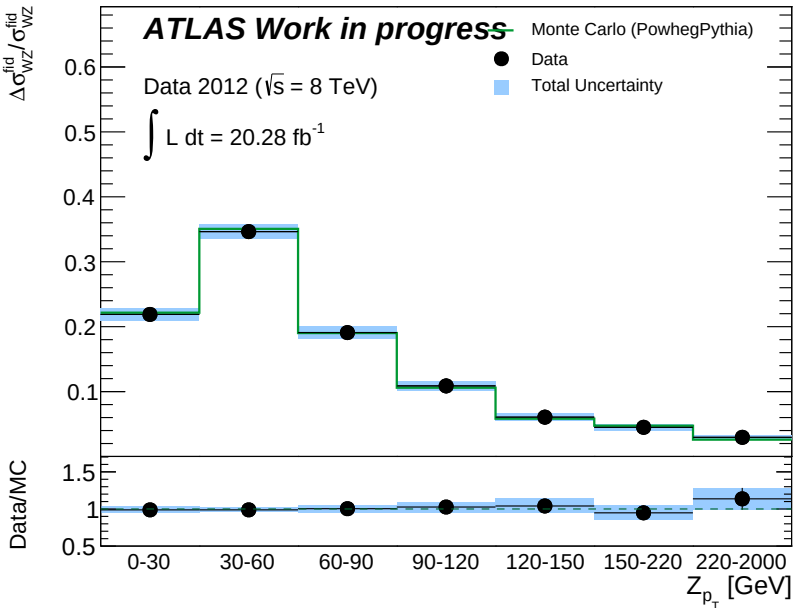

Figure 9.7: Unfolded distribution of the data-driven MC-shape uncertainty estimation "closure test". The uncertainty depicted by the blue band is the statistical uncertainty only. An excessive difference of 13.65% is found in the last bin alone.

Bibliography

[1] G. D'Agostini, *A Multidimensional unfolding method based on Bayes' theorem*, Nucl.Instrum.Meth. **A362** (1995) 487–498.

[2] L. B. Lucy, *An iterative technique for the rectification of observed distributions*, Astronomical Journal **79** (1974) 745.

[3] B. Malaescu, *An Iterative, Dynamically Stabilized(IDS) Method of Data Unfolding*, arXiv:1106.3107 [physics.data-an].

[4] A. Hocker and V. Kartvelishvili, *SVD approach to data unfolding*, Nucl.Instrum.Meth. **A372** (1996) 469–481, arXiv:hep-ph/9509307 [hep-ph].

[5] J. W. Monk and C. Oropeza-Barrera, *The HBOM Method for Unfolding Detector Effects*, Nucl.Instrum.Meth. **A701** (2013) 17–24, arXiv:1111.4896 [hep-ex].

[6] S. Schmitt, *TUnfold: an algorithm for correcting migration effects in high energy physics*, JINST **7** (2012) T10003, arXiv:1205.6201 [physics.data-an].

[7] T. Adye, *Unfolding algorithms and tests using RooUnfold*, arXiv:1105.1160 [physics.data-an].

[8] https://svnweb.cern.ch/trac/atlasphys/browser/Physics/StandardModel/ElectroWeak/Analyses/EWUnfolding/.

Chapter 10

Conclusions

With the recent discovery of the Higgs boson, the propagator of the Higgs field that generates the masses of the quarks and leptons and of the weak interaction bosons, the validity of the SM has been, once more, confirmed. In the forthcoming years, the LHC has a rich Physics potential to be unveiled, starting with the precision measurements of the Higgs boson, beyond SM searches are to be performed: SUperSymmetry (SUSY) is a promising and elegant theory and the potential discovery of the lightest supersymmetric particle is one of the main goals in the upcoming LHC Physics schedule.

My involvement with the ATLAS experiment began with the offline Data Quality Monitoring Framework (DQMF), the part of the ATLAS Data Quality Monitoring (DQM) core software that ensures the quality of the data, both in the online and the offline environment, through automated checks. I implemented a series of tests in the muon segment monitoring, the part of the offline monitoring that follows the segment finding reconstruction chain of the Muon Spectrometer. Several algorithms, that perform simple checks on histograms, were developed and are now part of the offline DQM software of the ATLAS experiment.

In order to achieve any of the LHC Physics goals, a good understanding of the "devices" it utilises, i.e the detectors surrounding the interaction points, is of very high importance. The total efficiency, ϵ, with which Physical objects are reconstructed is a crucial ingredient in numerous analyses, from performance to cross-section measurements and discoveries. This total efficiency can be broken down to its constituents which include lepton reconstruction, identification or isolation efficiency as well as the efficiency with which the trigger selected the events of interest. The method a performance group is going

to calculate the corresponding efficiency behind the scenes and provide it to the end-users performing the Physics analyses is Tag and Probe.

I was among the first people that developed the tag and probe method in the context of the ATLAS experiment, being it my authorship task. In that study, the reconstruction efficiency for CB muons was measured in the low-p_{T} region, using simulated di-muon events from J/ψ decays. The same study also utilized events from Υ decays, showing that the background contributions in the latter case were very hard to control, a fact that became apparent in the recent publication [1]. There the reconstruction and isolation efficiency and momentum resolution were calculated using 2010 data ($\sqrt{s}$=1.96 TeV) from J/ψ and Z decays to di-muon pairs, with the J/ψ candle used to probe the low-p_{T} region and the Z candle to access the 20 GeV $< p_{\mathrm{T}} <$ 100 GeV region. However, a gap in the efficiency in the region spanning from 10 GeV to 20 GeV verified the findings of our MC-based study, regarding the usage of the Υ candle for measuring efficiency with the tag and probe method, mainly due to the overlap of the three Υ states along with the difference in the mass resolution compared to the J/ψ candle.

My contribution in the data 2012 8 TeV full statistics $W^{\pm}Z$ analysis is manifold; Among others, I am mainly responsible for the unfolding of the differential distribution with respect to the p_{T} of the Z-boson. Limited acceptance, finite resolution and imperfect efficiency, collectively known as detector effects, distort the distributions of the measured observable. The procedure by which the detector effects can be removed, so that the measured distribution may be translated to one closer to the real, allowing thus cross-experiment comparisons of results, is known in High Energy Physics as *unfolding* (or unsmearing or deconvolution) and in its core it deals with solving the linear equation:

$$\mathbf{y} = \mathbf{A} \cdot \mathbf{x}$$

where $\mathbf{A}$ is the response matrix, which is obtained from MC and it describes the detector effects, $\mathbf{x}$ is the true spectrum (the goal of the unfolding process) and $\mathbf{y}$ the measured one. This is an inverse problem and it is, mathematically speaking, difficult and ill-posed. Among the plethora of methods that have been developed for this purpose, the Bayesian iterative (with 3 iterations) was chosen and it was used under the `RooUnfold` framework and the `EWUNFOLD` wrapper. A closure test verified the impeccable performance of the method and a "data-driven" procedure in order to estimate the uncertainty due to the description of

the Z-boson p_{T}-shape in MC was tested.

I was also responsible for the optimisation of the W-muon isolation criteria, resulting in the tightening of the track-based isolation to 10% (from 15%). This choice was driven by the need to retain as much signal yield as possible while still maximizing the background rejection. Finally, in this analysis the previous measurement [2] of the $W^{\pm}Z$ cross-section was updated and the fiducial cross-section was measured to be:

$$\sigma_{WZ}^{fid} = 34.56^{+0.93}_{-0.92}(stat.)^{+0.61}_{-0.50}(syst.)^{+1.09}_{-1.02}(lumi.)\text{fb}$$

and the total cross-section:

$$\sigma_{WZ}^{tot} = 23.89^{+0.64}_{-0.63}(stat.)^{+0.43}_{-0.36}(syst.)^{+0.75}_{-0.72}(lumi.)\text{ pb}$$

with the SM expectation from [3] of: $\sigma_{W^{\pm}Z}$=22.7±2.7 pb.

Bibliography

[1] ATLAS Collaboration Collaboration, G. Aad et al., *Muon reconstruction efficiency and momentum resolution of the ATLAS experiment in proton-proton collisions at* $\sqrt{s}$*=7 TeV in 2010*, arXiv:1404.4562 [hep-ex].

[2] ATLAS Collaboration, *A Measurement of WZ Production in Proton-Proton Collisions at* $\sqrt{(s)} = 8$ *TeV with the ATLAS Detector*, ATLAS Note (2013). https://cds.cern.ch/record/1525557?ln=en.

[3] J. Baglio, L. D. Ninh, and M. M. Weber, *Massive gauge boson pair production at the LHC: a next-to-leading order story*, Phys.Rev. **D88** (2013) 113005, arXiv:1307.4331.

Appendix A

List of MC samples used in the Tag and Probe feasibility study

MCID	Process	Generator	Events	Cross-section [nb]
108407	pp $\rightarrow J/\psi \rightarrow \mu 4\mu 4$	Pythia	149901	30
108411	$b\bar{b} \rightarrow J/\psi \rightarrow \mu 4\mu 4X$	PythiaB	49847	13.5
108423	pp $\rightarrow \Upsilon(1S) \rightarrow \mu 2.4\mu 2.5$	Pythia	199351	78
108401	$b\bar{b} \rightarrow \mu 4X$	PythiaB	99918	13170
108400	$c\bar{c} \rightarrow \mu 4X$	PythiaB	69971	7900
106004	pp $\rightarrow DY \rightarrow \mu 2.5\mu 2.5X$	Pythia	249945	5

Table A.1: The MC samples used in the Tag and Probe feasibility study. The MCID, production processes, cross-sections and numbers of fully simulated MC events are listed.

Appendix B

MC Samples in the 8 TeV $W^{\pm}Z$ analysis

MCID	Process	Generator	Events	k-factor	ϵ_{filter}	Cross-section [pb]
129877	$W^+Z \to e\nu ee$	POWHEG+PYTHIA	50000	1	1	0.0788611
129878	$W^+Z \to e\nu\mu\mu$	POWHEG+PYTHIA	49999	1	1	0.0524164
129879	$W^+Z \to e\nu\tau\tau$	POWHEG+PYTHIA	50000	1	1	0.0524164
129880	$W^+Z \to \mu\nu ee$	POWHEG+PYTHIA	50000	1	1	0.0524162
129881	$W^+Z \to \mu\nu\mu\mu$	POWHEG+PYTHIA	50000	1	1	0.0788659
129882	$W^+Z \to \mu\nu\tau\tau$	POWHEG+PYTHIA	50000	1	1	0.0524162
129883	$W^+Z \to \tau\nu ee$	POWHEG+PYTHIA	50000	1	1	0.052414
129884	$W^+Z \to \tau\nu\mu\mu$	POWHEG+PYTHIA	49900	1	1	0.052414
129885	$W^+Z \to \tau\nu\tau\tau$	POWHEG+PYTHIA	50000	1	1	0.0796506
129886	$W^-Z \to e\nu ee$	POWHEG+PYTHIA	50000	1	1	0.0467166
129887	$W^-Z \to e\nu\mu\mu$	POWHEG+PYTHIA	50000	1	1	0.0297652
129888	$W^-Z \to e\nu\tau\tau$	POWHEG+PYTHIA	50000	1	1	0.0297652
129889	$W^-Z \to \mu\nu ee$	POWHEG+PYTHIA	50000	1	1	0.0297652
129890	$W^-Z \to \mu\nu\mu\mu$	POWHEG+PYTHIA	50000	1	1	0.0467179
129891	$W^-Z \to \mu\nu\tau\tau$	POWHEG+PYTHIA	50000	1	1	0.0297652
129892	$W^-Z \to \tau\nu ee$	POWHEG+PYTHIA	50000	1	1	0.0297645
129893	$W^-Z \to \tau\nu\mu\mu$	POWHEG+PYTHIA	49900	1	1	0.0297645
129894	$W^-Z \to \tau\nu\tau\tau$	POWHEG+PYTHIA	50000	1	1	0.047194

Table B.1: The $W^{\pm}Z$ signal production processes, cross-sections and numbers of fully simulated MC events. The MC simulation filter is an event selection at the generator level. The corresponding filter efficiencies are given in the table. The listed cross sections do not include k-factors.

MCID	Process	Generator	Events	k-factor	ϵ_{filter}	Cross-section [pb]
126893	$W^{\pm}Z \to \ell^{\pm}\nu\ell^+\ell^-$	SHERPA	2699893	1.0	1	9.757
147194	$W^{\pm}Z \to \ell^{\pm}\nu\ell^+\ell^-$	SHERPA	199999	1.0	1	0.07296
147197	$W^{\pm}Z \to \ell^{\pm}\nu\ell^+\ell^-$	SHERPA (WZ$\to$ lllν jj)	5998980	1.0	0.274	9.757

Table B.2: SHERPA $W^{\pm}Z$ signal MC samples.

MCID	Process	Generator	Events	k-factor	ϵ_{filter}	Cross-section [pb]
117360	t-channel→e	AcerMCPythia	299999	1	1	9.48
117361	t-channel→ μ	AcerMCPythia	299999	1	1	9.48
117362	t-channel→ τ	AcerMCPythia	299999	1	1	9.48
108343	s-channel→e	MC@NLO	199999	1	1	0.564
108344	s-channel→ μ	MC@NLO	200000	1	1	0.564
108345	s-channel→ τ	MC@NLO	199900	1	1	0.564
110001	$t\bar{t}$	MC@NLO	9988449	1.2177	1	21.81
119353	$t\bar{t}W$	Madgraph Pythia	399997	1.18	1	0.1041
119354	$t\bar{t}W$j	Madgraph Pythia	399896	1.18	1	0.0932
119355	$t\bar{t}Z$	Madgraph Pythia	399996	1.34	1	0.06769
119356	$t\bar{t}Z$j	Madgraph Pythia	399895	1.34	1	0.0874

Table B.3: Single-top, $t\bar{t}$ and $t\bar{t}$+W/Z MC samples.

MCID	Process	Generator	Events	k-factor	ϵ_{filter}	Cross-section [pb]
126928	$W^+W^- \to ee$	Powheg+Pythia	299700	1	1	0.62
126929	$W^+W^- \to \mu e$	Powheg+Pythia	300000	1	1	0.62
126930	$W^+W^- \to \tau e$	Powheg+Pythia	299999	1	1	0.62
126931	$W^+W^- \to e\mu$	Powheg+Pythia	299999	1	1	0.62
126932	$W^+W^- \to \mu\mu$	Powheg+Pythia	300000	1	1	0.62
126933	$W^+W^- \to \tau\mu$	Powheg+Pythia	300000	1	1	0.62
126934	$W^+W^- \to e\tau$	Powheg+Pythia	299996	1	1	0.62
126935	$W^+W^- \to \mu\tau$	Powheg+Pythia	299999	1	1	0.62
126936	$W^+W^- \to \tau\tau$	Powheg+Pythia	299999	1	1	0.62
169471	$W^+W^- \to ee$	gg2wwJimmy	30000	1	1	0.017
169472	$W^+W^- \to e\mu$	gg2wwJimmy	30000	1	1	0.017
169473	$W^+W^- \to e\tau$	gg2wwJimmy	30000	1	1	0.017
169474	$W^+W^- \to \mu\mu$	gg2wwJimmy	30000	1	1	0.017
169475	$W^+W^- \to \mu e$	gg2wwJimmy	30000	1	1	0.017
169476	$W^+W^- \to \mu\tau$	gg2wwJimmy	30000	1	1	0.017
169477	$W^+W^- \to \tau\tau$	gg2wwJimmy	30000	1	1	0.017
169478	$W^+W^- \to \tau e$	gg2wwJimmy	30000	1	1	0.017
169479	$W^+W^- \to \tau\mu$	gg2wwJimmy	30000	1	1	0.017

Table B.4: $W^{\pm}W^{\mp}$ MC samples.

MCID	Process	Generator	Events	k-factor	ϵ_{filter}	Cross-section [pb]
117680	$We\nu Np0$	Alpgen+Pythia	3459993	1.19	1.0	8136.8
117681	$We\nu Np1$	Alpgen+Pythia	2499997	1.19	1.0	1791.5
117682	$We\nu Np2$	Alpgen+Pythia	3768693	1.19	1.0	541.6
117683	$We\nu Np3$	Alpgen+Pythia	1009998	1.19	1.0	146.65
117684	$We\nu Np4$	Alpgen+Pythia	249898	1.19	1.0	37.334
117685	$We\nu Np5$	Alpgen+Pythia	69997	1.19	1.0	11.355
147025	$We\nu Np0$	Alpgen+Pythia	9494882	1.18	1.0	8126.9
147026	$We\nu Np1$	Alpgen+Pythia	26298052	1.18	1.0	1792.9
147027	$We\nu Np2$	Alpgen+Pythia	17569347	1.18	1.0	542.3
147028	$We\nu Np3$	Alpgen+Pythia	4985287	1.18	1.0	147.66
147029	$We\nu Np4$	Alpgen+Pythia	2553792	1.18	1.0	37.751
147030	$We\nu Np5$	Alpgen+Pythia	799192	1.18	1.0	11.916
117690	$W\mu\nu Np0$	Alpgen+Pythia	3469998	1.19	1.0	8133.4
117691	$W\mu\nu Np1$	Alpgen+Pythia	2499892	1.19	1.0	1792.7
117692	$W\mu\nu Np2$	Alpgen+Pythia	3769294	1.19	1.0	541.27
117693	$W\mu\nu Np3$	Alpgen+Pythia	1009996	1.19	1.0	146.49
117694	$W\mu\nu Np4$	Alpgen+Pythia	255000	1.19	1.0	37.341
117695	$W\mu\nu Np5$	Alpgen+Pythia	65000	1.19	1.0	11.364
147033	$W\mu\nu Np0$	Alpgen+Pythia	11999285	1.18	1.0	8127.2
147034	$W\mu\nu Np1$	Alpgen+Pythia	26291747	1.18	1.0	1792.8
147035	$W\mu\nu Np2$	Alpgen+Pythia	17611454	1.18	1.0	542.42
147036	$W\mu\nu Np3$	Alpgen+Pythia	4986077	1.18	1.0	147.68
147037	$W\mu\nu Np4$	Alpgen+Pythia	2556595	1.18	1.0	37.76
147038	$W\mu\nu Np5$	Alpgen+Pythia	798898	1.18	1.0	11.934
117700	$W\tau\nu Np0$	Alpgen+Pythia	3419993	1.19	1.0	8135.7
117701	$W\tau\nu Np1$	Alpgen+Pythia	2499995	1.19	1.0	1793.7
117702	$W\tau\nu Np2$	Alpgen+Pythia	3769998	1.19	1.0	541.24
117703	$W\tau\nu Np3$	Alpgen+Pythia	1009994	1.19	1.0	146.48
117704	$W\tau\nu Np4$	Alpgen+Pythia	250000	1.19	1.0	37.344
117705	$W\tau\nu Np5$	Alpgen+Pythia	65000	1.19	1.0	11.477
147041	$W\tau\nu Np0$	Alpgen+Pythia	9498284	1.18	1.0	8126.0
147042	$W\tau\nu Np1$	Alpgen+Pythia	26298935	1.18	1.0	1792.5
147043	$W\tau\nu Np2$	Alpgen+Pythia	17601943	1.18	1.0	542.21
147044	$W\tau\nu Np3$	Alpgen+Pythia	4987982	1.18	1.0	147.61
147045	$W\tau\nu Np4$	Alpgen+Pythia	2558295	1.18	1.0	37.738
147046	$W\tau\nu Np5$	Alpgen+Pythia	799096	1.18	1.0	11.905

Table B.5: $W + jets$ MC samples.

MCID	Process	Generator	Events	k-factor	ϵ_{filter}	Cross-section [pb]
147770	$Z \to ee$	SHERPA	9999162	1	1	1241.2
147771	$Z \to \mu\mu$	SHERPA	9998983	1	1	1241.2
147772	$Z \to \tau\tau$	SHERPA	4999989	1	1	1241.2

Table B.6: Z+jets SHERPA MC samples.

MCID	Process	Generator	Events	k-factor	ϵ_{filter}	Cross-section [pb]
117650	$Ze\nu Np0$	ALPGEN+PYTHIA	6619984	1.18	1.0	718.89
117651	$Ze\nu Np1$	ALPGEN+PYTHIA	1329498	1.18	1.0	175.6
117652	$Ze\nu Np2$	ALPGEN+PYTHIA	404998	1.18	1.0	58.849
117653	$Ze\nu Np3$	ALPGEN+PYTHIA	109999	1.18	1.0	15.56
117654	$Ze\nu Np4$	ALPGEN+PYTHIA	30000	1.18	1.0	3.9322
117655	$Ze\nu Np5$	ALPGEN+PYTHIA	10000	1.18	1.0	1.1994
147105	$Ze\nu Np0$	ALPGEN+PYTHIA	6298988	1.19	1.0	718.97
147106	$Ze\nu Np1$	ALPGEN+PYTHIA	8199476	1.19	1.0	175.70
147107	$Ze\nu Np2$	ALPGEN+PYTHIA	3175991	1.19	1.0	58.875
147108	$Ze\nu Np3$	ALPGEN+PYTHIA	894995	1.19	1.0	15.636
147109	$Ze\nu Np4$	ALPGEN+PYTHIA	398597	1.19	1.0	4.0116
147110	$Ze\nu Np5$	ALPGEN+PYTHIA	229700	1.19	1.0	1.2592
117660	$Z\mu\nu Np0$	ALPGEN+PYTHIA	6608490	1.18	1.0	718.91
117661	$Z\mu\nu Np1$	ALPGEN+PYTHIA	1334697	1.18	1.0	175.81
117662	$Z\mu\nu Np2$	ALPGEN+PYTHIA	404995	1.18	1.0	58.805
117663	$Z\mu\nu Np3$	ALPGEN+PYTHIA	110000	1.18	1.0	15.589
117664	$Z\mu\nu Np4$	ALPGEN+PYTHIA	30000	1.18	1.0	3.9072
117665	$Z\mu\nu Np5$	ALPGEN+PYTHIA	10000	1.18	1.0	1.1933
147113	$Z\mu\nu Np0$	ALPGEN+PYTHIA	6298796	1.19	1.0	719.16
147114	$Z\mu\nu Np1$	ALPGEN+PYTHIA	8198384	1.19	1.0	175.74
147115	$Z\mu\nu Np2$	ALPGEN+PYTHIA	3175488	1.19	1.0	58.882
147116	$Z\mu\nu Np3$	ALPGEN+PYTHIA	894799	1.19	1.0	15.673
147117	$Z\mu\nu Np4$	ALPGEN+PYTHIA	398200	1.19	1.0	4.0057
147118	$Z\mu\nu Np5$	ALPGEN+PYTHIA	229200	1.19	1.0	1.2544
117670	$Z\tau\nu Np0$	ALPGEN+PYTHIA	6615490	1.18	1.0	718.85
117671	$Z\tau\nu Np1$	ALPGEN+PYTHIA	1334998	1.18	1.0	175.83
117672	$Z\tau\nu Np2$	ALPGEN+PYTHIA	405000	1.18	1.0	58.63
117673	$Z\tau\nu Np3$	ALPGEN+PYTHIA	108999	1.18	1.0	15.508
117674	$Z\tau\nu Np4$	ALPGEN+PYTHIA	108999	1.18	1.0	3.9526
117675	$Z\tau\nu Np5$	ALPGEN+PYTHIA	10000	1.18	1.0	1.1805
147121	$Z\tau\nu Np0$	ALPGEN+PYTHIA	6299885	1.19	1.0	718.87
147122	$Z\tau\nu Np1$	ALPGEN+PYTHIA	8199883	1.19	1.0	175.76
147123	$Z\tau\nu Np2$	ALPGEN+PYTHIA	3174895	1.19	1.0	58.856
147124	$Z\tau\nu Np3$	ALPGEN+PYTHIA	894995	1.19	1.0	15.667
147125	$Z\tau\nu Np4$	ALPGEN+PYTHIA	894995	1.19	1.0	4.0121
147126	$Z\tau\nu Np5$	ALPGEN+PYTHIA	229799	1.19	1.0	1.256

Table B.7: Z+jets ALPGEN+PYTHIA MC samples.

MCID	Process	Generator	Events	k-factor	ϵ_{filter}	Cross-section [pb]
116601	$ZZ \to e^+e^-e^+e^-$	$gg2ZZ$	90000	1	1	0.000675
116602	$ZZ \to \mu^+\mu^-\mu^+\mu^-$	$gg2ZZ$	89699	1	1	0.000675
116603	$ZZ \to e^+e^-\mu^+\mu^-$	$gg2ZZ$	89699	1	1	0.00134539
126937	$ZZ \to e^+e^-e^+e^-$	Powheg+Pythia	1099997	1	0.9077	0.0769
126938	$ZZ \to e^+e^-\mu^+\mu^-$	Powheg+Pythia	1599696	1	0.8279	0.1756
126939	$ZZ \to e^+e^-\tau^+\tau^-$	Powheg+Pythia	1099897	1	0.5824	0.1754
126940	$ZZ \to \mu^+\mu^-\mu^+\mu^-$	Powheg+Pythia	1099798	1	0.91241	0.0768
126941	$ZZ \to \mu^+\mu^-\tau^+\tau^-$	Powheg+Pythia	1098999	1	0.5873	0.1754
126942	$ZZ \to \tau^+\tau^-\tau^+\tau^-$	Powheg+Pythia	300000	1	0.106	0.0769

Table B.8: ZZ MC samples.

MCID	Process	Generator	Events	k-factor	ϵ_{filter}	Cross-section [pb]
146430	$W\gamma Np0$	Alpgen/Jimmy	50000	1.15	1	230.09
146431	$W\gamma Np1$	Alpgen/Jimmy	50000	1.15	1	59.343
146432	$W\gamma Np2$	Alpgen/Jimmy	50000	1.15	1	21.469
146433	$W\gamma Np3$	Alpgen/Jimmy	49999	1.15	1	7.1032
146434	$W\gamma Np4$	Alpgen/Jimmy	60000	1.15	1	2.1224
146435	$W\gamma Np5$	Alpgen/Jimmy	364999	1.15	1	0.46612

Table B.9: $W\gamma$ MC samples.

MCID	Process	Generator	Events	k-factor	ϵ_{filter}	Cross-section [pb]
145161	$Z(e^+e^-)\gamma$	Sherpa	6189679	1	1	32.26
145162	$Z(\mu^+\mu^-)\gamma$	Sherpa	9198579	1	1	32.317
126854	$Z(\tau^+\tau^-)\gamma$	Sherpa	3999409	1	1	32.33

Table B.10: $Z\gamma$ MC samples.

MCID	Process	Generator	Events	k-factor	ϵ_{filter}	Cross-section [pb]
129895	$W^+(e)Z(e^+e^-)$	MC@NLO	-	1	1	0.0500215
129896	$W^+(e)Z(\mu^+\mu^-)$	MC@NLO	-	1	1	0.0500215
129897	$W^+(e)Z(\tau^+\tau^-)$	MC@NLO	-	1	1	0.0500215
129898	$W^+(\mu)Z(e^+e^-)$	MC@NLO	-	1	1	0.0500215
129899	$W^+(\mu)Z(\mu^+\mu^-)$	MC@NLO	-	1	1	0.0500215
129900	$W^+(\mu)Z(\tau^+\tau^-)$	MC@NLO	-	1	1	0.0500215
129901	$W^+(\tau)Z(e^+e^-)$	MC@NLO	-	1	1	0.0500215
129902	$W^+(\tau)Z(\mu^+\mu^-)$	MC@NLO	-	1	1	0.0500215
129903	$W^+(\tau)Z(\tau^+\tau^-)$	MC@NLO	-	1	1	0.0500215
129904	$W^-(e)Z(e^+e^-)$	MC@NLO	-	1	1	0.028108
129905	$W^-(e)Z(\mu^+\mu^-)$	MC@NLO	-	1	1	0.028108
129906	$W^-(e)Z(\tau^+\tau^-)$	MC@NLO	-	1	1	0.028108
129907	$W^-(\mu)Z(e^+e^-)$	MC@NLO	-	1	1	0.028108
129908	$W^-(\mu)Z(\mu^+\mu^-)$	MC@NLO	-	1	1	0.028108
129909	$W^-(\mu)Z(\tau^+\tau^-)$	MC@NLO	-	1	1	0.028108
129910	$W^-(\tau)Z(e^+e^-)$	MC@NLO	-	1	1	0.028108
129911	$W^-(\tau)Z(\mu^+\mu^-)$	MC@NLO	-	1	1	0.028108
129912	$W^-(\tau)Z(\tau^+\tau^-)$	MC@NLO	-	1	1	0.028108

Table B.11: MC@NLO$W^{\pm}Z$ signal MC samples.

MCID	Process	Generator	Events	k-factor	ϵ_{filter}	Cross-section [pb]
119583	$t\bar{t}W^+W^-$	Madgraph Pythia	10000	2.0685	1	0.00091901
167006	WWW	Madgraph Pythia	50000	1	1	0.0050961
167007	ZWW	Madgraph Pythia	50000	1	1	0.0015546
167008	ZZZ	Madgraph Pythia	50000	1	1	0.00033239
181346	$W^+W^-\gamma$	Madgraph Pythia8	1200000	1	1	0.000005946

Table B.12: VVV MC samples.

MCID	Process	Generator	Events	k-factor	ϵ_{filter}	Cross-section [pb]
147280	$WW2\ell$	Pythia8	19900	1	0.48	0.0258
147282	$WZ2\ell$	Pythia8	20000	1	0.0539	0.139
147285	$ZZ2\ell$	Pythia8	799999	1	0.0539	0.213

Table B.13: VV DPS MC samples.

Appendix C

MCFM data card

```
'6.6'   [file version number]

[Flags to specify the mode in which MCFM is run]
.false.   [evtgen]
.false.   [creatent]
.false.   [skipnt]
.false.   [dswhisto]
.true.    [writetop]
.true.    [writedat]
.true.    [writegnu]
.true.    [writeroot]
.false.   [writepwg]

[General options to specify the process and execution]
76    [nproc]
'tota'    [part 'lord','real' or 'virt','tota']
'test'    ['runstring']
8000d0    [sqrts in GeV]
+1    [ih1 =1 for proton and -1 for antiproton]
+1    [ih2 =1 for proton and -1 for antiproton]
126d0   [hmass]
1.0d0   [scale:QCD scale choice]
1.0d0   [facscale:QCD fac_scale choice]
'm(3456)'   [dynamicscale]
.false.   [zerowidth]
.true.    [removebr]
10    [itmx1, number of iterations for pre-conditioning]
10000   [ncall1]
10    [itmx2, number of iterations for final run]
10000   [ncall2]
```

```
1089    [ij]
.false.   [dryrun]
.true.    [Qflag]
.true.    [Gflag]

[Heavy quark masses]
173.2d0   [top mass]
4.75d0    [bottom mass]
1.5d0   [charm mass]

[Pdf selection]
'CT10.00' [pdlabel]
4   [NGROUP, see PDFLIB]
46    [NSET - see PDFLIB]
CT10.LHgrid  [LHAPDF group]
-1             [LHAPDF set]

[Jet definition and event cuts]
0d0   [m34min]
8000d0    [m34max]
66.0d0    [m56min]
116.0d0   [m56max]
.true.    [inclusive]
'ankt'    [algorithm]
0d0   [ptjet_min]
0d0   [|etajet|_min]
4.7d0   [|etajet|_max]
0.5d0   [Rcut_jet]
.true.    [makecuts]
0d0   [ptlepton_min]
99d0    [|etalepton|_max]
0d0   [ptmin_missing]
0d0   [ptlepton(2nd+)_min]
99d0    [|etalepton(2nd+)|_max]
0d0   [minimum (3,4) transverse mass]
0d0   [R(jet,lept)_min]
0d0   [R(lept,lept)_min]
0d0   [Delta_eta(jet,jet)_min]
.false.   [jets_opphem]
0   [lepbtwnjets_scheme]
0d0             [ptmin_bjet]
99d0    [etamax_bjet]

[Settings for photon processes]
```

```
.false.         [fragmentation included]
'BFGsetII'       [fragmentation set]
80d0            [fragmentation scale]
20d0    [ptmin_photon]
2.5d0   [etamax_photon]
10d0    [ptmin_photon2]
0.7d0           [R(photon,lept)_min]
0.4d0           [R(photon,photon)_min]
0.7d0           [cone size for isolation]
0.4d0   [epsilon_h, energy fraction for isolation]

[Anomalous couplings of the W and Z]
0.0d0   [Delta_g1(Z)]
0.0d0   [Delta_K(Z)]
0.0d0   [Delta_K(gamma)]
0.0d0   [Lambda(Z)]
0.0d0   [Lambda(gamma)]
0.0d0   [h1(Z)]
0.0d0   [h1(gamma)]
0.0d0   [h2(Z)]
0.0d0   [h2(gamma)]
0.0d0   [h3(Z)]
0.0d0   [h3(gamma)]
0.0d0   [h4(Z)]
0.0d0   [h4(gamma)]
2.0d0   [Form-factor scale, in TeV]

[How to resume/save a run]
.false.   [readin]
.false.   [writeout]
''    [ingridfile]
''    [outgridfile]

[Technical parameters that should not normally be changed]
.false.   [debug]
.true.    [verbose]
.false.   [new_pspace]
.false.   [virtonly]
.false.   [realonly]
.true.    [spira]
.false.   [noglue]
.false.   [ggonly]
.false.   [gqonly]
.false.   [omitgg]
```

```
.false.   [vanillafiles]
1   [nmin]
2   [nmax]
.true.    [clustering]
.false.   [realwt]
0   [colourchoice]
1d-2    [rtsmin]
1d-4    [cutoff]
0.2d0   [aii]
0.2d0   [aif]
0.2d0   [afi]
1d0   [aff]
1d0             [bfi]
1d0             [bff]
```

Acknowledgements

Even though the protocol dictates otherwise, I will start with Christos Anastopoulos, my dearest friend from our M.Sc. years. There are so many moments over these past years to remember; I will just say "thank you for that coffee Christos", since it was the start of this journey for me. And thank you for being true all these years.

I would like to heartily thank my supervisor, Professor Spyros Tzamarias, for his guidance during the time of our collaboration. His expertise and deep understanding has been an unlimited source of knowledge and inspiration for me. Also from the Hellenic Open University I need to thank Lecturer Antonios Leisos, for his support and guidance during these years.

I would also like to thank Samira Hassani for her guidance during my early days in ATLAS. Thank you for all the advising and the knowledge I got from you in the time we worked together Samira. I would also like to thank here Dimitra Tsionou and Joany Andreina Manjarres Ramos for their valuable help (and patience) in showing me the first steps in FLIT.

Dinos Bachas, Ilectra Christidi, Ioannis Nomidis, Andreas Petridis, Apostolos Tsirigotis, Giorgos Bourlis, Vaso Kouskoura: I can't think of better co-workers. Ilectra thank you for your support and our conversations. Ioannis for the music, the fun, the beers, the fights, everything! Andreas, for the times in batiment 54. Dinos, I have learned so many things from you over these years and I am grateful I have worked with such a devoted and talented Physicist. Giorgos, Apostolos, Giannis thank you for the unforgettable, hard-working yet so much fun moments we shared in the HOU lab and for making Patra feel like home from the first day.

Assistant professor Dimos Sampsonidis you have been most supportive and caring. Going (way) back to the Atomic Physics labs where I first met you presenting the phenomena with your unique, cool style, up to the Physics analyses and the events we organised together, I have always enjoyed learning while working with you.

Assistant professor Kostas Kordas! "They say the darkest hour is right before the dawn" sang Bob Dylan. It was your arrival in the AUTh that re-motivated me when I needed it the most. It is your unmatched, authentic style as a speaker and your profound understanding of Physics that made working with you a wonderful experience. Thank you Kostas for being such a gifted teacher and speaker, you have been a role model for me and the brightest example in my first teaching steps.

Professor Charicleia Petridou, I cannot thank you enough. Your vast experience

and knowledge have guided me wisely throughout these years. Thank you Chara for giving me the chance to be part of such a wonderful team; for pulling me back when I was off track. Thank you for all the opportunities you gave me, for all the knowledge, for this wonderful journey. And above all, thank you for your patience and for being...you!

I've had the most wonderful parents and sister one could wish for. Thank you Dimitri, Thaleia, Vicky for your unconditional love and support.

However, words fail me as I try to describe the magnitude of my gratitude towards my other half, my soul-mate, my wife, Katerina. You are my rock. This is for you.

Et ca, c'est fini.